SELF-ASSEMBLED THIN POLYMER FILM USED FOR SENSING APPLICATION

by

FENG LI

B.S., Nankai University, 2000
M.S., China Agriculture University, 2004

AN ABSTRACT OF A DISSERTATION

submitted in partial fulfillment of the requirements for the degree

DOCTOR OF PHILOSOPHY

Department of Chemistry
College of Arts and Sciences

KANSAS STATE UNIVERSITY
Manhattan, Kansas

2013

Abstract

Polymer thin films have played an important role in our everyday lives ranging from industrial to biomedical applications. In this thesis, two major topics based on polymer thin films including photopolymerized self-assembled monolayer and nanoporous thin films derived from diblock copolymer are discussed.

In the first part of this thesis, a well-packed self-assembled monolayer with phosphonic acid as head group and diacetylenic functional group in the tail formed on AlGaN/GaN surface. According to water contact angle and UV/Vis absorption spectroscopy data, the stability of this self assembled monolayer on oxidized AlGaN/ GaN surface can be improved by photopolymerization of SAMs. The photopolymerization efficiency of the SAMs is effected by the position of polymerization functional group in the alkyl chain.

In the second part of this thesis, PS-b-PMMA diblock copolymer thin films were prepared, characterized and applied as a template for electron transfer efficiency determination. The surface COOH group in nanoporous thin films derived from PS-b-PMMA were modified with ferrocene redox moieties having different linker lengths in the organic phase. The surface functionalization efficiency was quantitatively assessed by measuring the monovalent probe cations released from the surface COOH groups via cation-exchange processes using highly-sensitive analytical techniques including spectrofluorometry and inductively coupled plasma mass spectrometry (ICP-MS). The surface coverage of the redox moieties is an important parameter to determine the electron hopping efficiency. The electron propagation resulted from electron hopping across relatively large spacing that was controlled by the motion of anchored redox sites. The longer linker led to the larger physical displacement range of anchored ferrocene moieties, facilitating the approach of the adjacent ferrocene moieties within a distance required for electron self-exchange reaction. Faradic currents originating from redox-involved electron hopping through the ferrocene moieties anchored onto the insulator surface decreased with increasing the concentration of beta-cyclodextrin (β-CD) in aqueous solution. The current could be recovered by adding redox-inactive guest molecules of β-CD to the solution.

SELF-ASSEMBLED THIN POLYMER FILM USED FOR SENSING APPLICATION

by

FENG LI

B.S., Nankai University, 2000
M.S., China Agriculture University, 2004

A DISSERTATION

submitted in partial fulfillment of the requirements for the degree

DOCTOR OF PHILOSOPHY

Department of Chemistry
College of Arts and Sciences

KANSAS STATE UNIVERSITY
Manhattan, Kansas

2013

Approved by:

Major Professor
Takashi Ito

Copyright

Abstract

Polymer thin films have played an important role in our everyday lives ranging from industrial to biomedical applications. In this thesis, two major topics based on polymer thin films including photopolymerized self-assembled monolayer and nanoporous thin films derived from diblock copolymer are discussed.

In the first part of this thesis, a well-packed self-assembled monolayer with phosphonic acid as head group and diacetylenic functional group in the tail formed on AlGaN/GaN surface. According to water contact angle and UV/Vis absorption spectroscopy data, the stability of this self assembled monolayer on oxidized AlGaN/ GaN surface can be improved by photopolymerization of SAMs. The photopolymerization efficiency of the SAMs is effected by the position of polymerization functional group in the alkyl chain.

In the second part of this thesis, PS-b-PMMA diblock copolymer thin films were prepared, characterized and applied as a template for electron transfer efficiency determination. The surface COOH group in nanoporous thin films derived from PS-b-PMMA were modified with ferrocene redox moieties having different linker lengths in the organic phase. The surface functionalization efficiency was quantitatively assessed by measuring the monovalent probe cations released from the surface COOH groups via cation-exchange processes using highly-sensitive analytical techniques including spectrofluorometry and inductively coupled plasma mass spectrometry (ICP-MS). The surface coverage of the redox moieties is an important parameter to determine the electron hopping efficiency. The electron propagation resulted from electron hopping across relatively large spacing that was controlled by the motion of anchored redox sites. The longer linker led to the larger physical displacement range of anchored ferrocene moieties, facilitating the approach of the adjacent ferrocene moieties within a distance required for electron self-exchange reaction. Faradic currents originating from redox-involved electron hopping through the ferrocene moieties anchored onto the insulator surface decreased with increasing the concentration of beta-cyclodextrin (β-CD) in aqueous solution. The current could be recovered by adding redox-inactive guest molecules of β-CD to the solution.

Table of Contents

List of Figures

List of Tables

Acknowledgements

Here I am glad to have this opportunity to say thanks to my friends and colleagues for their assistance. The work presented in this thesis would not have been possible without their help.

First and foremost, I would like to express my sincerest appreciation to my advisor Dr. Takashi Ito. Beyond providing financial support and laboratory space, Dr. Ito has been a constant source of ideas and motivation. He has required me to consider every research problem, and his incredible laboratory intuition has kept me on a productive path from beginning to end. His efforts have made me a much better chemist than I was six years ago.

I am very grateful to the members of my advisory committees for guidance in the course of my graduate studies and doctoral research: Professor Christer Aakeräy, Professor James Edgar, Professor Jun Li for their suggestions on my PhD proposal and their valuable time and I also thank the chairperson and Professor Anil Pahwa for conducting the exam.

My heartfelt gratitude goes to all of the group members of the Ito group, both past and present, for their suggestions and advice during group meetings and in discussion, their help in the lab. To Bipin Pandey, Khanh Hoa Tran Ba, Dr. Yongxin Li, Dr. Shaida Ibrahim and Dr. Neluni Perrera: Thanks these wonderful people for making our lab an enjoyable and interesting place to work. Special thanks go to those undergraduate students Evgeniy Shishkin, Ruben Diaz who were involved in my PhD works. I also would like acknowledge my committee member Dr. Edgar and Michael A. Mastro, Jennifer K. Hite and Charles R. Eddy, Jr from Naval Research Laboratory for providing the AlGaN substrates.

To the Chemistry department faculty and staff - I would like to thank Tobe Eggers, Ron Jackson, Earline Dikeman, Jim Hodgson, Mary Dooley and Kim Ross for helping me in various ways.

I have been lucky to have very good friends around me all the time in Kansas State Uuniversity, and also those old friends in China. I would like acknowledge my friends for lending me an ear when needed, and offering their opinions and advice during the past six years.

I am deeply grateful to my parents and other family members who were always close by me during my graduate school years. They supported me in everything I did. During times when

things in life were not going so well, they were the ones who gave me the needed encouragement that helped me move on. I am very fortunate for that and I owe it all to them.

My graduate school experience was filled with moments of joy, pride, frustration, and disappointment, but most of all, it was simply delightful and rewarding. Now I'm eagerly looking forward to my next experience.

Dedication

To My Daughter

Chapter 1 - Introduction

1.1 Research Motivation

A thin film is a layer of material ranging from fractions of a nanometer to several micrometers in thickness. Thin films have very interesting properties that are quite different from the bulk materials that they are made of. This is because of the fact that their properties depend on a number of interrelated parameters, and also on the technique employed for their fabrication. Currently, thin films are mainly applied to electronic semiconductor devices and optical coatings.

The process of introducing a thin film to a surface is thin film deposition: the techniques for depositing a thin film of material onto a substrate or onto previously deposited layers. There are basically two kinds of deposition techniques, depending on whether the process is primarily chemical or physical. Self-assembly is one of the mostly applied chemical deposition technique for preparing thin layers. There are lots of examples for self-assembly in literature: self-assembled monolayers (SAMs) on solid substrate, [1-9] block copolymers morphologies formed in solution and when confined to surfaces, [10-12] the field of supramolecular chemistry, [13] and the inorganic synthesis of nanorods, nanotubes.[14] Self-assembly is observed even in nature when phospholipid bilayers self-assemble to encapsulate cells.[15] Use of self-assembly techniques can be used to mimic nature's building blocks and create an investigative platform to study model lipid bilayers and model biological cells through microfluidically formed microgels.[16-18]

Self-assembly is a dynamic process. In this process, a disordered pre-existing components system forms an organized structure or pattern without external direction. Self-assembly can be defined as the spontaneous and reversible organization of molecular units into ordered structures by non-covalent interactions.[1] In this research, two self-assembled polymer thin films are studied: photopolymerized self-assembled monolayers and diblock copolymer thin films.

Polymer thin films are an important part of our everyday lives and are found anywhere in industrial and biomedical applications such as paints, coatings, packaging, adhesives, dielectrics, and other common entities because of their versatility, integrity, and dependability. At the same time, the polymer thin film field has been continuously expanded into new technologies and

applications. These new applications have shortcomings and subtleness in the polymer thin film properties and behavior.

This dessertatoin begins with a description of the photopolymerized self-assembled monolayer on semiconductor surface. The thermodynamic stability of a self-assembled monolayer on a surface is not always guaranteed, so our goal was to keep the geometry stable under a variety of processing and performance conditions. A delicate, methodical way to prepare stabled monolayer film was adopted. The first half of this research engages in a comprehensive study of the stability of a self-assembled monolayer on semiconductor surface and developing a model for polymerized monolayer film.

Second, block copolymer thin films can phase-separate and elegantly self-assemble into a variety of highly ordered nanostructures. In this research, we are going to use the cylindrical domain structure derived from diblock copolymer thin films. By controlling over nanodomain orientation in thin films of PS-*b*-PMMA, we can get vertical domain orientation of the nanoscale PMMA cylinders. By selectively removing PMMA domain, a dense cylindrical nanopore array with uniform pore size is obtained. In addition, the surface of the nanopores was subsequently modified via esterification or amidation of surface COOH group with chemical recognition functional groups so these thin films can be used for sensing and energy applications.

1.2 Self-Assembled Monolayers and Applications

1.2.1 Self-Assembled Monolayers (SAMs)

Self-assembled monolayers (SAMs) are ordered thin films of molecular assemblies on solid substrates. These thin films are formed spontaneously by the immersion of an appropriate substrate into a solution with an active surfactant, such as alkanethiols, sulfides, and disulfides in an organic or aqueous solvent.[3] In 1983, Nuzzo and Allara reported the first paper on the self-assembly of diakyldisulfides on gold surfaces resulting in well packed monolayers. [19] After that, SAMs attracted lots of attention in the field of surface chemistry, especially for sensing applications.[20] This is because SAMs, in which molecules are chemically adsorbed on the surface of the substrate, are stable and by incorporating molecules with various functional groups worked as chemical recognition sites can be achieved. In Langmuir-Brodgett films previously used, the molecules are absorbed physically on the substrate and the molecules are so unstable that they may be easily removed from the solid substrate in short time. Comparing with LB

films, the SAMs chemically attached on substrates with relatively high stability and also molecules are not required to be amphiphilic. From this point of view, the application of this chemical sensor system using SAMs is thought to be a quite promising and widely applicable method.

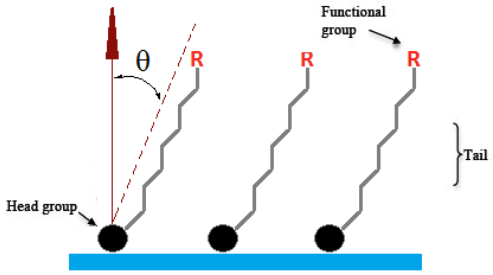

Figure 1.1 Representation of a SAM Structure

A typical self-assembled monolayer consisting of a head group, tail and functional end group on the substrates is depicted in Figure 1.1. Here, the functional groups give the substrate bearing the surface with specific functions. For sensing application, this functional group is the most important part related to chemical recognition of the sensors. However, the performance of the sensors will also depend on the packing of the monolayers.

The head group and the tail will affect the final packing of the monolayers on the substrates. Common head groups include thiols, silanes, phosphonates, etc. The head group provides chemisorption on the substrate surface. Here we briefly summarized two cases: SAMs on metal surfaces and SAMs on oxide surfaces. The most extensively investigated types of SAMs are alkanethiols on metal surfaces such as gold, silver, copper, palladium. Since it is easy to deposit as planar thin films and to pattern with conventional lithographic tools or chemical etchants, Au is commonly used for alkanethiols SAMs. Furthermore, Au is reasonably inert to oxidation and readily binds organothiols.[135] In the case of a gold surface immersed in a solution of an alkyl thiol, it is generally assumed that a hydrogen atom is abstracted from a thiol molecule and the resulting radical species undergoes precipitation on the surface, forming a covalent Au–S bond. The chemical equation for the deposition of the alkene thiol on the gold surface can be presented as:[25]

$$R\text{—}SH + Au_n(0) \longrightarrow R\text{—}S\text{—}Au_n(0) + 1/2\,H_2 \qquad \text{Eq 1.1}$$

Previous studies have reported that the monolayer formation on the surface follows a two-step process.[26] According to the Eq 1.1, the process of the chemisorption is first started through the head group, here for example –SH. Because of the more exothermic interaction

between the head group and the surface comparing to the interchain van der Waals interaction, the molecules occupied available binding site on the surface to form low density crystalline islands with the surface aligned molecular axes. Then the surface undergoes a phase transition to a denser phase by realignment of the molecular axes perpendicular to the surface. The density or the packing of the molecules on the surface is related to the interaction of the tail in the molecules including van der Waals interactions (in case of typical alkyl or derivatized alkyl group) or in rare cases hydrogen bonds (in case of carboxylic or hydroxyl group) or electrostatic interactions. After the molecules are put in place to the surface, the formation of an ordered and closely packed assembly started. It's known that the intermolecular interaction is larger in self-assembled monolayers when the molecules on the surface have longer tails, which probably result in a monolayer with better packing and higher stability.

To form a SAM on an oxide surface, the typical material is organosilanes (RSiX3, with X=Cl, OMe, OEt). Hydroxylated substrate surfaces such as SiO_2, Al_2O_3, and ITO are required to form organosilane self assembled monolayers on surfaces. In the case of SiO_2 surfaces, the driving force for self-assembly is the in situ formation of siloxanes, which connect the precursor silane to the surface silanol (–Si–OH) groups via very strong Si–O–Si bonds.[132] Since the substrate surfaces are amorphous, the packing and ordering of the chemisorbed organosilanes are determined by the underlying siloxane network.

Other classes of materials instead of organosilanes deposited on oxide surfaces include n-alkanoic acids and phosphonic acids. These kind molecules have attracted lots of attention due to their ability to bind to a wide range of metal oxide surfaces and to form robust SAMs of similar quality to that of thiols on Au. In this thesis, we are using alkylphosphonic acid to form well packed monolayers on oxidized AlGaN/GaN surface which will give a large impact to the performance of AlGaN/GaN based HEMTs. Same as SAMs on Au, the packing of phosphonate SAMs is also affected by the alkyl chain length. There is a large packing difference between short and long alkyl phosphate SAMs. For the long alkyl phosphate SAMs, the enthalpy gain due to van der Waal interactions between the tightly packed alkyl chains stabilizes the SAMs on the surface.

In this research, a side application using self-assembled monolayers has also been used in chapter 5. The electrochemical desorption of the thiol self-assembled monolayers on gold surface was used to determine the open surface area of the working electrode.[21-23] This method was

reported by Porter and coworkers for the first time.[24] By sweeping a potential of -1.5 V vs Ag/AgCl to an alkanethiol SAM on Au electrode, a reduction peak appeared at -0.7 V to -1.4 V vs Ag/AgCl. The peak area is corresponding to the coverage of the self-assembled thiol molecules on the gold surface. By comparing the self- assembled monolayer desorption peak area of sample with known surface area and unknown, we can calculate exposed gold electrode surface coated with nanoporous PS-b-PMMA thin films.

1.2.2 Application of SAMs on High Electron Mobility Transistors (HEMTs)

High electron mobility transistor (HEMT) is a field effect transistor incorporating a junction between two semiconductors with different band gaps as the channel instead of a doped region, as is generally the case for MOSFET. It has been more than 25 years since the high electron mobility transistor (HEMT) was first proposed in 1979.[27] To allow conduction, semiconductors are doped with impurities which donate mobile electrons. However, these electrons are slowed down through collisions with the impurities. HEMTs avoid this through the high mobility electrons generated by the heterojunction of a highly doped wide-band gap n-type donor-supply layer and a non-doped narrow-band gap channel layer. Electrons generated in the highly-doped wide-band gap n-type donor-supply layer drop completely into the non-doped narrow-band gap channel layer to form a depleted layer, because the heterojunction created by different band-gap materials forms a quantum well in the conduction band on the non-doped layer side where the electrons can move quickly without colliding with any impurities, and from which they cannot escape. This creates a high concentration of highly mobile conducting electrons in a thin layer, giving the channel very low resistivity. This layer is called a two-dimensional electron gas. As with all the other types of FETs, a voltage applied to the gate alters the conductivity of this layer.

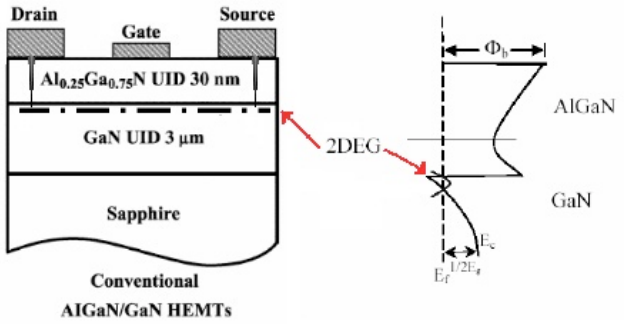

Figure 1.2 The basic structure of HEMTs[140]

The key concept of the HEMT is the field-effect modulation of the high-mobility two-dimensional electron gas (2DEG) at the heterostructure consisting of one of the selectively doped semiconductor pairs. A commonly used semiconductor combination is GaAs/AlGaAs. More recently studies have focused mainly on developing chemical and biological sensors using AlGaN/GaN high electron mobility transistors.[28-30] These devices can be miniaturized to develop portable chemical sensors, similar to silicon-based transistors and will be more robust chemically and physically as compared with Si-based devices.

AlGaN/GaN based transistors are sensitive signal transducers can also be used to develop sensitive chemical sensors,. However, because of their properties like low chemical selectivity and also the low chemical reactivity of the AlGaN based gate surface, the sensors based on AlGaN/GaN transducers are only able to detect a limited number of chemical species. Researchers have improved the chemical selectivity by chemically modifying the gate surface of AlGaN transistors with organic monolayers thin film having chemical recognition moieties. For example, Ren's group used biotin-terminated organosilane self-assembled monolayers modified the AlGaN gate area by forming a covalent bond between silane and oxidized AlGaN surface to detect specific adsorption of streptavidin as a current changes between source and drain in the HEMT.[31] A common method to form self-assembled monolayers is to assemble the thiol terminated molecules on gold surface. Ren's group first coated a lay of gold on AlGaN/GaN HEMTs' gates, then a thiol modified probe DNA was assembled on the gold used for DNA detection.[32]

In previous studies, researchers have demonstrated that reactive groups such as amines and thiols can directly link to the GaN surface under ultrahigh vacuum conditions.[33] However, the density of the monolayers with these functional groups is low. Researchers demonstrated that organophosphonic acids have high affinities to surface oxides of materials, including oxides of ion, aluminum and titanium. In our group's studies,[139] it's shown that the alkylphosphonic acid can form a densely packed monolayer on oxidized GaN surface. Phosphoric acid is attractive for GaN surface modification because of its highly reproducibility. However, the sensors will used under some ambient conditions, so the stabilities of the monolayer is important as it can affect the performance of the sensors. In this research, we are thinking to make the polymerized monolayer thin film on GaN surface to improve the stability of the monolayer.

Studies have shown that certain crystalline diacetylenes have a dramatic color change by storaging under ambient conditions for a century. Until the mid of last century, Schmidt predict that the color change must be the result of a polymerization process in course of which the C1 and C4 carbon atoms of adjacent diacetylene moieties in a molecular stack are linked together.[34] As a polymerization moiety, the photopolymerization of the conjugated diacetylene in thin films such as nanoscale molecular assemblies,[35, 36] Langmuir-Blodgett (LB) films,[3, 36-41] and also SAMs have been widely investigated to improve the physical and chemical stability.[42,43] Here, in this research, we are trying to get a well packed diacetylenic self-assembled monolayers on AlGaN/GaN surface which has unique optical and electric properties, and also stabilize the monolayers by photopolymerization to provide a potential platform for developing unique chemical and biological sensing devices.

1.3 Electron Transfer Studies Based on Self-Assembled Block Copolymer Thin Films

1.3.1 Block copolymer thin films

Nanometer-scale pores have unique characteristics for various chemical sensing applications. The nanoporous membranes containing nanometer-scale pores include track etched membranes (polycarbonate / polyester), anodic aluminum oxide membranes, and block copolymer (BCP) nanoporous films.[44]

When we talk about polymer, it is a high molecular weight macromolecule made up of multiple repeating units called monomer. When the polymer is made up by only one kind of monomer, it is called homopolymer. When there are at least two different types of monomers (for example A and B), the polymer is called a copolymer. Depending on the block organization, different copolymers are found such as statistic copolymer, alternating copolymer, graft copolymer and also block copolymer (Figure 1.3). When there are several homopolymers covalently grafted to each other linearly to form a chain-like polymer, the resulting molecule is called a block copolymer.[44]

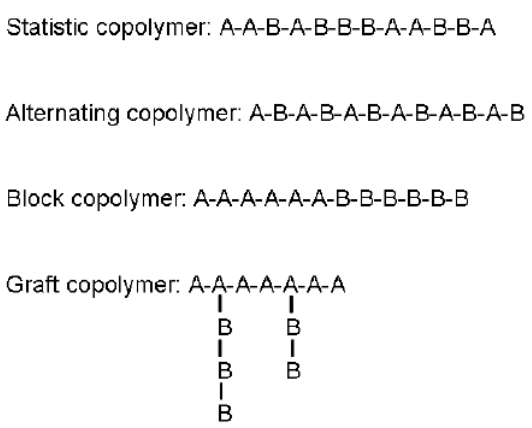

Figure 1.3 Structures for Different Types of Copolymer

Block copolymers are polymers with two or more chemically distinct polymer fragments connected together in a long chain (figure 1.3). Block copolymers can be used for fabricating thin films by phase separation into nanodomains within the bulk segment due to the chemical incompatibility of the monomeric segments. Nakahama's group demonstrated the first nanoporous membrane derived from block copolymer in 1980s.[45] They synthesized a lamellar morphology of poly (4-vinylphenyl-dimethyl-2-propoxysilane)-b-polyisoprene-b-poly (4-vinylphenyl-dimethyl-2-propoxysilane) (PPS-PI-PPS) triblock copolymer film. After degrading the minor component of PI in the triblock copolymer via ozonolysis/methanol, they generated a porous structure which they characterized with SEM and TEM.[46-52] The cylindrical domain shapes also attracted lots of attention. If the constituent polymers are immiscible and the volume fraction of the fragments in a block copolymer is appropriate, the minor components form cylindrical domains via self-assembly. Mansky's group prepared a block copolymer membrane derived from block copolymers in orienting the cylindrical domains perpendicular to the underlying substrate which has the potential to be used as lithographic templates.[49] In their work, thin films of polystyrene-polybutadiene (PS-PBD) with vertically oriented PBD domains were prepared and the PBD component degraded via ozonolysis to generate a well-ordered porous template. Since then, nanoporous films obtained from cylinder-forming block copolymer have attracted much attention studying the self assembly of block copolymers in terms of its chemistry and thermodynamics owing to their potential for template applications.[53-56] In view of this, it is not surprising that block copolymers fall into the category of nanomaterials that are well-explored and documented.[57-59] The majority of such work was driven by the potential applications of block copolymer templates as chemical sensors,[60] heterogeneous catalysis,[61]

separation membranes,[62-64] and lithographic templates for the synthesis of nanomaterials of desired size and shapes.[65-67]

Due to chemical and physical incompatibility block copolymer segments are often immiscible and thus phase separate into domains rich in one phase within the bulk rich in the other phase. The resulting morphology depends largely on the relative volume fraction of each component. Compared to diblock copolymer, triblock copolymers, with three chemically distinct polymer fragments, introduce additional building blocks hence more complex morphologies. Generally, in bulk, diblock copolymers with immiscible blocks can microphase separate as a function of composition into a variety of morphologies, including spheres (S), cylinders (C), bicontinuous gyroids (G), lamellae (L), etc., as shown in Figure 1.4.[68] The self-assembly process is driven by an unfavorable mixing enthalpy coupled with a small mixing entropy, with the covalent bond connecting the blocks preventing macroscopic phase separation. The microphase separation of diblock copolymers depends on three parameters:[68] (1) the volume fractions of the A and B blocks , (2) the total degree of polymerization, and (3) the Flory–Huggins parameter, χ_{AB}. The χ-parameter specifies the degree of incompatibility between the A and B blocks, which drives the phase separation.

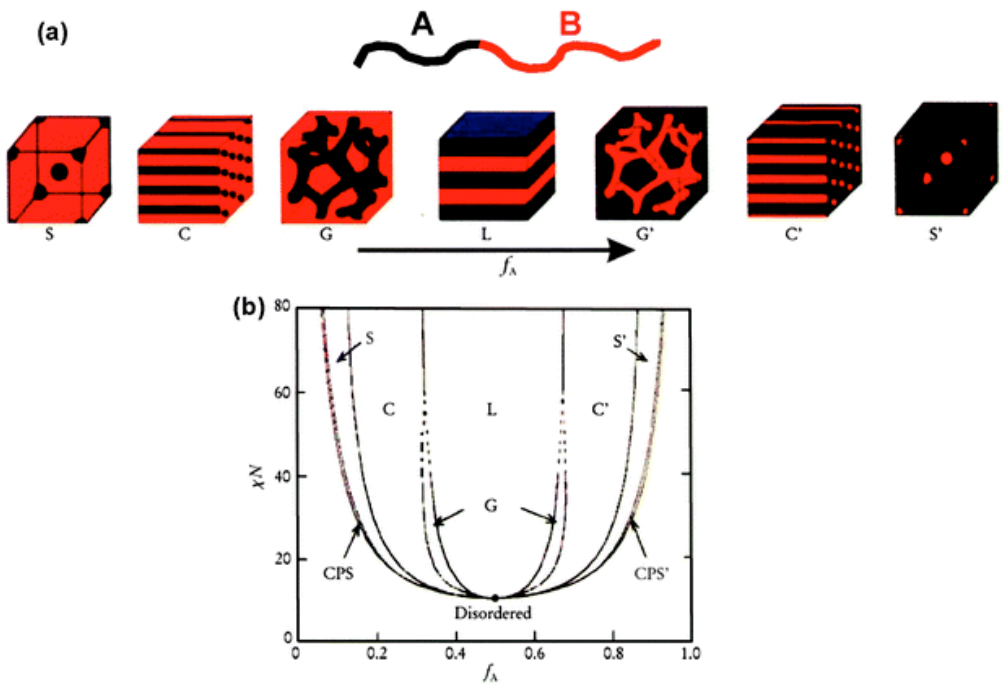

Figure 1.4 (a) Equilibrium morphologies of AB diblock copolymers in bulk (b) Theoretical phase diagram of AB diblocks predicted by the self-consistent mean-field theory, depending on volume fraction (f) of the blocks and the segregation parameter, χN, where χ is the Flory–Huggins segment–segment interaction energy and *N* is the degree of polymerization; CPS and CPS′ = closely packed spheres.[69]

For diblock copolymer, when the volume fraction of the minor segment is 0.3, it can phase separate into cylindrical domains within the major segment in thin films. The uniform domain size of diblock copolymers is basically determined by the total molecular weight of the polymer and can be tuned in the range of 5-100nm by choosing an appropriate molecular weight.[58, 59] The uniform domain size is a signature of block copolymer materials.

Thin films of diblock copolymers can be easily fabricated by spin casting from solutions of the polymer onto different substrates, such as gold or silicon substrates. The thickness of such films can be easily controlled by the spin speed and/or polymer solution concentration. The orientation of the domains in a block copolymer film is another signature of block copolymer materials. The orientation of nanodomains (parallel or perpendicular to an underlying substrate) in thin films is largely governed by the wetting properties of each chemically distinct segment of the diblock copolymer at the polymer/substrate interfaces. Interfaces have the strongest influence

when the thickness of the block copolymer film is comparable to the microdomain spacing. Various methods have been employed to control the orientation of the microdomains in thin films of diblock copolymer so that domains orient themselves perpendicular to an underlying substrate. First factor that effects the orientation of the domains is the film thickness. If the film much thinner than the domain spacing often exhibit very little or no microdomains since all polymeric material is used to wet the interfaces.[69-71] Another way to tune the wetting of the surface by chemical tailoring of substrates, via self-assembled monolayers or random copolymer brush layers, which can control the the affinities of both block copolymer segments at the polymer/ substrate interface.[69, 72-74] Russell's group also controlled the PS-b-PEO domain orientation by control the solvent evaporation conditions or introducing the electric field during the annealing.[75-78]

In this research, we are studying the electron transport through redox moieties covalently bounded on cylindrical nanopores derived from a cylinder forming PS-b-PMMA diblock copolymer. Among block copolymer systems, PS-*b*-PMMA has been widely used to fabricate nanostructure materials because these materials can be fabricated using well-established procedures for selectively etching the PMMA domains. The self-assembly of cylinder forming PS-*b*-PMMA, where the PMMA domains were oriented perpendicular to an underlying substrate, was first demonstrated by Russell'group.[77] Here, the volume fraction of the minor component for PS-b-PMMA we used is ~ 30% v/v. During self-assembling, the minor component will self-assemble as cylindrical domains in a matrix of the PS segment.[58, 59, 69] To obtain PS-b-PMMA nanoporous films, the minor component PMMA is etched out chemically,[79] photo-chemically (UV irradiation) or thermally.[80,81] Here, nanoporous films derived from PS-b-PMMA will be prepared by UV irradiation to degrade the cylindrical PMMA domains formed during annealing and by subsequent dissolution of PMMA fragments into acetic acid.

Before the photo-cleavable PS-b-PEO has been introduced, PS-b-PMMA is the only block copolymer system that can form the nanoporous structure using UV radiation. In this degradation process, the PS segment in the thin film is crosslinked at the same time, which results a mechanically and chemically stable PS matrix. Most other BCPs require heat treatment coupled with hydrolysis with strong acids or bases to generate the nanoporous system. Other cylinder forming block copolymer systems which require heat treatment then hydrolysis with strong acids or bases to get the nanoporous system, such as polystyrene-polylactide (PS-PLA),

polystyrene-polydimethylacrylamide-polylactide (PS-PDMA-PLA) and polystyrene-polyimide-polylactide (PS-PI-PLA) will give a PS matrix that is not cross-linked. This might make the nanoporous structure thermally unstable at elevated temperatures comparing with PS-b-PMMA derived nanoporous thin films.[82]

Another important factor that effects the application of nanoporous thin film derived from block copolymer is interactions (specific, non-specific adsorption and electrostatic interactions) between the analytes and nanoporous surface.[83] Thus control of the surface functionalization are key factors for many applications of block copolymers. Surface chemistry of block copolymer is controllable because of functional groups (–COOH) upon formation of nano-pores via etching. [53, 60, 83-85] The presence of -COOH groups on the pore walls was proved by infrared spectroscopy,[66, 86] and pH-dependent CV measurements of charged and uncharged redox molecules.[86] In addition, the control of the charge and protein adsorptivity of the nanopore surface via 1-ethyl-3-(3-dimethylamino- propyl)carbodiimide-mediated amidation of the surface -COOH groups was also demonstrated.[60, 63] Kim's group have developed a method for single nucleotide polymorphism (SNP) detection using functionalized nanopores derived from a diblock copolymer(PS-b-PMMA-diCOOH).[87] To prepare the nanoporous block copolymer (PS-b-PMMA-diCOOH) thin film, PMMA homopolymer which was used to introduce the cylindrical orientation of the nanodomains was added to block copolymer. By etching away the homopolymer and PMMA segment, the –COOH group was exposed to the cylindrical nanopore surface. After modifying the –COOH group with dye labeled overhanging ssDNA probe, this system was used for SNP detection.

1.3.2 Electron Transfer

Electron transfer is a mechanistic description of the thermodynamic concept of redox, wherein the oxidation states of both reaction partners change. Electron transfer (ET) is the process by which an electron moves from one atom or chemical species such as a molecue to another atom or chemical species. It is the simplest and also most important chemical processes in nature. The process of efficiently and controllably moving electrons around is one of the primary regulation mechanisms in biology. Without control of electrons in living organisms, life could simply not exist. For example, electron transfer processes drive photosynthesis and nitrogen fixation. A deep understanding of electron transfer processes is necessary for future

development in many fields of technology and science, ranging from gaining detailed understanding of some biological phenomenon to developing useful molecular electronics for energy and sensing application.

Many systems especially the SAMs of biological molecules have been applied to understand the fundamental principles of electron transfer that control and define the simple act of adding and/or removing electrons from chemical species. Electron transfer rate in these systems can be obtained by application of various physicochemical methods such as electrochemical methods including chronoamperometry, cyclic voltammetry (CV),[88-94] alternating current voltammetry (ACV),[90, 95, 96] electrochemical impedance spectroscopy (EIS),[97, 98] and also photo-physical approaches.[99, 100]

Among the electron transfer process, there are two mechanisms including superexchange and electron-hopping mechanism. Let's use a peptide as an example where the peptide has an electron donor in one side and electron acceptor in another side and the chain works as a bridge of the electron transfer. The mechanisms of this electron transfer include electron-tunneling and electron-hopping mechanisms. In the tunneling mechanism, the bridge serves as a medium to pass the electron between the donor and acceptor, which is different from the hopping mechanism that the electron will jump through the bridge. In a superexchange mechanism, the electron transfer rate depends exponentially on distance, whereas a linear distance relationship is expected for a hopping mechanism.

The first generally accepted theory of electron transfer was developed by Rudolph A. Marcus in 1956 to explain the rates of electron transfer reactions – the rate at which an electron can move or jump from one chemical species to another.[101] The Marcus theory of electron transfer was then extended to include electron-tunneling by Noel Hush and Marcus.[102,103] Since then, the Marcus-Hush theory has guided most discussions of electron transfer. Both theories are, however, semiclassical in nature, although they have been extended to fully quantum mechanical treatments by Joshua Jortner, Alexender M. Kuznetsov, and others proceeding from the Fermi's Golden Rule and following earlier work in non-radiative transitions. Furthermore, theories have been put forward to take into account the effects of vibronic coupling on electron transfer.[104] Before 1991, ET in metalloproteins was thought to affect primarily the diffuse, averaged properties of the non-metal atoms forming an insulated barrier between the metals, but Beratan, Betts and Onuchic[105] subsequently showed that the ET rates are governed by the bond structures

of the proteins -- that the electrons, in effect, tunnel through the bonds comprising the chain structure of the proteins.

1.3.3 Redox-Involved Surface Lateral Electron Transfer

Except for the electron transfer between an electron donor and electron acceptor that are linked by a bridge linker, there is another type of electron transfer reactions happened between participating redox centers that are not linked via any bridge during the electron transfer event. This topic is mainly studied in a 2D structure assembled with redox-active moieties involved systems including self-assembled monolayers,[106-109] Langmuir monolayers,[110-113] and bilayers.[114] This electron transfer behavior across these systems is named surface lateral electron transfer. Researchers have studied how electrons move across these systems, to inprove technological applications such as solar energy conversion,[106,107] sensors,[115] and molecular electronics.[116–119]

People already studied the lateral electron transfer both experimentally and theoretically.[106,107,120,121] First study is using anodic aluminum oxide coated electrodes. Redox moieties were self assembled on the pore surface of a porous aluminum oxide film at a gold electrode and form a bilayer.[122] The Langmuir Blodgett monolayer with redox molecules at air/soln interface has also been used to study the lateral electron transfer.[123] In these kinds of systems, the redox moities are not covalently bonded on the interface. According to Dahms–Ruff equation (Eq 1.2), two modes of motion are primarily responsible for the diffusion of electrons in these systems: physical motion of redox centers (D_{phys}), and hopping of electrons between reduced sites (D_{eh}). These take place simultaneously and independently.[124-126]

$$D = D_{phys} + D_{eh} \qquad \text{Eq 1.2}$$

$$D_{phys} = k_B T / 6\pi\eta C r \qquad \text{Eq 1.3}$$

$$D_{eh} = \delta^2/6\tau \qquad \text{Eq 1.4}$$

Here, k_B is the Boltzmann constant, r the hydrodynamic radius of the redox centers and η is the concentration-dependent viscosity, δ is the displacement distance and τ is the average time between two displacement events.

More recently, redox-involved electron hopping was quantitatively investigated on redox moieties linked to surface of insulator based nanoparticles[127-129] and dendrimers[130, 131]. In these systems, the redox moieties were covalently anchored to the insulator base, which indicate there is no physical motion involved in the electron transport process. According to Saveant's

theoretical study, they assume that electron transfer through the anchored redox moieties originated from electron hopping based on bounded diffusion. In this case, the physical diffusion of the redox moieties is negligable.[120] The apparent diffusivity due to bounded diffusion can be described in the Eq 1.5.

$$D_{eh} = \frac{1}{2\nu t_e}\left[\nu\lambda^2\left(\frac{\rho}{1+\rho}\right)+\delta^2\right] \qquad \text{Eq 1.5}$$

In this equation, λ is the mean physical displacement of a redox center that is chemically bonded. δ is the electron hopping distance, and ρ is the ratio of the mean-squared displacement for free diffusion after a time the average time between electrons hops to the maximum mean-squared displacement. When the physical motion of the redox moieties is much faster than electron hopping, the equation can be rewrite as:

$$D_{eh} = \frac{\left(\nu\lambda^2+\delta^2\right)}{2\nu t_e} \qquad \text{Eq 1.6}$$

Using Saveant's theory, Hotton's group[134] studied the bounded diffusion in redox polymer. Here, according to Bu and coworker's observation [133], the mean physical displacement of a redox center λ related to the concentration of the redox center in the polymer, they approximate the bounded diffusion contribution to the apparent diffusivity by:

$$D_{ap} = \frac{K_{act}}{6}\left[3\lambda^2\left(\frac{\rho}{1+\rho}\right)+\delta^2\right] \qquad \text{Eq 1.7}$$

$$\lambda^2\left(\frac{\rho}{1+\rho}\right) \approx \left(\frac{\omega}{c^n}\right)^2 \qquad \text{Eq 1.8}$$

Here, ω and n are positive parameters specific to a given redox polymer system. Thus, the modified Blauch-Saveant equation is:

$$D_{ap} = \frac{K_{act}}{6}\left(3\frac{\omega^2}{c^{2n}}+\delta^2\right) \qquad \text{Eq 1.9}$$

This bounded diffusion should be affected by the physical displacement of redox moieties. Two factors will define this physical displacement range: one is the center to center distance between redox moieties, and the other one is the distance between bounded sites to redox center which reflect the flexibility of the redox centers.

In this thesis, diblock copolymer nanoporous thin film will be used as a media to experimentally study the electron hopping process through the redox moieties anchored on the nanopore surface and try to use it for sensing application.

References

1. Dubois, L.; Nuzzo, R. *Annu. Rev. Phys. Chem.,* **1992**, 43, 437-463.
2. Ogawa, H.; Takamura, T.; Shimoyama, Y. *Jpn. J. Appl. Phys.,* **1999**, 38, 6019-6023.
3. Ullman, A. An Introduction to Ultrathin Organic Films: From Langmuir--Blodgett to Self--Assembly Academic Press, 1991.
4. Sullivan, T.; Huck, W. *Eur J. Org. Chem.,* **2003**, 17-29.
5. Bain, C.; Evall, J.; Whitesides, G. *J. Am. Chem. Soc.,* **1989**, 111, 7155-7164.
6. Bain, C.; Troughton, E.; Tao, Y.; Evall, J.; Whitesides, G.; Nuzzo, R. *J. Am. Chem. Soc.,* **1989**, 111, 321-335.
7. Bain, C.; Whitesides, G. *J. Am. Chem. Soc.,* **1989**, 111, 7164-7175.
8. Chidsey, C.; Bertozzi, C.; Putvinski, T.; Mujsce, A. *J. Am. Chem. Soc.,* **1990**, 112, 4301-4306.
9. Porter, M.; Bright, T.; Allara, D.; Chidsey, C. *J. Am. Chem. Soc.,* **1987**, 109, 3559-3568.
10. Bates, F.; Fredrickson, G. *Annu. Rev. Phys. Chem.,* **1990**, 41, 525-557.
11. Park, C.; Yoon, J.; Thomas, E. *Polymer,* **2003**, 44, 6725-6760.
12. Krausch, G.; Magerle, R. *Adv. Mater.,* **2002**, 14, 1579-1583.
13. Lehn, J. M. *Science,* **1993,** 260, 1762-1763.
14. Ozin, G. A. Nanochemistry: A Chemical Approach to Nanomaterials; Royal Society of Chemistry, **2005**.
15. Cevc, G.; Marsh, D. Phospholipid Bilayers: Physical Principles and Models; John Wiley and Sons: New York, **1987**.
16. Tien, H. T. *Adv. Mater.,* **1990**, 2, 316-318.
17. Brizard, A. M.; Van Esch, J. H. *Soft Matter.,* **2009**, 5, 1320-1327.
18. Tumarkin, E.; Kumacheva, E. *Chem. Soc. Rev.,* **2009**, 38, 2161-2168.
19. Nuzzo, R. G.; Allara, D. L. *J. Am. Chem. Soc*., **1983,** 105, 4481-4483.
20. Buhlmann, P.; Aoki, H.; Xiao, K. P.; Amemiya, S.; Tohda, K.; and Umezawa,Y. *Electroanalysis*, **1998**, 10, 1149-1158.
21. Widrig, C. A.; Chung, C.; Porter, M. D. *J. Electroanal. Chem.,* **1991**, 310, 335–359.
22. Ito, T.. *J. Electroanal. Chem.,* **2001**, 495, 87–97.
23. Li, F., Pandey, B., and Ito, T. *Langmuir*, **2012**, 28, 16496-16500

24. Weisshaar, D. E.; Lamp, B. D.; Porter, M. D. *J. Am. Chem. Soc.,* **1992**, 114,
25. 5860-5862.
26. Ulman, A. *Chem. Rev.*, **1996**, 96, 1533-1554.
27. Pirier, G. E.; and Pylant, E. D. *Science*, **1996**, 272, 1145.
28. Mimura, T.; Hiyamizu, S.; Fuji, T.; and Nanbu, K. *Jpn. J. Appl. Phys.* **1980**, 19, L225.
29. Pearton, S. J.; Kang, B. S.; Kim, S.; Ren, F.; Gila, B. P.; Abernathy, C. R.; Lin, J.; and Chu, S. N. G. *J. Phys.: Condens. Matter.*, **2004**, 16, R961-R994.
30. Kang, B. S.; Wang, H.-T.; Tien, L.-C.; Ren, F.; Gila, B. P.; Norton, D. P.; Abernathy, C. R.; Lin, J.; and Pearton, S. *J. Sensors*, **2006**, 6, 643-666.
31. Steinhoff, G.; Purrucker, O.; Tanaka, M.; Stutzmann, M.; and Eickhoff, M. *Adv. Funct. Mater.*, **2003,** 13, 841-846.
32. Kang, B. S.; Ren, F.; Wang, L.; Lofton, C.; Tan, W. W.; Pearton, S. J.; Dabiran, A.; Osinsky, A.; and Chow, P. P. *Appl. Phys. Lett.*, **2005**, 87, 023508.
33. Kang, B. S.; Pearton, S. J.; Chen, J. J.; Ren, F.; Johnson, J. W.; Therrien, R. J.; Rajagopal, P.; Roberts, J. C.; Piner, E. L.; Linthicum, K. J. *Appl. Phys. Lett.*, **2006,** 89, 122102.
34. Bermudez, V. M. *Chem. Phys. Lett.*, **2000**, 317, 290-295.
35. Schmidt, G. M. J.: "Photochemistry of the Solid State", in "Reactivity of the Photoexcited Organic Molecule", Wiley, N.Y. **1967**.
36. Mueller, A.; O'Brien, D. F. *Chem. Rev*. **2002,** 102, 727-757.
37. Reppy, M. A.; Pindzola, B. A. *Chem. Commun.* **2007**, 42, 4317-4338.
38. Tieke, B.; Lieser, G. *J. Colloid Interface Sci.,* **1982,** 88, 471-486.
39. Ostermayer, B.; Vogt, W. Makromol. *Chem., Rapid Commun.,* **1982**, 3, 563-568.
40. Albrecht, O.; Laschewsky, A.; Ringsdorf, H. *J. Memb. Sci.*, **1985**, 22, 187-197.
41. Ostermayer, B.; Albrecht, O.; Vogt, W. *Chem. Phys. Lipids,* **1986**, 41, 265-291.
42. Carpick, R. W.; Sasaki, D. Y.; Marcus, M. S.; Eriksson, M. A.; Burns, A. R. *J. Phys.: Condens. Matter*, **2004**, 16, R679-R697.
43. Batchelder, D. N.; Evans, S. D.; Freeman, T. L.; Haussling, L.; Ringsdorf, H.; Wolf, H. *J. Am. Chem. Soc.*, **1994**, 116, 1050-1053.
44. Kim, T.; Chan, K. C.; Crooks, R. M. *J. Am. Chem. Soc.* **1997**, 119, 189-193.

45. Ito, T.; Perera, D. M. N. T. In Analytical Applications of Block Copolymer Derived Nanoporous Membranes; Pierce, D. T., Zhao, J. X., Eds.; Trace Analysis with Nanomaterials; WILEY-VCH Verlag GmbH & Co. KGaA: Weinheim**, 2010**.
46. Lee, J.; Hirao, A.; Nakahama, S. *Macromolecules,* **1988**, 21, 274-276.
47. Lee, J.; Hirao, A.; Nakahama, S. *Macromolecules*, **1989**, 22, 2602-2606.
48. Hedrick, J. L.; Labadie, J.; Russell, T.; Hofer, D.; Wakharker, V. *Polymer,* **1993**, 34, 4717-4726.
49. Mansky, P.; Chaikin, P. M.; Thomas, E. L. *J. Mater. Sci.,* **1995**, 30, 1987-1992.
50. Mansky, P.; Harrison, C. K.; Chaikin, P. M.; Register, R. A.; Yao, N. *Appl. Phys. Lett.*, **1996**, 68, 2586-2588.
51. Liu, G.; Ding, J.; Guo, A.; Herfort, M.; Bazett-Jones, D. *Macromolecules*, **1997**, 30, 1851-1853.
52. Hashimoto, T.; Tsutsumi, K.; Funaki, Y. *Langmuir*, **1997**, 13, 6869-6872.
53. Hedrick, J. L.; Labadie, J. W.; Volksen, W.; Hilborn, J. G. *Adv. Polym. Sci.,* **1999**, 147, 61-111.
54. Park, M.; Harrison, C.; Chaikin, P. M.; Register, R. A.; Adamson, D. H. *Science*, **1997**, 276, 1401-1404.
55. Harrison, C.; Park, M.; Chaikin, P. M.; Register, R. A.; Adamson, D. H. *J. Vac. Sci. Technol. B*, **1998**, 16, 544-552.
56. Thurn-Albrecht, T.; Steiner, R.; DeRouchey, J.; Stafford, C. M.; Huang, E.; Bal, M.; Tuominen, M.; Hawker, C. J.; Russell, T. P. *Adv. Mater.,* **2000**, 12, 787-791.
57. Park, M.; Chaikin, P. M.; Register, R. A.; Adamson, D. H. *Appl. Phys. Lett.,* **2001**, 79, 257-259.
58. Fasolka, M. J.; Mayes, A. M. *Annu. Rev. Mater. Res.,* **2001**, 31, 323-355.
59. Hillmyer, M. A. *Adv. Polym. Sci.,* **2005**, 190, 137-181.
60. Olson, D. A.; Chen, L.; Hillmyer, M. A. *Chem. Mater.,* **2008**, 20, 869-890.
61. Li, Y.; Ito, T. *Langmuir*, **2008**, 24, 8959-8963.
62. Mercier, L.; Pinnavaia, T. *J. Adv. Mater*., **1997**, 9, 500-503.
63. Yang, S. Y.; Ryu, I.; Kim, H. Y.; Kim, J. K.; Jang, S. K.; Russell, T. P. *Adv. Mater.,* **2006**, 18, 709-712.
64. Li, Y.; Ito, T. *Anal. Chem.*, **2009**, 81, 851-855.

65. Nuxoll, E. E.; Hillmyer, M. A.; Wang, R.; Leighton, C.; Siegel, R. A. *ACS Appl. Mater. Interfaces,* **2009**, 1, 888-893.
66. Zhang, Q.; Xu, T.; Butterfield, D.; Misner, M. J.; Ryu, D. Y.; Emrick, T.; Russell, T. P. *Nano. Lett.,* **2005**, 5, 357-361.
67. Darling, S. B.; Yufa, N. A.; Cisse, A. L.; Bader, S. D.; Sibener, S. *J. Adv. Mater*., **2005**, 17, 2446-2450.
68. Darling, S. B. *Surf. Sci.*, **2007**, 601, 2555-2561.
69. Bates, F. S.; Fredrichson, G. H. *Phys. Today*, **1999**, 52, 32–38
70. Li, M.; Coenjarts, C. A.; Ober, C. K. *Adv. Polym. Sci.,* **2005**, 190, 183−226.
71. Fasolka, M. J.; Mayes, A. M. *Annu. Rev. Mater. Res.,* **2001**, 31, 323−355.
72. Wang, H.; Djurisic, A. B.; Xie, M. H.; Chan, W. K.; Kutsay, O. *Thin Solid Films,* **2005**, 488, 329−336.
73. Mansky, P.; Liu, Y.; Huang, E.; Russell, T. P.; Hawker, C. *Science*, **1997**, 275, 1458−1460.
74. Mansky, P.; Russell, T. P.; Hawker, C. J.; Pitsikalis, M.; Mays, J. *Macromolecules*, **1997**, 30, 6810−6813.
75. Heier, J.; Kramer, E. J.; Walheim, S.; Krausch, G. *Macromolecules*, **1997**, 30, 6610−6614.
76. Kim, S.; Misner, M.; Kimura, M., Xu, T.; Russell, T. P. *Advanced Materials*, **2004**, 16, 226-231.
77. Thurn-Albrecht, T.; DeRouchey, J.; Russell, T. P.; Jaeger, H. M. *Macromolecules*, **2000**, 33, 3250−3253.
78. Thurn-Albrecht, T.; Steiner, R.; DeRouchey, J.; Stafford, C. M.; Huang, E.; Bal, M.; Tuominen, M.; Hawker, C. J.; Russell, T. P. *Adv. Mater.,* **2000**, 12, 787−791.
79. Thurn-Albrecht, T.; Schotter, J.; Kastle, G. A.; Emley, N.; Shibauchi, T.; Krusin-Elbaum, L.; Guarini, K.; Black, C. T.; Tuominen, M. T.; Russell, T. P. *Science*, **2000**, 290, 2126−2129.
80. Zalusky, A. S.; Olayo-Valles, R.; Wolf, J. H.; Hillmyer, M. A. *J. Am. Chem. Soc.,* **2002**, 124, 12761-12773.
81. Melde, B. J.; Burkett, S. L.; Xu, T.; Goldbach, J. T.; Russell, T. P.; Hawker, C. J. *Chemistry of Materials,* **2005**, 17, 4743-4749.

82. Chung, C. M.; Lee, J. H.; Cho, S. Y.; Kim, J. G.; Moon, S. Y. *J Appl. Polym. Sci.,* **2006**, 101, 532-538.
83. Jeong, U.; Ryu, D. Y.; Kim, J. K.; Kim, D. H.; Wu, X.; Russell, T. P. *Macromolecules*, **2003**, 36, 10126-10129.
84. Rzayev, J.; Hillmyer, M. A. *J. Am. Chem. Soc.*, **2005**, 127, 13373-13379.
85. Bailey, T. S.; Rzayev, J.; Hillmyer, M. A. *Macromolecules*, **2006**, 39, 8772-8781.
86. Klaikherd, A.; Ghosh, S.; Thayumanavan, S. *Macromolecules*, **2007**, 40, 8518-8520.
87. Li, Y.; Maire, H. C.; Ito, T. *Langmuir*, **2007**, 23, 12771-12776.
88. Yang, S. Y.; Son, S.; Jang, S.; Kim, H.; Jeon, G.; Kim, W. J.; Kim, J. K. *Nano. Lett.,*
89. **2011**, 11, 1032-1035
90. Smalley, J. F.; Feldberg, S. W.; Chidsey, C. E. D.; Linford, M. R.; Newton, M. D.; Liu, Y.-P. *J. Phys. Chem.*, **1995**, 99, 13141-13149.
91. Forster, R. J.; O'Kelly, J. P. *J. Phys. Chem.*, **1996**, 100, 3695-3704.
92. Weber, K. S.; Creager, S. E. *J. Electroanal. Chem.*, **1998**, 458, 17-22.
93. Galka, M. M.; Kraatz, H.-B. *ChemPhysChem*, **2002**, 3, 356-359.
94. Morita, T.; Kimura, S. *J. Am. Chem. Soc.* **2003**, 125, 8732-8733.
95. Bediako-Amoa, I.; Sutherland, T. C.; Li, C.-Z.; Silerova, R.; Kraatz, H.-B. *J.Phys. Chem. B*, **2004**, 108, 704-714.
96. Yang, Y. J.; Khoo, S. B. *Electrochem. Commun.*, **2004**, 6, 87-90.
97. Brevnov, D. A.; Finklea, H. O.; Van Ryswyk, H. *J. Electroanal. Chem.*, **2001**, 500, 100-107.
98. Lambert, C.; Kriegisch, V.; Terfort, A.; Zeysing, B. *J. Electroanal. Chem.*, **2006**, 590, 32-36.
99. Li, J.; Schuler, K.; Creager, S. E. *J. Electrochem. Soc.*, **2000**, 147, 4584-4588.
100. Chang, B.-Y.; Hong, S.-Y.; Yoo, J.-S.; Park, S.-M. *J. Phys. Chem. B*, **2006**, 110, 19386-19392.
101. Sikes, H. D.; Smalley, J. F.; Dudek, S. P.; Cook, A. R.; Newton, M. D.; Chidsey,
102. C. E.; Feldberg, S. W. *Science*, **2001**, 291, 1519-1523.
103. Isied, S. S.; Ogawa, M. Y.; Wishart, J. F., *Chem. Rev.,* **1992**, 92, 381-394.
104. Marcus, R. A., *J. Chem. Phys.*, **1956**, 24, 966-978
105. Marcus, R. A. *J. Chem. Phys.*, **1957**, 26, 872-877.

106. Hush, N. S. *Electrochim. Acta*. **1968**, 13, 1005-1023.

107. Piepho, S. B.; Krausz, E. R.; Schatz, P. N. *J. Am. Chem. Soc.*, **1978**, 100, 2996–3005.

108. Beratan, D. N.; Betts, J. N.; Onuchic, J. N.; *Science*, **1991**, 252, 1285-1288.

109. Bonhote, P.; Gogniat, E.; Tingry, S.; Barbe, C.; Vlachopoulos, N.; Lenzmann, F. *J. Phys. Chem. B*, **1998**, 102, 1498-1507.

110. Papgeorgiou, N.; Gratzel, M.; Enger, O.; Bonifazi, D.; Diederich, F. *J. Phys. Chem. B*, **2002**, 106, 3813-3822.

111. O'Regan, B.; Gratzel, M. *Nature*, 1991, 353, 737.

112. Trammell, S.A.; Meyer, T. J. *J. Phys. Chem. B,* **1999**, 103, 104-107.

113. Forster, R. J.; Keyes, T. E.; Majda, R. *J. Phys. Chem. B*, **2004**, 104, 4425-4432.

114. Lee, W. Y.; Majda, M.; Brezesinski, G.; Wittek, M.; Mobius, D. *J. Phys. Chem. B,* **1999**, 103, 6950-6956.

115. Charych, D. H.; Landau, E. M.; Majda, M. *J. Am. Chem. Soc.*, **1991**, 113, 3340-3346.

116. Widrig, C. A.; Miller, J.; Majda, M. *J. Am. Chem. Soc.*, **1988**, 110, 2009.

117. Miller, C. J.; Widrig, C. A.; Charych, D. H.; Majda, M. *J. Phys. Chem.*, **1988**, 92, 1928-1936.

118. Bardea, A.; Patolsky, F.; Dagan, A.; Willner, I. *Chemical Communications*, **1999**, 21-22.

119. Fan, R.; Yang, J. P.; Cai, L. T.; Price, D. W.; Dirk, S. M.; Kosynkin, D. V. *J. Am. Chem. Soc.*, **2002**, 124, 5550-5560.

120. Fan, R.; Lai, R. Y.; Cornil, J.; Karazi, Y.; Bredas, J. L.; Cai, L. T. *J. Am. Chem. Soc.,* **2004**, 126, 2568-2574.

121. Fan, R.; Yao, Y. X.; Cai, L. T.; Cheng, L.; Tour, J. M.; Bard, A. J. *J. Am. Chem. Soc.*, **2004**, 126, 4035-4042.

122. Ishida, T.; Mizutani, W.; Akiba, U.; Umemura, K.; Inoue, A.; Choi, N. *J. Phys. Chem. B*, **1999**, 103, 16861690.

123. Blauch, D. N.; Saveant, J. M. *J. Am. Chem. Soc.*, **1992,** 114, 3323-3332.

124. Blauch, D. N.; Saveant, J. M. *J. Phys. Chem.*, **1993**, 97, 6444-6448.

125. C. J. Miller, M. Majda, JACS, 1986, 108, 3118.

126. Lee, W.-Y. *J. Phys. Chem. B,* **1999**, 103, 6950-6960.

127. Ruff, I.; Friedrich, V. J. *J. Phys. Chem.*, **1971**, 75, 3297-3302.

128. Ruff, I.; Friedrich, V. J.; Demeter, K.; Csillag, K. *J. Phys. Chem.*, 1971, 75, 3303-3309.

129. Dahms, H. *J. Phys. Chem.*, **1968**, 72, 362-364.

130. Budny, A.; Novak, F.; Plumere, N.; Schetter, B.; Speiser, B.; Straub, D.; Mayer, H. A.; Reginek, M. *Langmuir*, **2006**, 22, 10605-10611.

131. Plumere, N.; Speiser, B. *Electrochim. Acta*, **2007**, 53, 1244-1251.

132. Beasley, C. A.; Murray, R. W. *Langmuir*, **2009**, 25, 10370-10375.

133. Amatore, C.; Bouret, Y.; Maisonhaute, E.; Goldsmith, J. I.; Abruna, H. D. *ChemPhysChem.*, **2001**, 2, 130-134.

134. Amatore, C.; Bouret, Y.; Maisonhaute, E.; Goldsmith, J. I.; Abruna, H. D. *Chem. Eur. J.*, **2001**, 7, 2206-2226.

135. E. P. Plueddemann, Silane Coupling Agents, 2nd Ed., Plenum Press, New York 1991.

136. Bu, H.-Z.; Mikkelsen, S. R.; English, A. M. *Anal. Chem.* **1995**, 67, 4071−4076.

137. Akhoury, A.; Bromberg, L.; Hatton, T. A. *J. Phys. Chem. B* **2013**, 117, 333−342

138. Love, J. C.; Estroff, L. A.; Kriebel, J. K.; Nuzzo, R. G.; Whitesides, G. M. *Chem. Rev.* **2005**, 105, 1103-1169

139. Ito, T.; Forman, S. M.; Cao, C.; Li, F.; Eddy, C. R.; Jr.; Mastro, M.A.; Holm, R.T.; Henry, R.L.; Hohn, K. L.; Edgar, J. H. *Langmuir* **2008**, *24*, 6630-6635

140. Wang, W. K.; Lin, P. C.; Lin, C. H.; Lin, C. K.; Chan, Y.; Chen, G. T.; and Chyi, J. I. *IEEE Electron Dev. Lett.* **2005**, 26, 5-7

Chapter 2 - Analytical Techniques Used in This Research

The thin films, including self assembled monolayer and PS-b-PMMA nanoporous thin films, prepared in this research were characterized by several analytical techniques. Water contact angle measurement were used to qualitatively determine the hydrophobicity of the self-assembled monolayers coated on group III nitride surfaces which reflects the basic properties of the surface such as the packing of the monolayers. UV-vis spectroscopy was used to monitor the photopolymerization of the diacetylenic functional group on the AlGaN surface. The thickness of PS-b-PMMA films spin cast on gold-coated Si wafer was measured by spectroscopic ellipsometry. The surface modification yield of the nanopores has been checked by fluorescence spectroscopy. Atomic force microscopy (AFM) was employed to obtain topographic images of the thin films before and after modification. Cyclic voltammetry (CV) was used in assessing the active surface area of the electrodes fabricated from PS-b-PMMA nanoporous films on gold substrate in NaOH solution. The electron hopping of redox moieties immobilized on the nanoporous cylinder shape PS-b-PMMA films in this research was also determined from CV.

2.1 Contact Angle Goniometry

The contact angle is the angle, conventionally measured through the pure water, where a liquid/vapor interface meets a solid surface. This angle is formed by a liquid, here pure water, at the three phases boundary where liquid, gas, and solid intersect as shown in Figure 2.1. Contact angle goniometry is a technique that allows the measurement of the contact angle formed by a drop of liquid at the point where the solid, liquid and vapor phases intersect. The contact angle θ depends on the interfacial tensions between the liquid/solid (γ_{SL}), the gas/solid (γ_{SG}), and the liquid/gas (γ_{LG}). According to Young's equation (Eq 2.1), which defines the balance of forces caused by a drop of liquid on a solid surface, the contact angle (θ) is a function of the interfacial energies of the three phases.[1]

$$\gamma_{SG} = \gamma_{SL} + \gamma_{LG} \cos \theta \qquad \textbf{Eq 2.1}$$

It is assumed that the droplet fits the geometry of a sphere. The goniometer measures this contact angle θ. θ directly provides information on the interaction energy between surface and liquid. It can be described in term of adhesion vs. cohesion. Adhesion is the force between the liquid molecules and the solid molecules. Cohesion is the force between the liquid molecules that hold the liquid together. A balance of the adhesion and cohesion forces that determine the interfacial surface energies determines the wetting property of a solid. If $\theta \sim 0$ denotes the adhesive forces are dominating, so the droplet spread completely on the solid surface. If θ is very high, cohesive forces are dominating, so the droplet beads up on the solid surface. A highly polar surface possesses a large surface free energy that can overcome the cohesive forces of a liquid and cause it to spread out. In contrast low surface energy substrates cannot overcome this force and display poor wetting properties. In general if $\theta < 90^{o}$ the surface is sufficiently polar or hydrophilic and is wet by the probing liquid and if $\theta > 90^{o}$ the surface is hydrophobic (low surface energy) and the liquid does not wet the surface.

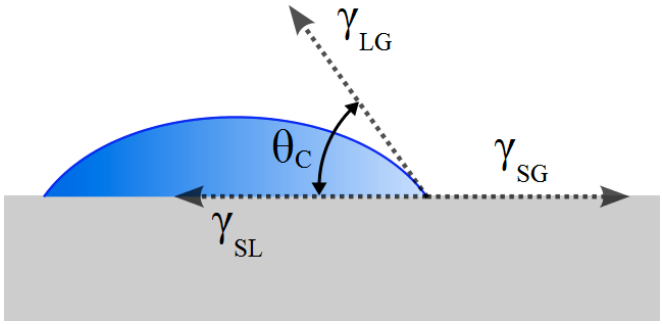

Figure 2.1 Contact angle θ of a Liquid Sample Fitting Young Equation

The contact angles of photopolymerized diacetylenic alkylphosphonic acid self assembled monolayer on AlGaN/GaN substrates have been measured in this research. The AlGaN/GaN substrates were coated with a hydrophilic surface after exposed to UV/O_3 because of the formation of oxygen-containing species at the surface. By coating the surface with self-assembled monolayers, the surface becomes hydrophobic and the surface energy becomes lower. Surface energy quantifies the disruption of intermolecular bonds that occurs when a self-assembled monolayer is created. Surface energy is defined as the excess energy at the surface of a material compared to the bulk. Because the measurement of θ involves the consideration of the behavior of liquid in contact with solids and formation of droplets or thin films, it is referred to as surface energy measurement.

2.2 UV-Vis Spectroscopy[2]

UV-Vis absorption spectroscopy is absorption spectroscopy or reflectance spectroscopy in the ultraviolet-visible spectral region. Perhaps the UV-Vis absorption spectroscopy is one of the simplest forms of spectroscopy because it's a nature process that the sample absorbs the UV and visble light by the sample.

When an atom or molecule absorbed the light in the UV-Vis region, the valence electrons in the atom or the σ, π or nonbonding electrons in the molecule will be excited from one electronic orbital to another. The exact energy of the light required to cause such an electronic transition is highly specific to the chemical or electronic structure of the atom or molecule. So the UV-Vis spectroscopy will provide a way to obtain the chemical information on samples, such as the organization and bonding configuration between atoms.

To quantitatively determine the unknown sample, the concentration of an analyte in solution can be determined by measuring the absorbance at some wavelength and applying the Beer-Lambert Law as shown in Eq 2.2.

$$A = \varepsilon b C \qquad \text{Eq 2.2}$$

Here, the A is absorbance, ε is the molar extinction coefficient ($M^{-1}cm^{-1}$), *b* is the optical path length through the sample (cm) and C is the concentration (M). Absorbance varies as the log of the ratio of incident to transmitted optical power (passing through the sample).

$$A = \log (I_0/I) \qquad \text{Eq 2.3}$$

Since the UV-Vis spectral range is approximately 190 to 900 nm, as defined by the working range of typical commercial UV-Vis spectrophotometers, UV-Vis spectroscopy is useful to characterize the absorption, transmission, and reflectivity of a variety of technologically important materials, such as pigments and coatings,. This more qualitative application usually requires recording at least a portion of the UV-Vis spectrum for characterization of the optical or electronic properties of materials.

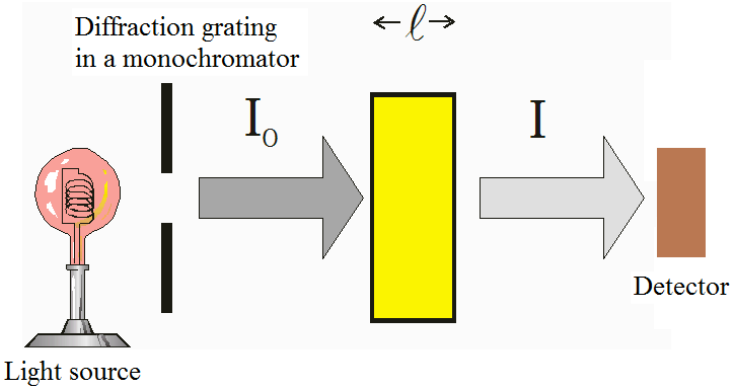

Figure 2.2 Ultraviolet-Visible Spectroscopy

The instrument used in UV-Vis spectroscopy is called a UV-Vis spectrophotometer. The basic parts of a spectrophotometer as shown in Figure 2.2 are a light source, a holder for the sample, a diffraction grating in a monochromator or a prism to separate the different wavelengths of light, and a detector.

2.3 Ellipsometry[3,4]

Ellipsometry is an optical technique for the investigation of the dielectric properties of thin films. Spectroscopic ellipsometry is s very sensitive measurement technique. It provides capabilities for thin films metrology.

Ellipsometry involves the reflection of light from a surface. Consider a model reflective surface coated with a nanofilm of thickness *d* (Figure 2.3). When light passes from one medium to a second medium, some of the light is reflected from the surface and some enters the second medium. When a linearly polarized light reflects off a surface, a phase shift occurs in both the parallel and perpendicular components (i.e., s- and p-polarized components).

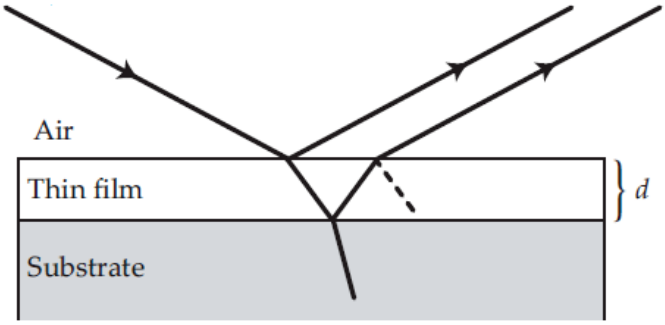

Figure 2.3 Illustration of a thin film on top of a substrate

There may also be an amplitude difference between incident and reflected beams in both components. In fact, the amplitude difference and phase shift are usually not the same for both

components. Thus, the reflected beam is elliptically polarized. The ellipticity depends on the optical properties of the substrate (reflecting surface) as well as the optical properties and thickness of any overlying films. One optical property of importance is the refractive index (RI), also denoted as *n*.

The fundamental equation of ellipsometry can be expressed as Eq 2.3:

$$\rho = r_p / r_s = \tan \Psi e^{i\Delta} \qquad \text{Eq 2.3}$$

Here the optical parameter Δ is defined as the phase difference between the p-polarized and s-polarized components of the incident light upon reflection. In other words, Δ is the resulting change in the phase difference between the s and p waves as the light is reflected from the sample. The second ellipsometric optical parameter ψ is defined as the angle whose tangent is the ratio of the magnitudes of the total reflection coefficients.

Δ and ψ are the experimental quantities measured by the ellipsometer and fitted to a computer model to yield refractive index and film thickness.

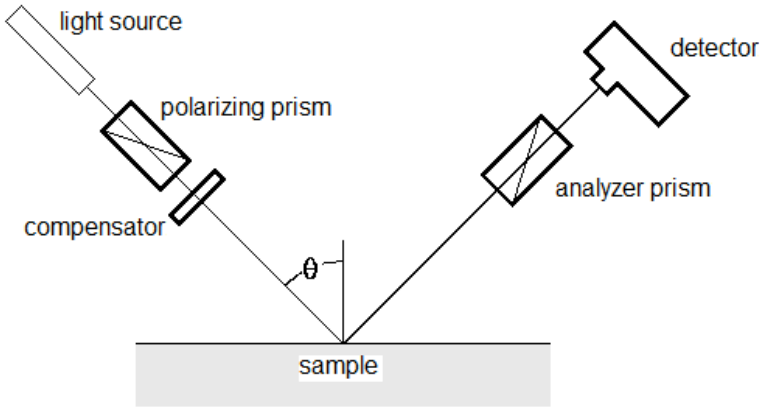

Figure 2.4 Schematic Diagram of Ellipsometer

Figure 2.4 shows the components of an ellipsometer which has a polarizer-compensator-sampleanalyzer-detector configuration. The light source emits an incident light beam with a known polarization state on the sample. According to the properties of the sample, the polarization of the incident beam is changed. The detector detects the change in polarization of the reflected beam of light and experimental results are expressed as Δ and ψ parameters. After an ellipsometric spectrum is generated for the film, a model layer is created to extract parameters such as film thickness and refractive index of the material. The model created should have the correct layer sequence, with values guessed for thickness of all layers, and refractive index. Using an iterative procedure, unknown optical constants and/or thickness parameters are varied,

and Δ and ψ parameters are calculated. The desired film parameters are obtained when the calculated and experimental data match with a minimized mean square error.

2.4 Fluorescence Emission Spectroscopy [5]

Fluorescence spectroscopy is a type of electromagnetic spectroscopy which analyzes fluorescence from a sample. Fluorescence based detection methods are extremely sensitive and have detection limits as low as 10^{-17} M. Therefore, given its extreme sensitivity fluorescence spectroscopy was an ideal detection method for measuring the concentration of the dye molecules released from the PS-b-PMMA nanopore surface in this work.

In fluorescence spectroscopy, the species is first excited, by absorbing a photon, from its ground electronic state to one of the various vibration states in the excited electronic state. Collisions with other molecules cause the excited molecule to lose vibration energy until it reaches the lowest vibration state of the excited electronic state. This process is often visualized with a Jablonski diagram (Figure 2.5).

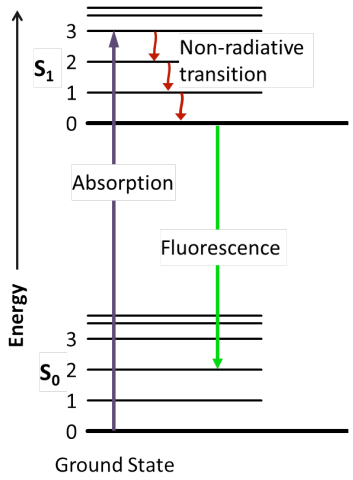

Figure 2.5 Jablonski Diagram Showing Fluorescence Emission

The excited electron relaxes rapidly before coming back to the ground state with reemission of photons. The emitted photons have different energies and thus frequencies because excited molecules may drop down into any of several vibration levels in the ground state. The emitted light is at a longer wavelength than the excitation light which is characteristic of fluorescence. This makes fluorescence a very sensitive method for detection because one can use light of a particular wavelength and detect fluorescence emission at a longer wavelength without any interference from the source light. Furthermore, detection of the emission beam is performed

at right angles to the excitation beam hence the background from the source is further cut down. At low concentrations the fluorescence intensity will generally be proportional to the concentration of the fluorephore in the solution. With the linear relationship between fluorescence intensity and standard fluorophore concentrations, we can get the concentration of the unknown solution with same fluorophore.

2.5 Atomic Force Microscopy[6,7]

Atomic force microscopy (AFM) is a very high-resolution type of scanning probe microscopy whereby a very sharp probe precisely maps the topography of a surface during raster scanning of the surface. AFM is used vastly in surface characterization, imaging and determination of interaction forces between molecules / surfaces of interest. It is also advantageous over electron microscopy, since it can be used in air or solution phase.

AFMs operate by measuring force between a probe and the sample. During the probe close to the surface (within ca. 1 nm), a multitude of interactive forces between the tip apex and the sample surface including adhesion, electrostatic, van der Waals, capillary and repulsive forces depending on the tip-sample distance has been introduced. These forces between the tip and the sample lead to a deflection of the cantilever according to Hooke's law shown in Eq 2.4.

$$F = -k\,x \qquad \text{Eq 2.4}$$

Where F (N) is the elastic force, x (m) is the deflection of the cantilever and k is the spring constant of the cantilever (N/m).

Figure 2.6 shows a typical AFM setup with the force measuring deflection system and the detector. By scanning the probe over the surface the forces of interaction between the tip and the sample are measured as deflections in the cantilever which are translated into motions of the laser beam over the position sensitive diode. As the tips move along the surface, the reflected laser beam will change their direction after strike on a position-sensitive photodetector consisting of four-segment photo-detector. The differences between the segments of photodetector of signals indicate the position of the laser spot on the detector and thus the angular deflections of the cantilever.

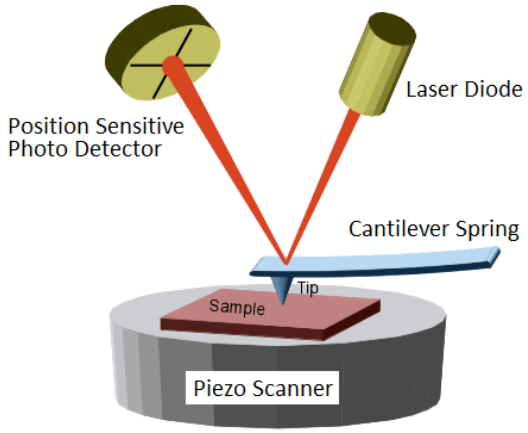

Figure 2.6 Components of AFM

Depending on the application, the AFM can be operated on different modes, named as contact mode, non-contact mode and taping mode. Both contact mode and tapping mode have been used in this research.

In the contact mode operation, the static tip deflection is used as a feedback signal. Because the measurement of a static signal is prone to noise and drift, low stiffness cantilevers are used to boost the deflection signal. In contact mode, the force between the tip and the surface is kept constant during scanning by maintaining a constant deflection.

In tapping mode, the cantilever is driven to oscillate up and down at near its resonance frequency. When the tip comes close to the surface, forces such as van der Waals force, dipole-dipole interaction and also electrostatic forces act on the cantilever and cause the amplitude of the oscillation to decrease as the tip gets closer to the sample. The piezoelectric controls the height of the cantilever above the sample. The height is adjusted to maintain a set cantilever oscillation amplitude as the cantilever is scanned over the sample. Therefore, a tapping AFM image is produced by imaging the force of the oscillating contacts of the tip with the sample surface.

2.6 Cyclic Voltammetry[8]

Redox-involved surface electron transport has been studied since 80's using different systems. Cyclic voltammetry is the most widely used technique for acquiring the information about electrochemical reactions. It also provides a way to determine the dynamics of electron transport occurring on redox-involved systems.

Cyclic voltammetry involves the measurement of current as a function of a varying potential. In electrochemistry experiments, two types of currents are measured including faradaic current and nonfaradaic current. The nonfaradaic current is not involving any chemical reactions. It only causes accumulation or removal of electrical charges on the electrode and the electrolyte solution interface. The faradaic current originates from the redox reaction. In most cases, faradaic current is discussed. The nonfaradaic is often considered to be a background signal. To accurately measure the faradaic current, the nonfaradiaic current needs to be subtracted from the total current.

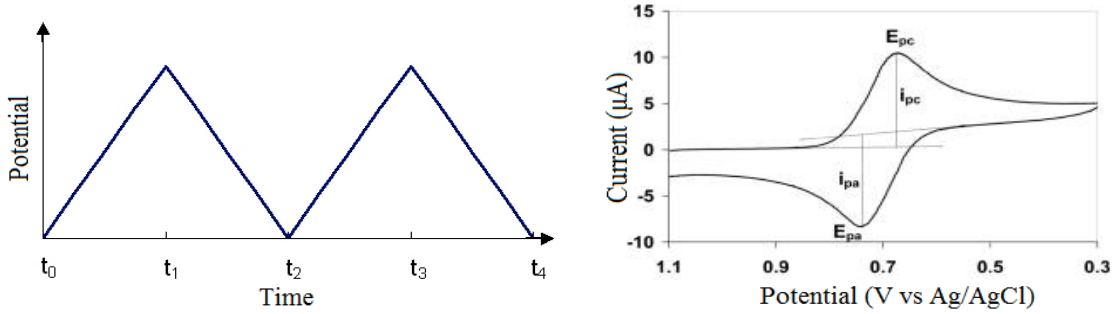

Figure 2.7 (a) Cyclic potential sweep and (b) resulting cyclic voltammogram

In order to measure current and potential simultaneously, three electrodes are required. The reference electrode is typically a half-cell with a standard electrochemical potential. A platinum wire is used as a counter electrode, and a nanoporous thin film derived gold surface is incorporated as a working electrode. To measure a voltammogram, the current flow between the working electrode and counter electrode is recorded as a sawtooth potential is applied to the working electrode. At the same time, the magnitude of the resulting potential is measured between the working and reference electrodes. The typical reversible cyclic voltammogram is shown in the Figure 2.7.

In a typical CV experiment, the redox current is determined by several factors such as the reactant concentration, electrode area, the diffusion coefficient and electron transfer rate constant of the reactant, and potential sweep rate. In this research, we will consider two cases: adsorbed cases at low scan rate and diffusion-limited case at high scan rate. In both cases, redox current is proportional to reactant concentration and electrode area, but will change differently with increasing potential scan rate. So, here CV measurements at different scan rates provide a way to determine which case is dominant in the measured redox current.

For diffusion-limited case, during the CV measurements, the electrode and solution are static, the species being oxidized or reduced at the electrode surface is obviously depleted in the region nearest the electrode. As the potential is scanned past the redox potential of the species, the current increases and then decreases as all the reactant is used up near the electrode. For the potential sweep in the cathodic (or anodic) direction, the analyte is reduced (or oxidized) at the electrode. Upon sweep reversal, the reduced analyte is reoxidized or rereduced. Hence, positive and negative current peaks are obtained, which means the electron transfer between the reactant and electrode occurs instantly without any side reactions. Thus, as the potential of the working electrode is swept back and forth, a cyclic voltammogram similar to that shown in Figure 2.6 (b) will recorded. The peak current is given by:

$$i_p = (2.69 \times 10^5)\, n^{3/2} A D^{1/2} v^{1/2} C \qquad \text{Eq 2.5}$$

In this equation, n is the number of electrons, A is the area of the electrode, D is the diffusion coefficient of the redox species, and C is the concentration of the redox species.

In the case that the redox species observed in an electrochemical experiment adsorbed to the electrode surface, the peak current can be expressed as:

$$i_p = n^2 F^2 A\, \Gamma_c\, v/4RT \qquad \text{Eq 2.6}$$

In this equation, n is the stoichiometric number of the moles of electrons involved in the redox process, F is Faraday's constant (96,485 C/mol), A is the electrode area in cm2, Γ_c is the electroactive surface coverage, v is the scan rate, R is molar gas constant and T is temperature.

Here, a three electrode cell set up consisting of a working electrode recessed nanoporous array electrode of PS-b-PMMA film chemically modified with redox moieties in the cylindrical inner wall, a reference electrode (Ag/ AgCl, 3M KCl) and a counter electrode (Pt wire) was used.

References

1. Hunter, R. J., Ed.; In Foundations of Colloid Science; Oxford University Press: New York, 2002; , pp 1-787.
2. Chaniotakis, N.; Sofikiti, N. *Anal. Chim. Acta* **2008**, *615*, 1-9.
3. Tompkins, H. G.; Irene, E. A., Eds.; In Handbook of Ellipsometry; William Andrew Publishing/Noyes: 2005 .
4. Mrstik, B. J.; McMarr, P. J.; Blanco, J. R.; Bennett, J. M. *J. Electrochem. Soc.* **1991**, 138, 1770-1778.
5. Sassolas, A.; Leca-Bouvier, B. D.; Blum, L. J. *Chem. Rev.* **2008***, 108*, 109-139.
6. Humphris, A. D. L.; Miles, M. J., Hobbs J. K., *Applied Physics Letters,* **2005**, *86*, 034106.
7. Giessibl F., *Advances in Atomic Force Microscopy, Reviews of Modern Physics*, **2003**, 75(3), 949-983.
8. Bard, A. J.; Faulkner, L. R., Eds.; In *Electrochemical Methods, Fundamentals and Applications;* Bard, A. J., Faulkner, L. R., Eds.; Wiley: New York, 2001; Vol. 2nd.

Chapter 3 - Photopolymerization of Self-Assembled Monolayers of Diacetylenic Alkylphosphonic Acids on Group-III Nitride Substrates

Reproduced by permission of The American Chemical Society

Published as: Li, F., Shishkin, E., Mastro, M. M., Hite, J. K., Eddy, C. R., Jr., Edgar, J. H., Ito, T. *Langmuir.* **2010**, *26(13)*, 10725-10730

3.1. Introduction

This chapter reports the properties of diacetylenic alkylphosphonate self-assembled monolayers (SAMs) on UV/O_3-treated, metal-polar group-III nitride substrates. These SAMs were characterized using contact angle goniometry, transmission visible absorption spectroscopy and atomic force microscopy (AFM). Alkylphosphonate SAMs were formed on an $Al_xGa_{1-x}N$ (AlGaN) substrate, as with GaN, upon immersion in a toluene solution of an alkylphosphonic acid. A series of diacetylenic alkylphosphonic acids were synthesized to study the effects of crosslinking positions within the SAMs on their photopolymerization efficiency. Visible absorption spectra suggested that UV irradiation initially led to the photopolymerization of adjacent conjugated diacetylene groups in a SAM and then to the degradation of the crosslinked moieties, which was correlated to the stability of the SAM in 0.1 M NaOH.

Because of their unique electrical properties, low toxicity and excellent chemical/physical stability, group-III nitride semiconductors, such as GaN and AlGaN, are employed in chemical and biological sensors.[1-3] These sensors measure changes in their electrical properties induced by the adsorption of analytes onto nitride's surface. Oxide-coated GaN and AlGaN could be used for fabricating a pH sensor because of the high affinity of its surface to OH^- and/or H^+.[1, 4-7] In addition, the selectivity and sensitivity of a nitrides-based sensor can be tailored by modifying the nitride's surface with a thin layer that selectively recognizes chemical species of interest.[3] For example, organosilane SAMs with terminal binding moieties were immobilized directly onto AlGaN surface in the gate region to control the detection selectivity of AlGaN-based transistor-type sensors.[8-11] However, formation of thick polymer layers due to the high reactivity of

organosilanes with water and also the hydrolysis of organosilane SAMs at basic pH[12, 13] can deteriorate the reproducibility of the sensor performance. Thiolate SAMs[14] were more commonly used to develop AlGaN-based chemical and biological sensors for various chemical and biological analytes.[3, 15, 16] These SAMs could be immobilized on the gold-coated gate of an AlGaN-based transistor by simpler procedures without multilayer formation. However, the thin gold layer deposited on an AlGaN gate reduced the detection sensitivity of the transistor-type sensors.

It was previously reported by us[17, 18] and other researchers[19] that oxide-coated GaN substrates could be directly modified with SAMs of *n*-octadecylphosphonic acid (ODPA). The SAM formation was shown by their large water contact angle (103 - 109 °),[17, 18] ellipsometric thickness (ca. 2.4 nm),[18] XPS spectra,[18-20] and FTIR spectra.[19] In our previous reports,[18] ODPA SAMs were formed by soaking a UV/O_3-treated GaN in its organic solution regardless of the GaN polarity or dopant concentration. In contrast, primary substituted hydrocarbons with terminal -OH, -SH, -NH_2 and -COOH groups did not strongly adsorb onto GaN substrates.[18] The weak adsorption of -NH_2 and -COOH groups will allow us to modify GaN surface with organophosphonate SAMs having these terminal functional groups that can be used as linkers of other functional moieties such as antibodies. However, ODPA SAMs desorbed from GaN substrates upon immersion in aqueous solution, especially in basic solution, probably reflecting the high solubility of deprotonated ODPA in the solution,[18] the electrostatic repulsion between the negatively-charged ODPA and substrate surface,[18] and/or the dissolution of the gallium oxide layer.[19] The stability of a SAM in aqueous solution, which is required for its future applications to chemical and biological sensors, may be improved by crosslinking molecules in the SAM.[12]

In this study, we prepared SAMs of diacetylenic alkylphosphonic acids ($CH_3(CH_2)_n$-C≡C-C≡C-$(CH_2)_m$PO$(OH)_2$; **1a**–**1c** in **Scheme 3.1**) on GaN and AlGaN substrates and investigated their UV-initiated polymerization behavior and their stability in basic solution. These molecules have the same chain length (i.e., $m + n$ = constant) and a conjugated diacetylene moiety at different positions. A conjugated diacetylene was chosen as a polymerization moiety, because its photopolymerization was widely investigated to improve the physical and chemical stability of nanoscale molecular assemblies,[21, 22] Langmuir-Blodgett (LB) films,[12, 22-27] and SAMs.[28, 29] The polymerization of diacetylenic moieties occurs by simply irradiating with 254-nm UV light, although it requires well-ordered molecular packing, which is known as topochemical

polymerization.[12, 21, 22, 27] The high chemical stability of polydiacetylenes, in addition to the selective photopolymerization at the UV-irradiated area, made it possible to apply diacetylenic SAMs as ultrathin photoresists in photolithography.[30] Diacetylenic SAMs with terminal functionalities were prepared to fabricate controlled multilayers[31, 32] and also to covalently immobilize chemical and biological recognition moieties.[33] In addition, polydiacetylenes have unique optical properties, leading to their applications for optical electronic devices and chemical/biological sensors.[22, 33, 34] The combination of the unique optical and electric properties of GaN/AlGaN and diacetylenic SAMs may thus provide a means for developing unique chemical and biological sensing devices.

3.2. Experimental Section

3.2.1. Chemicals and Materials

1,3-Dibromopropane ($C_3H_6Br_2$; Alfa Aesar), 1,6-dibromohexane ($C_6H_{12}Br_2$; Aldrich), 1,9-dibromononane ($C_9H_{18}Br_2$; Aldrich), 1,4-bis(trimethylsilyl)-1,3-butadiyne ($C_{10}H_{18}Si_2$; Aldrich), 1-bromohexane ($C_6H_{13}Br$; Aldrich), 1-bromononane ($C_9H_{19}Br$; Aldrich), 1-bromododecane ($C_{12}H_{25}Br$; Acros Organics), hexamethylphosphoric triamide (HMPA, MP Biomedicals), methyllithium-lithium bromide complex (Acros Organics), *n*-butyllithium (Acros Organics), trimethylsilylbromide (C_3H_9SiBr; Aldrich), potassium fluoride dihydrate (Allied Chemical), triethyl phosphite ($(C_2H_5O)_3P$; Aldrich), *n*-octadecanol ($C_{18}H_{37}OH$; Alfa Aesar), *n*-hexadecyl mercaptan ($C_{16}H_{33}SH$; Acros Organics), *n*-octadecylamine ($C_{18}H_{37}NH_2$; Alfa Aesar), *n*-octadecanoic acid ($C_{17}H_{35}COOH$; Aldrich), *n*-octadecylphosphonic acid ($C_{18}H_{37}PO(OH)_2$, ODPA; Alfa Aesar), *N*,*N*-dimethylformamide (Fisher), and sodium hydroxide (Fisher) were used as received. Tetrahydrofuran (THF) (Fisher) was dried by distillation from Na. CH_2Cl_2 was dried by distillation from CaH_2. All aqueous solutions were prepared with water having a resistance of 18 MΩ cm or higher (Barnstead Nanopure Systems). GaN epiwafers (GaN layer thickness ~ 3 μm; on single-side polished sapphire wafers), $Al_{0.2}Ga_{0.8}N$ epiwafers (AlGaN layer thickness ~ 1 μm; on double-side polished sapphire wafers), and $Al_{0.25}Ga_{0.75}N$ epiwafers (AlGaN layer thickness ~ 1 μm; on double-side polished sapphire wafers) were prepared via metalorganic chemical vapor deposition (MOCVD) using thin (ca. 25-35 nm thick) aluminum nitride nucleation layers on commercial *a*-plane sapphire substrates. All GaN and AlGaN samples were

c-plane, i.e., (0001), oriented, metal- (i.e., Ga- or AlGa-) polar, and unintentionally-doped. Details of the growth method are described elsewhere.[35]

3.2.2. Synthesis of Diacetylenic Alkylphosphonic Acids (1a–1c; Scheme 1)

^{1}H- and ^{13}C-NMR spectra were measured on a Varian INOVA 400 Fourier transform NMR spectrometer (400 MHz), and chemical shifts were reported in δ values in ppm downfield of tetramethylsilane. IR spectra were measured on a Nicolet Protege 640 spectrophotometer. Exact MS data were measured at the Mass Spectroscopy Laboratory, University of Kansas.

Scheme 3.1 Synthesis of Diacetylenic Alkylphosphonic Acids

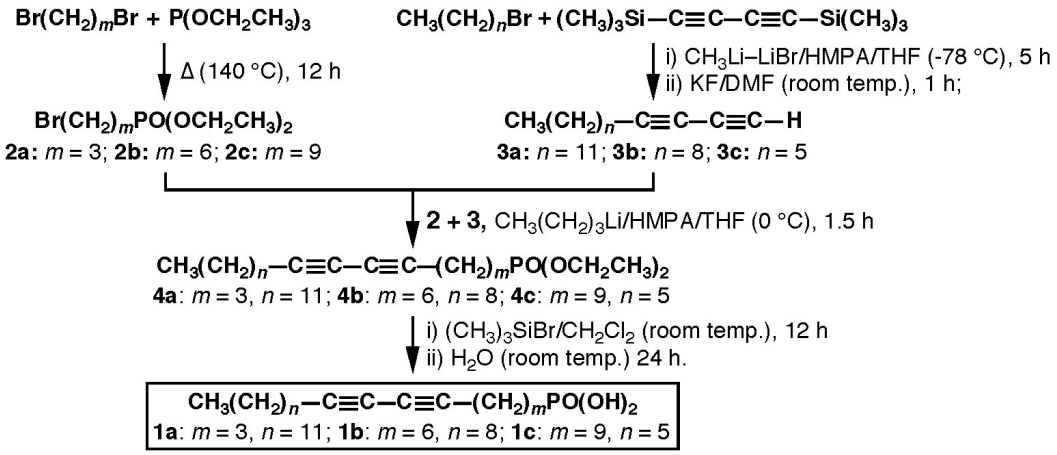

3.2.2.1. Synthesis of Diethyl (ω-bromoalkyl)phosphonates (2a–2c in Scheme 3.1)[36]

The mixture of triethyl phosphite (10 mmol) with alkyl dibromide (10 mmol) was heated at 140 °C for overnight. After cooling to room temperature, the reaction mixture was purified by silica gel column chromatography (elution with pure CH_2Cl_2, then 1:15 petroleum ether/ ethyl acetate) to give colorless oil. Diethyl (3-bromopropyl) phosphonate (**2a**): yield 87%. ^{1}H NMR ($CDCl_3$) δ 4.10 (q, J = 6.0 Hz, 4H, OCH_2), 3.48 (t, J = 6.4 Hz, 2H, $BrCH_2$), 2.15 (m, 2H, CH_2), 1.93 (m, 2H, CH_2), 1.36 (t, J = 6.8 Hz, 6H, CH_3). ^{13}C NMR ($CDCl_3$) δ 61.89 (d, J = 6 Hz), 33.87(d, J = 19 Hz), 26.15 (d, J = 4 Hz), 24.59 (d, J = 142 Hz), 16.67 (d, J = 6 Hz). IR (cm^{-1}): 2979, 2929, 2855, 1464, 1458, 1441, 1391, 1246, 1165, 1097, 1057, 1030, 959, 786, 645. Diethyl (6-bromohexyl) phosphonate (**2b**): yield 89%. ^{1}H NMR ($CDCl_3$) δ 4.11 (q, J = 7.2 Hz, 4H, OCH_2), 3.41 (t, J = 6.8 Hz, 2H, $BrCH_2$), 1.9-1.4 (m, 10H, $(CH_2)_5$), 1.35 (t, J = 7.2 Hz, 6H, CH_3). ^{13}C NMR ($CDCl_3$) δ 61.62 (d, J = 7 Hz), 33.97 (d, J = 9 Hz), 32.67 (d, J = 5 Hz), 29.88 (d, J = 17 Hz), 27.67 (d, J = 35 Hz), 25.78 (d, J = 140 Hz), 22.52, 16.70 (d, J = 6 Hz). IR (cm^{-1}):

2980, 2935, 2863, 1457, 1443, 1392, 1369, 1241, 1164, 1098, 1056, 1027, 962, 799, 642. Diethyl (9-bromononyl) phosphonate (**2c**): yield 90%. ^{1}H NMR ($CDCl_3$) δ 4.10(q, J = 6.8 Hz, 4H, OCH_2), 3.41 (t, J = 6.8 Hz, 2H, $BrCH_2$), 1.9-1.3 (m, 16H, $(CH_2)_8$), 1.34 (t, J = 6.4 Hz, 6H, CH_3); ^{13}C NMR ($CDCl_3$) δ 61.57 (d, J = 6 Hz), 34.27, 32.96, 30.76 (d, J = 17 Hz), 29.36, 29.18, 28.88, 28.30, 26.56, 25.15, 22.60, 16.70. IR (cm^{-1}): 2980, 2929, 2855, 1465, 1458, 1442, 1391, 1369, 1247, 1164, 1098, 1057, 1029, 958, 786, 644.

3.2.2.2. Synthesis of 1,3-Alkadiynes (3a–3c in Scheme 3.1)[37, 38]

An ether solution of methyllithium-lithium bromide complex (6.7 mL; 10 mmol) was added dropwise to a solution of 1,4-bis(trimethylsilyl)-1,3-butadiyne (10 mmol) in anhydrous THF (20 mL) at –78 °C, and stirred for 5 hours at room temperature under argon protection. Subsequently, 1-bromoalkane (12 mmol) in fresh distilled HMPA (20 mL) was added dropwise at –78 °C, and stirred for 30 min at room temperature. After the pH was adjusted to 7.0 by adding 3 M HCl at 0 °C, the mixture was extracted with ethyl acetate. After the solvent was evaporated, potassium fluoride dihydrate (20 mmol) in DMF (20 mL) was added, stirred for 1 hour at room temperature, poured into 3 M HCl (15 mL) with stirring at 0 °C, and then extracted with ethyl acetate. The organic layer was washed with 3 M HCl, brine, saturated $NaHCO_3$ solution, saturated NaCl solution, and dried over $MgSO_4$. Removal of the solvent gave a brown liquid, which was used for next step directly.

3.2.2.3. Synthesis of Diethyl Alkadiyn-1-phosphonates (4a–4c in Scheme 3.1)

To crude 1,3-alkadiyne **(3**; nominally 2.0 mmol**)** in anhydrous THF (8 mL) was added dropwise 1.5 mL of *n*-butyllithium (a 1.6 M solution in hexane; 2.4 mmol) at 0 °C. The reaction mixture was stirred for 1 hour at 0 °C under argon, and then a HMPA solution (8 mL) of diethyl (ω-bromoalkyl)phosphonate (**2**; 2.4 mmol) was added. The mixture was stirred for 30 min at 0 °C and then for 2 hours at room temperature followed by extraction with ethyl acetate. The organic layer was washed with saturated $NaHCO_3$ solution, water, saturated NaCl solution, dried over $MgSO_4$, and then the solvent was evaporated. The crude product was purified by silica gel column chromatography with 20:1 ethyl acetate/hexane as eluent to give light-yellow liquid. 4, 6-Nonadecadiyn-1-phosphonate (**4a**): yield 72% ^{1}H NMR ($CDCl_3$) δ 4.08 (q, J = 6.4 Hz, 4H, OCH_2), 2.24 (t, J = 6.8 Hz, 4H, C-CH_2), 1.8-1.2 (m, 30H, CH_2 and $OCH_2C\underline{H}_3$), 0.90 (t, J = 6.8 Hz, 3H, CH_3). ^{13}C NMR ($CDCl_3$) δ 65.39, 65.33, 61.56, 61.50, 32.02, 30.86, 30.71, 29.62, 29.46,

29.41, 29.29, 29.23, 29.06, 28.99, 28.53 (d, J = 6 Hz), 26.57, 25.16, 22.90, 22.60 (d, J = 3 Hz), 19.35, 16.67 (d, J = 6 Hz). IR (cm^{-1}): 2977, 2928, 2854, 1456, 1391, 1248, 1164, 1099, 1058, 1029, 960, 815, 788, 722. 7, 9-Nonadecadiyn-1-phosphonate (**4b**): yield 75%. ^{1}H NMR ($CDCl_3$) δ 4.11 (q, J = 6.8 Hz, 4H, OCH_2), 2.23 (t, J = 6.8 Hz, 4H, C-CH_2), 1.8-1.3 (m, 30H, CH_2 and $OCH_2C\underline{H}_3$), 0.90 (t, J = 6.8 Hz, 3H, CH_3). ^{13}C NMR ($CDCl_3$) δ 65.42, 65.36, 61.59, 61.53, 32.05, 30.86, 30.71, 29.64, 29.47, 29.40, 29.30, 29.24, 29.06, 28.99, 28.53 (d, J = 6 Hz), 26.57, 25.17, 22.87, 22.70 (d, J = 3 Hz), 19.39, 16.70 (d, J = 7 Hz). IR (cm^{-1}): 2979, 2929, 2855, 1457, 1392, 1244, 1164, 1097, 1057, 1031, 960, 818, 786, 702. 10, 12-Nonadecadiyn-1-phosphonate (**4c**): yield 62%. ^{1}H NMR ($CDCl_3$) δ 4.10 (q, J = 7.2 Hz, 4H, OCH_2), 2.24 (t, J = 6.8 Hz, 4H, C-CH_2), 1.8-1.2 (m, 30H, CH_2 and $OCH_2C\underline{H}_3$), 0.90 (t, 6.8Hz, 3H, CH_3). ^{13}C NMR ($CDCl_3$) δ 65.42, 65.37, 61.59, 61.53, 32.07, 30.86, 30.71, 29.64, 29.47, 29.41, 29.30, 29.24, 29.06, 28.99, 28.53 (d, J = 6 Hz), 26.54, 25.15, 22.87, 22.59 (d, J = 3 Hz), 19.32, 16.70 (d, J = 7 Hz). IR (cm^{-1}): 2979, 2927, 2855, 1465, 1391, 1245, 1164, 1098, 1058, 1030, 959, 824, 788, 723.

3.2.2.4. Synthesis of Diacetylenic Alkylphosphonic Acids (Alkadiyn-1-phosphonic Acids; 1a–1c in Scheme 3.1)[39]

Trimethylsilylbromide (1.56 mmol) was added to an anhydrous CH_2Cl_2 solution (5 mL) of diethyl alkadiyn-1-phosphonate (**4**, 0.26 mmol) at 0 °C, and then stirred overnight at room temperature. After the solvent was evaporated under reduced pressure, water (15 mL) was added and stirred for 24 hours. The reaction mixture was extracted with ethyl acetate, washed with water, saturated NaCl solution, and then dried over $MgSO_4$. Removal of the solvent gave white solid. 4, 6-Nonadecadiyn-1-phosphonic acid (**1a**): yield (from **4a**) 79%. ^{1}H NMR ($CDCl_3$) δ 2.9 (br, OH), 2.26 (t, J = 7.2 Hz, 4H, C-CH_2), 1.8-1.2 (m, 24H, CH_2), 0.89 (t, J = 6.4 Hz, 3H, CH_3). ^{13}C NMR ($CDCl_3$) δ 65.63, 65.39, 32.07, 29.64, 29.48, 29.30, 29.06, 28.54, 22.88, 19.40, 14.33. IR (cm^{-1}): 2955, 2922, 2849, 1465, 1419, 1340, 1293, 1233, 1223, 1070, 1009, 989, 938, 724. Exact MS: *m/z* calculated for $C_{19}H_{32}O_3P$ (M – H), 339.2089; found 339.2080. 7, 9-Nonadecadiyn-1-phosphonic acid (**1b**): yield (from **4b**) 82%. ^{1}H NMR ($CDCl_3$) δ 2.23 (t, J = 6.8 Hz, 4H, C-CH_2), 1.8-1.2 (m, 24H, CH_2), 0.89 (t, J = 6.4 Hz, 3H, CH_3). ^{13}C NMR ($CDCl_3$) δ 65.54, 65.38, 32.10, 29.65, 29.49, 29.31, 29.25, 29.10, 29.03, 28.59, 22.89, 19.41, 14.34. IR (cm^{-1}): 2955, 2921, 2849, 1465, 1420, 1340, 1293, 1232, 1223, 1065, 1009, 989, 938, 723. Exact MS: *m/z* calculated for $C_{19}H_{34}O_3P$ (M – H), 339.2089; found 339.2089. 10, 12-Nonadecadiyn-1-phosphonic acid (**1c**): yield (from **4c**) 79%. ^{1}H NMR ($CDCl_3$) δ 2.24 (t, J = 6.4 Hz, 4H, C-CH_2),

1.8-1.2 (m, 24H, CH_2), 0.88 (t, J = 6.4 Hz, 3H, CH_3). ^{13}C NMR ($CDCl_3$) δ 65.60, 65.31, 32.07, 29.66, 29.49, 29.31, 29.22, 29.06, 29.00, 28.55, 22.65, 19.41, 14.35. IR (cm^{-1}): 2954, 2920, 2848, 1464, 1420, 1342, 1293, 1233, 1222, 1072, 1011, 989, 935, 727; Exact MS: *m/z* calculated for $C_{19}H_{32}O_3P$ (M + H), 341.2246; found 341.2242.

3.2.3. Preparation and Characterization of Group-III Nitride Samples

Group-III nitride samples coated with phosphonate SAMs were prepared according to our previous report.[18] In short, GaN or AlGaN substrates (ca. 5 x 5 mm^2) were soaked in 50% HCl for 1 min, rinsed with water, dried under an Ar stream, and then treated by UV/O_3 for 30 min in a Novascan PSD-UVT UV/ozone system. The resulting UV/O_3-treated substrates were immersed in a 0.1 mM toluene solution of an organic compound for 17 hours, thoroughly washed with toluene, and dried under an Ar stream. Diacetylenic alkylphosphonate SAMs were polymerized with a low intensity UV lamp (Spectronics Model EF-180, 254 nm, 1.9 mW cm^{-2} at 25 cm) at a distance of 10 cm in an Ar-purged glove bag. Water contact angles on group-III nitride samples were measured using a PG-1 pocket contact angle goniometer by reading contact angle values of the two sides of a drop (2 μL) within 30 s after deposition of the drop. To study the stability of diacetylenic alkylphosphonate SAMs on group-III nitrides, SAM-coated substrates were immersed in 0.1 M NaOH for 10–240 min at room temperature, quickly washed with water, and dried under an Ar stream, and their water contact angles were measured. Transmission visible absorption spectra of diacetylenic alkylphosphonate SAMs on $Al_{0.25}Ga_{0.75}N$ substrates deposited onto double-side polished sapphire wafers were recorded on a Varian *Cary*500 Spectrophotometer. A UV/O_3-treated substrate was used as a reference, and diacetylenic alkylphosphonate SAMs on the AlGaN after UV irradiation for 0, 2, 5, 6, 8 or 10 min were used as samples. Contact mode AFM images were obtained by contact-mode imaging in air, using a digital instruments multimode AFM with Nanoscope IIIa electronics. Contact-mode pyramidal AFM tips were purchased from Veeco (Model NP-10).

3.3. Results and Discussion

3.3.1. Water Contact Angle Measurements of GaN and AlGaN Substrate Surfaces after the Adsorption of a Primary Substituted Hydrocarbon

Prior to investigating the properties of diacetylenic alkylphosphonate SAMs, adsorption of primary substituted hydrocarbons with different terminal functional groups (-OH, -SH, -NH_2, -COOH or -$PO(OH)_2$) onto GaN and AlGaN (x = 0.2, 0.25) was assessed by measuring water contact angle (θ^{water}). We previously reported the essential contribution of hydrogen bond interactions between polar functional groups and surface oxide layers to the adsorption of these compounds onto GaN substrates.[17, 18] Considering that the chemical properties (e.g., hydrogen bond acidity and basicity) of a surface oxide layer would be altered according to the substrate composition, the surfaces of group-III nitride substrates with different Al/Ga ratios may exhibit different adsorptivities of these compounds.

Just after UV/O_3 treatment, the surfaces of AlGaN substrates were hydrophilic (θ^{water} < 15°), as with UV/O_3-treated GaN surfaces,[17, 18] suggesting the formation of a hydrophilic surface oxide layer. After immersion in a 0.1 mM toluene solution for 17 hours, which were long enough to reach the adsorption equilibrium, the θ^{water} of AlGaN surfaces increased (Table 3.1) due to the adsorption of a primary substituted hydrocarbon onto the surfaces. Regardless of the substrates, the adsorption of n-$C_{18}H_{37}PO(OH)_2$ (ODPA) resulted in hydrophobic surfaces with very high θ^{water} values (> 100°), suggesting ODPA SAM formation on these substrates probably due to the strong hydrogen bond acidity/basicity of the -$PO(OH)_2$ group.[18] In contrast, the other four compounds did not strongly adsorb onto the substrates, as shown by the much lower θ^{water} values (< 80°, Table 3.1). Interestingly, the θ^{water} values of AlGaN substrates upon the adsorption of these four compounds were significantly smaller than those of GaN substrates. In addition, the difference in θ^{water} values between n-$C_{17}H_{35}COOH$ and n-$C_{18}H_{37}NH_2$ was larger on AlGaN as compared to GaN.

Table 3.1 Water Contact Angle (deg)a of Chemical Modified Group-III Nitride Substrates.[b]

	GaN	$Al_{0.2}Ga_{0.8}N$	$Al_{0.25}Ga_{0.75}N$
n-$C_{18}H_{37}OH$	72.7 ± 1.2	63.3 ± 3.1	62.6 ± 1.6
n-$C_{16}H_{33}SH$	71.7 ± 0.8	54.8 ± 1.3	56.7 ± 1.0
n-$C_{18}H_{37}NH_2$	71.7 ± 1.4	63.1 ± 0.8	61.2 ± 2.2
n-$C_{17}H_{35}COOH$	75.0 ± 1.3	70.2 ± 0.7	67.2 ± 3.7
n-$C_{18}H_{37}PO(OH)_2$	104.9 ± 1.2	103.1 ± 0.4	102.9 ± 0.1

[a] Average ± standard deviation from three separate samples. [b] Substrates treated in a UV/O_3 cleaner for 30 min were immersed in a 0.1mM toluene solution for 17 hours.

The different molecular adsorption behavior between UV/O_3-treated GaN and AlGaN substrates may be explained on the basis of the basis of the difference in their surface chemical compositions. The oxide layer on AlGaN surface would consist of the mixture of Al_2O_3 and Ga_2O_3,[40] whereas that on GaN consists only of Ga_2O_3.[41-43] The lower adsorptivity (i.e., smaller θ^{water}) of UV/O_3-treated AlGaN substrates may reflect the lower surface density of hydrogen bonding sites on Al_2O_3 as compared to Ga_2O_3.[44] The stronger adsorption of acidic *n*-$C_{17}H_{35}COOH$ on the AlGaN substrates over basic *n*-$C_{18}H_{37}NH_2$ is probably due to the higher basicity and much lower acidity of Al_2O_3 surface.[44, 45] These θ^{water} values of the ODPA SAMs on GaN and AlGaN were smaller than those previously reported on the Al_2O_3 surface of sputtered Al.[46] The larger θ^{water} values in the literature may reflect the larger surface roughness of the Al substrates and may also be due to the use of a different method, the dynamic Wilhelmy method. Indeed, our θ^{water} value of the ODPA SAMs on single-crystal sapphire substrates was 103°, close to our θ^{water} values on GaN and AGaN.

3.3.2. Comparison of the Stability of Diacetylenic Alkylphosphonate SAMs on GaN in Basic Solution before and after UV Irradiation

The above results suggest that ODPA SAMs can be formed on UV/O_3-treated GaN and AlGaN substrates. As with ODPA (Table 3.1), the θ^{water} values of GaN and AlGaN substrates were similarly high (102–104°) were similarly observed after immersion in a toluene solution

containing one of diacetylenic alkylphosphonic acids (**1a**–**1c**). The high θ^{water} values suggest the SAM formation of diacetylenic alkylphosphonic acids on GaN and AlGaN substrates,[18] permitting us to employ these substrates for investigating the properties of diacetylenic alkylphosphonate SAMs.

However, these SAMs without UV irradiation desorbed from the substrates upon immersing in 0.1 M NaOH, as reported for ODPA SAMs on GaN[18, 19] and Al_2O_3.[46] For example, Figure 3.1 (open circles) shows the θ^{water} values of **1b**-coated GaN substrates at different immersion times. Within 10 min, the θ^{water} values decreased from 103° to ca. 65°, and then did not change upon immersion for an extended time. In contrast, the desorption of **1b**-SAMs on GaN substrates in 0.1 M NaOH was reduced by UV irradiation at 254 nm (Figure 3.1, filled circles). The UV irradiation led to a slight decrease in θ^{water} from 103° to 96°, as shown by the data at t = 0 min. The θ^{water} of SAMs of **1a**–**1c** on GaN and AlGaN similarly decreased upon UV irradiation from 102–104° to 95–96°, maybe due to changes in molecular packing and/or partial degradation of the SAMs induced by the UV light.[47] More importantly, after the initial decrease from 96° within the first 10 min, the θ^{water} values did not change to be *ca.* 82° upon prolonged immersion in 0.1 M NaOH. The significantly higher plateau θ^{water} values of UV-irradiated SAMs would indicate the improved chemical stability of the SAMs due to the photopolymerization of the conjugated diacetylene moieties. On the other hand, the decrease in θ^{water} for the first 10-min immersion may result from the partial desorption of molecules at defect sites in the SAM (*vide infra*).

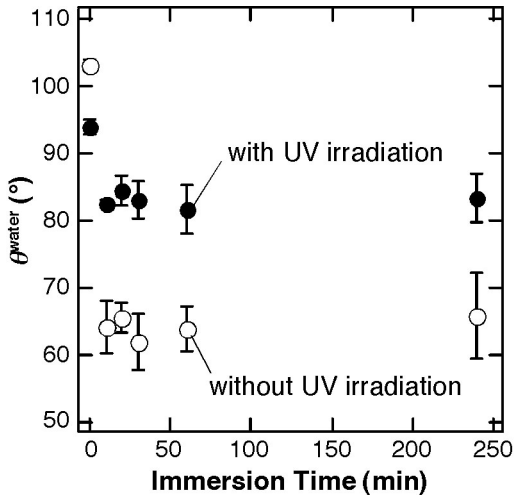

Figure 3.1 Water contact angle (θ_{water}) of SAMs of diacetylenic alkylphosphoric acid (1b) formed on GaN after soaking in 0.1M NaOH for 0, 10, 20, 30, 60 and 240 min at room temperature. Filled and open circles represent data obtained for SAMs with and without the UV irradiation (254 nm, 6 min), respectively. The plots and error bars indicate the average and standard deviation, respectively, measured using three separate samples.

3.3.3. Effect of UV Irradiation Time on the Stability of Diacetylenic Alkylphosphonate SAMs on GaN in Basic Solution

For all the diacetylenic alkylphosphonic acids examined, UV irradiation led to the reduced desorption of their SAMs on GaN in basic solution. **Figure 3.2** summarizes the effect of UV irradiation time (t_{UV}) on the water contact angle of the SAMs of **1a**–**1c** after immersion in 0.1 M NaOH for 4 hours (θ_{NaOH}^{water}). Without UV irradiation (i.e., at t_{UV} = 0 min), θ_{NaOH}^{water} was ca. 60° for all the SAMs examined, indicating that these SAMs similarly desorbed in 0.1 M NaOH. With increasing t_{UV}, θ_{NaOH}^{water} increased up to ca. 80°, indicating the reduced desorption of the SAMs due to the photopolymerization of conjugated diacetylene moieties in the SAMs. However, prolonged UV irradiation led to a slight decrease in θ_{NaOH}^{water}, which would be due to the degradation of the SAMs induced by the UV irradiation (*vide infra*).[48, 49] Interestingly, t_{UV} that gave the highest θ_{NaOH}^{water} was longer for **1a**, which has a conjugated diacetylene moiety closer to a terminal phosphonic acid group, probably reflecting the feasibility of the UV-initiated polymerization of diacetylene moieties. The photopolymerization and degradation of the SAMs could be verified from their visible absorption spectra described in the next section.

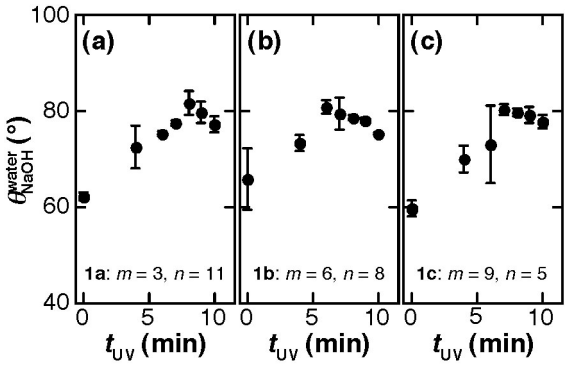

Figure 3.2 Influence of UV irradiation time (t_{UV}) on water contact angle of diacetylenic phosphonate SAMs on GaN measured after soaking in 0.1 M NaOH for 4 hours at room temperature: (θ^{water}_{NaOH}): (a) 1a; (b) 1b; (c) 1c. The plots and error bars indicate the average and standard deviation, respectively, measured using three separate samples.

3.3.4. Visible Absorption Spectra of Diacetylenic Alkylphosphonate SAMs on AlGaN

Figure 3.3 shows transmission visible absorption spectra of a SAM of **1c** on $Al_{0.25}Ga_{0.75}N$ at different t_{UV}. At t_{UV} = 0 min, except a peak around 580-600 nm due to the AlGaN epilayer,[50, 51] there was no peak originating from the diacetylenic alkylphosphonate SAM in the wavelength range of 500-700 nm. Upon UV irradiation, a broad peak around 640 nm appeared. The height of the peak increased up to 6 min, and then decreased for longer t_{UV}. The peak around 640 nm could be assigned to π-π * electronic transition in the blue form of polydiacetylene.[12, 22, 27, 34] Indeed, the maximum absorbance obtained at t_{UV} = 6 min (ca. 0.002) was similar to that of polydiacetylene monolayer reported previously.[32, 47] On the other hand, a peak around 540 nm due to the red form of polydiacetylene[12, 22, 27, 34] was not observed even for the prolonged t_{UV}, indicating that the decrease in 640-nm peak intensity for the longer t_{UV} would be due to the degradation of the polydiacetylene on AlGaN induced by UV irradiation. The UV-induced degradation of polydiacetylene was reported previously.[48, 49]

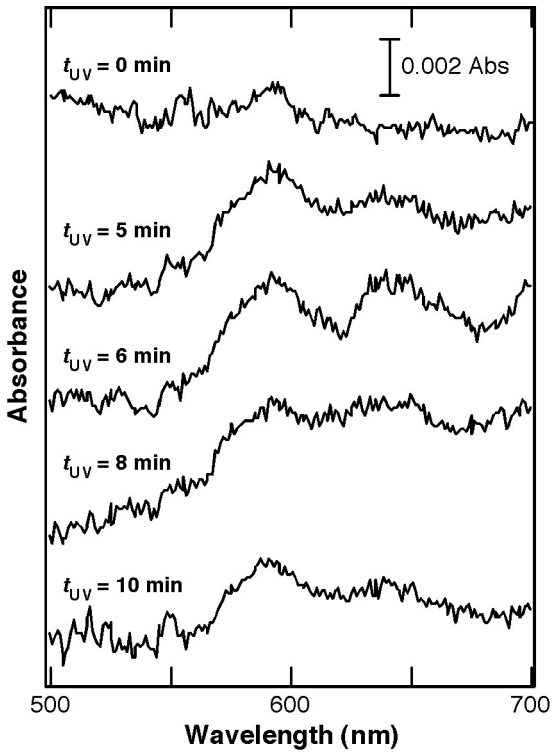

Figure 3.3 Visible absorption spectra of SAMs of 1c formed on $Al_{0.25}Ga_{0.75}N$ substrates at different UV irradiation times. A peak around 580-600 nm originated from the substrate, which could not be completely subtracted from the background visible absorption spectrum.

Similar changes in the absorbance at 640 nm upon UV irradiation were observed for SAMs of the diacetylenic alkylphosphonic acids (**1a**–**1c**), as summarized in Figure 3.4. t_{UV} that gave the maximum absorbance (i.e., the maximum polymerization) was longer in the order of **1a** > **1b** ~ **1c**. This order corresponded to that of t_{UV} required for maximum stability in basic solution (Figure 3.2), supporting the claim that the improved stability of the diacetylenic alkylphosphonate SAMs (Figure 3.1) was due to their UV-initiated polymerization. In addition, the order suggests photopolymerization was less efficient as the diacetylene moieties were closer to the substrate (i.e., **1a**), which was consistent to the trend observed in the photopolymerization yield of diacetylenic thiolate SAMs on gold.[52] The lower efficiency probably reflected the hindrance of the topochemical polymerization due to the limited flexibility of the diacetylene moieties.[53] In comparison, more efficient photopolymerization was observed in a LB film of an amphiphilic compound having the same total hydrophobic chain length with a diacetylene moiety near a hydrophilic head group.[23] In LB films, the head groups were not completely fixed

to the air/water interface, and thus the photopolymerization efficiency was mainly determined by molecular packing that was better for compounds with longer alkyl chains.[23]

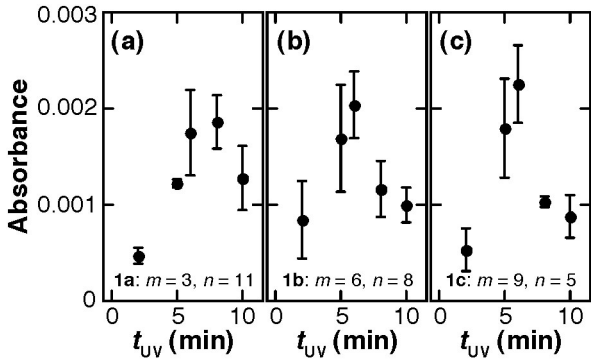

Figure 3.4 Relationship between the absorbance of diacetylenic phosphonate SAMs formed on $Al_{0.25}Ga_{0.75}N$ at 645 nm and UV irradiation time(t_{UV}): (a) 1a; (b) 1b; (c) 1c. The peak height was determined by Gaussian fitting of a peak. The plots and error bars indicate the average and standard deviation, respectively, measured using three separate samples.

3.3.5. AFM Images of a Photopolymerized Diacetylenic Alkylphosphonate SAM on GaN before and after Immersion in Basic Solution

In addition, AFM images of a photopolymerized diacetylenic SAM on GaN were measured to understand its partial desorption in 0.1 M NaOH (Figure 3.1, filled circles). Figure 5 shows topographic and friction images of a UV-irradiated SAM of 1b on GaN before and after immersion in 0.1 M NaOH for 4 hours. The topographic images prior to the immersion (Figure 3.5a, left) showed step features that reflected the underlying surface structure of a GaN substrate fabricated by the MOCVD method,[9, 17] suggesting uniform coverage of the surface with the SAM. In contrast, after immersed in 0.1 M NaOH, a number of pits were observed in the topographic image, especially at the step edges (Figure 3.5b, left). The surface heterogeneity was more clearly shown in the frictional images (i.e., the right images of Figures 3.5a and b). The pits were probably formed as a result of the desorption of the SAM molecules that were not highly crosslinked at their defects. The preferential desorption at the step edges may reflect the hindered topochemical photopolymerization of diacetylene moieties at the step edges of the substrate[53] and also the higher accessibility of the basic solution to the resulting defect sites in the SAM.

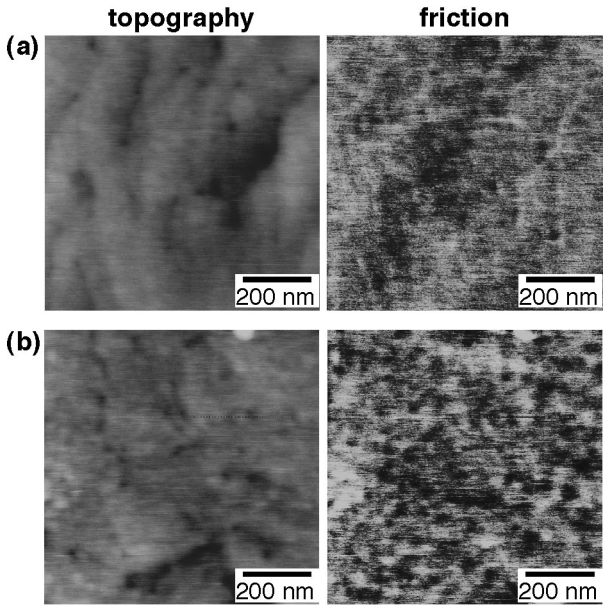

Figure 3.5 Contact mode topography (left) and friction (right) images of a UV-irradiated (6 min) SAM of diacetylenic phosphoric acid 1b on GaN. (a) before and (b) after soaking in 0.1 M NaOH for 4 hours at room temperature. The topography and friction images were taken at the same area simultaneously.

3.4. Conclusions

This chapter described the SAM formation of diacetylenic alkylphosphonate SAMs on group-III nitride substrates and their photopolymerization. UV/O_3-treated AlGaN substrates could be used to prepare alkylphosphonate SAMs, as with UV/O_3-treated GaN substrates. They exhibited weaker adsorption of the other primary substituted hydrocarbons as compared to GaN maybe due to the presence of Al_2O_3 having lower hydrogen bond acidity. More importantly, the UV-initiated photopolymerization of diacetylenic alkylphosphonate SAMs reduced their desorption in aqueous basic solution. SAMs containing diacetylene moieties farther from terminal phosphonate groups exhibited more efficient photopolymerization. However, the hindrance of the topochemical polymerization at the III-N surface step edges and the UV-induced degradation of polydiacetylene on group-III nitride surface limited the uniform functionalization with diacetylenic alkylphosphonate SAMs.

References

1. Steinhoff, G.; Purrucker, O.; Tanaka, M.; Stutzmann, M.; Eickhoff, M. *Adv. Funct. Mater.* **2003**, *13*, 841-846.
2. Chaniotakis, N.; Sofikiti, N. *Anal. Chim. Acta* **2008**, *615*, 1-9.
3. Pearton, S. J.; Ren, F.; Wang, Y. L.; Chu, B. H.; Chen, K. H.; Chang, C. Y.; Lim, W.; Lin, J. S.; Norton, D. P. *Prog. Mater. Sci.* **2009**, *55*, 1-59.
4. Steinhoff, G.; Hermann, M.; Schaff, W. J.; Eastman, L. F.; Stutzmann, M.; Eickhoff, M. *Appl. Phys. Lett.* **2003**, *83*, 177-179.
5. Alifragis, Y.; Konstantinidis, G.; Georgakilas, A.; Chaniotakis, N. *Electroanalysis* **2005**, *17*, 527-531.
6. Dimitrova, R.; Catalan, L.; Alexandrov, D.; Chen, A. *Electroanalysis* **2007**, *19*, 1799-1806.
7. Tran Ba, K. H.; Mastro, M. A.; Hite, J. K.; Eddy, C. R. J.; Ito, T. *Appl. Phys. Lett.* **2009**, *95*, 142501.
8. Kang, B. S.; Ren, F.; Wang, L.; Lofton, C.; Tan, W. W.; Pearton, S. J.; Dabiran, A.; Osinsky, A.; Chow, P. P. *Appl. Phys. Lett.* **2005**, *87*, 023508.
9. Baur, B.; Steinhoff, G.; Hernando, J.; Purrucker, O.; Tanaka, M.; Nickel, B.; Stutzmann, M.; Eickhoff, M. *Appl. Phys. Lett.* **2005**, *87*, 263901.
10. Petoral, R. M., Jr.; Yazdi, G. R.; Lloyd Spetz, A.; Yakimova, R.; Uvdal, K. *Appl. Phys. Lett.* **2007**, *90*, 223904.
11. Yakimova, R.; Steinhoff, G.; Petoral, R. M., Jr.; Vahlberg, C.; Khranovskyy, V.; Yazdi, G. R.; Uvdal, K.; Lloyd Spetz, A. *Biosens. Bioelectron.* **2007**, *22*, 2780-2785.
12. Ulman, A. *An Introduction to Ultrathin Organic Films: from Langmuir–Blodgett to Self-Assembly*; Academic Press: London, 1991.
13. Ulman, A. *Chem. Rev.* **1996**, *96*, 1533-1554.
14. Love, J. C.; Estroff, L. A.; Kriebel, J. K.; Nuzzo, R. G.; Whitesides, G. M. *Chem. Rev.* **2005**, *105*, 1103-1169.
15. Wang, H.-T.; Kang, B. S.; Chancellor, T. F., Jr.; Lele, T. P.; Ren, F.; Pearton, S. J.; Johnson, W. J.; Rajagopal, P.; Roberts, J. C.; Piner, E. L.; Linthicum, K. J. *Appl. Phys. Lett.* **2007**, *91*, 042114.
16. Kang, B. S.; Wang, H.-T.; Ren, F.; Pearton, S. J. *J. Appl. Phys.* **2008**, *104*, 031101.

17. Ito, T.; Forman, S. M.; Cao, C.; Eddy, C. R. J.; Mastro, M. A.; Holm, R. T.; Henry, R. L.; Hohn, K.; Edgar, J. H. *ECS Transaction* **2007**, *11*, 97-101.
18. Ito, T.; Forman, S. M.; Cao, C.; Li, F.; Eddy, C. R., Jr.; Mastro, M. A.; Holm, R. T.; Henry, R. L.; Hohn, K.; Edgar, J. H. *Langmuir* **2008**, *24*, 6630-6635.
19. Kim, H.; Colavita, P. E.; Paoprasert, P.; Gopalan, P.; Kuech, T. F.; Hamers, R. J. *Surf. Sci.* **2008**, *602*, 2382-2388.
20. Hughes, W. C.; Koh, S. E.; Augustine, B. H.; Polefrone, J. M. *Proceedings - Electrochemical Society* **2001**, *2001-1*, 213-217.
21. Mueller, A.; O'Brien, D. F. *Chem. Rev.* **2002**, *102*, 727-757.
22. Reppy, M. A.; Pindzola, B. A. *Chem. Commun.* **2007**, *42*, 4317-4338.
23. Tieke, B.; Lieser, G. *J. Colloid Interface Sci.* **1982**, *88*, 471-486.
24. Ostermayer, B.; Vogt, W. *Makromol. Chem., Rapid Commun.* **1982**, *3*, 563-568.
25. Albrecht, O.; Laschewsky, A.; Ringsdorf, H. *J. Memb. Sci.* **1985**, *22*, 187-197.
26. Ostermayer, B.; Albrecht, O.; Vogt, W. *Chem. Phys. Lipids* **1986**, *41*, 265-291.
27. Carpick, R. W.; Sasaki, D. Y.; Marcus, M. S.; Eriksson, M. A.; Burns, A. R. *J. Phys.: Condens. Matter* **2004**, *16*, R679-R697.
28. Batchelder, D. N.; Evans, S. D.; Freeman, T. L.; Haussling, L.; Ringsdorf, H.; Wolf, H. *J. Am. Chem. Soc.* **1994**, *116*, 1050-1053.
29. Kim, T.; Chan, K. C.; Crooks, R. M. *J. Am. Chem. Soc.* **1997**, *119*, 189-193.
30. Chan, K. C.; Kim, T.; Schoer, J. K.; Crooks, R. M. *J. Am. Chem. Soc.* **1995**, *117*, 5875-5876.
31. Kim, T.; Crooks, R. M.; Tsen, M.; Sun, L. *J. Am. Chem. Soc.* **1995**, *117*, 3963-3967.
32. Gatebe, E.; Herron, H.; Zakeri, R.; Rajasekaran, P. R.; Aouadi, S.; Kohli, P. *Langmuir* **2008**, *24*, 11947-11954.
33. Okada, S.; Peng, S.; Spevak, W.; Charych, D. *Acc. Chem. Res.* **1998**, *31*, 229-239.
34. Yoon, B.; Lee, S.; Kim, J.-M. *Chem. Soc. Rev.* **2009**, *38*, 1958-1968.
35. Eddy, C. R., Jr. ; Holm, R. T.; Henry, R. L.; Culbertson, J. C.; Twigg, M. E. *J. Electron. Mater.* **2005**, *34*, 1187-1192.
36. Kosolapoff, G. M. *J. Am. Chem. Soc.* **1944**, *66*, 1511-1512.
37. Xu, Z.; Byun, H.-S.; Bittman, R. *J. Org. Chem.* **1991**, *56*, 7183-7186.
38. Kim, T.; Crooks, R. M. *Tetrahedron Lett.* **1994**, *35*, 9501-9504.

39. Zamorano-Octaviano, J.; Hernandez-Martínez, A.; Ortega-Guevara, A.; Linzaga-Elizalde, I.; Höpfl, H. *Heteroat. Chem.* **2006**, *17*, 75-80.
40. Hashizume, T.; Nakasaki, R.; Ootomo, S.; Oyama, S.; Hasegawa, H. *Mater. Sci. Eng. B* **2001**, *80*, 309-312.
41. Wolter, S. D.; Luther, B. P.; Waltemyer, D. L.; Onneby, C.; Mohney, S. E.; Molnar, R. J. *Appl. Phys. Lett.* **1997**, *70*, 2156-2158.
42. Shalish, I.; Shapira, Y.; Burstein, L.; Salzman, J. *J. Appl. Phys.* **2001**, *89*, 390-395.
43. Shiozaki, N.; Sato, T.; Hashizume, T. *Jpn. J. Appl. Phys.* **2007**, *46*, 1471-1473.
44. Vimont, A.; Lavalley, J. C.; Sahibed-Dine, A.; Otero Arean, C.; Rodriguez Delgado, M.; Daturi, M. *J. Phys. Chem. B* **2005**, *109*, 9656-9664.
45. Auroux, A.; Gervasini, A. *J. Phys. Chem.* **1990**, *94*, 6371-6379.
46. Liakos, I. L.; Newman, R. C.; McAlpine, E.; Alexander, M. R. *Langmuir* **2007**, *23*, 995-999.
47. Tanaka, T.; Honda, Y.; Sugi, M. *Jpn. J. Appl. Phys.* **1995**, *34*, 3250-3254.
48. Bloor, D.; Worboys, M. R. *J. Mater. Chem.* **1998**, *8*, 903-912.
49. Morigaki, K.; Schonherr, H.; Frank, C. W.; Knoll, W. *Langmuir* **2003**, *19*, 6994-7002.
50. Rieger, W.; Dimitrov, R.; Brunner, D.; Rohrer, E.; Ambacher, O.; Stutzmann, M. *Phys. Rev. B* **1996**, *54*, 17596-17602.
51. Mattila, T.; Nieminen, R. M. *Phys. Rev. B* **1997**, *55*, 9571-9576.
52. Menzel, H.; Mowery, M. D.; Cai, M.; Evans, C. E. *J. Phys. Chem. B* **1998**, *102*, 9550-9556.
53. Mowery, M. D.; Menzel, H.; Cai, M.; Evans, C. E. *Langmuir* **1998**, *14*, 5594-5602.

Chapter 4 - Quantitative Investigation of Surface Functionalization of Cylindrical Nanopores Derived from Polystyrene-Poly(methylmethacrylate) Diblock Copolymers

Reproduced by permission of The Royal Society of Chemistry
Published as: Li, F., Diaz, R., Ito, T. *RSC Advances*, **2011**, *1*, 1732–1736

4.1. Introduction

Nanoporous films derived from cylinder-forming block copolymers[1-3] are promising materials for chemical and biological separations because of their high porosities, cylindrical pore shapes, and uniform and controllable pore diameters.[4, 5] Previous work has mainly focused on investigating their size-selective molecular permeability: Such nanoporous films were applied for virus filtration,[6, 7] macromolecule separations[8, 9] and protein delivery.[10]

Film permeability can be tailored based on chemical interactions by functionalizing the nanopore surface, as demonstrated with track-etched and anodic alumina membranes.[11] However, the surface chemistry of block copolymer-derived nanoporous films has attracted limited attention. Novel block copolymers were synthesized to fabricate nanoporous films comprising cylindrical nanopores with predictable surface functional groups upon chemical degradation of the cylindrical domains.[12-16] Chemical modification of the resulting nanopore surface was assessed using NMR and FTIR.[12-14] Very recently, a polystyrene-poly(methylmethacrylate) block copolymer (PS-*b*-PMMA) with a di-COOH group at the PMMA terminal was synthesized to fabricate thin films comprising COOH-decorated nanopores.[17] Nanoporous films were obtained by dissolving PMMA homopolymer from block copolymer-homopolymer blend films. The surface -COOH groups were employed to covalently immobilize single-stranded probe DNA.

We have investigated the surface chemistry of cylindrical nanopores derived from PS-*b*-PMMA.[18-21] Nanoporous films were prepared by selective removal of the cylindrical PMMA domains in thermally-annealed thin films via UV-based degradation and subsequent acetic acid (AcOH) treatment.[22, 23] Electrochemical methods were employed to assess the pH-dependence

of film permeability for charged redox species, revealing the presence of surface -COOH groups.[18] The presence of surface -COOH groups was further validated by scanning force microscopy studies on UV/AcOH-treated PS-*b*-PMMA films.[21, 24] Electrochemical methods were also used to verify nanopore surface functionalization via aqueous-phase amidation of the surface –COOH groups mediated by 1-ethyl-3-(3-dimethylaminopropyl)carbodiimide chloride (EDC).[19, 20] However, the electrochemical and force microscopy approaches measure changes in film permeability and tip-surface force primarily based on electrostatic interactions.[18, 20, 21] Because of surface charge screening involved in electrostatic effects, it is challenging to directly and quantitatively correlate electrochemical and surface force data to the density of surface -COOH groups.[25] PS-*b*-PMMA-derived nanoporous films cannot be characterized using solution-phase NMR as was done previously,[12-14] because they are insoluble in organic solvent as a result of the UV-induced crosslinking of the PS matrix.[7, 26] The surface functionalization of these films cannot be assessed using FTIR spectroscopy, because the absorption bands of surface –COOH groups were not observed in the FTIR spectra of these films.[18]

Here, the surface functionalization efficiency of PS-*b*-PMMA-derived nanopores was quantitatively assessed by measuring monovalent probe cations released from the surface –COOH groups via cation-exchange processes. The nanopore surface was functionalized by aqueous-phase amidation mediated by EDC and organic-phase amidation/esterification through acid chloride. These reactions reduce free –COOH groups on nanopore surface, and thus their yields can be determined by comparing the surface –COOH densities before and after the reactions. The quantity of cations released from a 30-nm thick film was on the order of pmol, and thus was measured using highly-sensitive analytical techniques including spectrofluorometry and inductively coupled plasma mass spectrometry (ICP-MS). Similar approaches using spectrofluorometry have been employed previously to determine the modification yields of surface -COOH groups in track-etched membranes.[27, 28]

4.2. Experimental Section

4.2.1. Chemicals and Materials

Three types of PS-*b*-PMMA (43K PS-*b*-PMMA: M_n = 31 400 g/mol for PS and 11 500 g/mol for PMMA, M_w/M_n = 1.06; 57K PS-*b*-PMMA: M_n = 39 800 g/mol for PS and 17 000 g/mol for PMMA, M_w/M_n = 1.06; 82K PS-*b*-PMMA: M_n = 57 000 g/mol for PS and 25 000

g/mol for PMMA, M_w/M_n = 1.07) were purchased from Polymer Source and used as received. Ferrocene (Aldrich), aluminum chloride ($AlCl_3$, Acros), 16-bromohexadecanoic acid (Aldrich), 6-bromohexanoic acid (Aldrich), ferrocene carboxaldehyde (Aldrich), hydroxylamine (Aldrich), magnesium sulfate (Fisher), lithium aluminum hydride ($LiAlH_4$, Aldrich), ethanol (Fisher) and potassium acetate (Aldrich) were used as received. Tetrahydrofuran (THF, Fisher) was dried by distillation from Na, and dichloromethane (Fisher) was dried by distillation from CaH_2. Rhodamine 6G (Aldrich), cesium chloride (Aldrich), thionine acetate (Acros), 1-ethyl-3-(3-dimethylaminopropyl)carbodiimide hydrochloride (EDC; Chemimpex international), *N*-hydroxysuccinimide (Acros Organics), tetraethyleneglycol monoamine ($(PEO)_4NH_2$; Molecular Biosciences, Inc.), oxalyl chloride (Acros) and glacial acetic acid (AcOH) were used as received. Gold-coated Si wafers, which were prepared by sputtering 10 nm of Ti followed by 20 nm of Au onto Si (100) wafers, were purchased from LGA Thin Films (Foster City, CA). All aqueous solutions were prepared with water having a resistivity of 18 MΩ cm or higher (Barnstead Nanopure Systems).

4.2.2. Synthesis of Ferrocene Derivatives

^{1}H- and ^{13}C-NMR spectra were measured on a Varian INOVA 400 Fourier transform NMR spectrometer, and chemical shifts were reported in δ values in ppm downfield of tetramethylsilane. IR spectra were measured on a Nicolet Protege 640 spectrophotometer. Exact MS data were measured at the Mass Spectroscopy Laboratory, University of Kansas.

4.2.2.1. Synthesis of Ferrocenylmethylamine

Ferrocenylmethylamine was synthesized according to reported procedure.[32] A mixture of ferrocene carboxaldehyde (0.50 g, 2.34 mmol) and hydroxylamine (0.165 g, 5.00 mmol) in ethanol (25 mL) was stirred at reflux for 3 h. After cooling to room temperature, the mixture was poured to 50 mL water, and then extracted by dichloromethane (3 × 30 mL). The organic phase was washed by brine, and then dried over $MgSO_4$. The solvent was evaporated to give ferrocenylcarboxaldehyde oxime as an orange solid. The solid was dried, and then dissolved in anhydrous THF (20 mL) without purification. This solution was dropped to $LiAlH_4$ (0.37 g, 9.30 mmol) in anhydrous THF (20 mL). The mixture was stirred under reflux overnight. After cooling to room temperature, the mixture was poured to 30 mL water, and then extracted by diethyl ether (3 × 100 mL). The organic phase was washed by brine, and then dried over

$MgSO_4$. The solvent was removed, and purified by silica gel column chromatography (elution with ethyl acetate) to give ferrocenylmethylamine as an orange oil (0.44 g, 89%). ^{1}H-NMR ($CDCl_3$) δ 4.16 (t, J = 2.0 Hz, 2H, C_p), 4.14 (s, 5H, $C_{p'}$), 4.11 (t, J = 2.0 Hz, 2H, C_p), 3.53 (s, J = 6.2 Hz, 2H, CH_2).

4.2.2.2. Synthesis of 16-Bromo-1-Oxohexadecylferrocene

16-Bromo-1-oxohexadecylferrocene was synthesized following the same procedure reported for 6-bromo-1-oxohexylferrocene.[33] 16-Bromohexadecanoic acid (0.50 g, 1.49 mmol) and oxalyl chloride (3 mL, 35 mmol) were mixed together and stirred at room temperature for overnight. The extra oxalyl chloride was removed under vacuum to obtain a colorless solid. Anhydrous dichloromethane (5 mL) was added to the flask to dissolve the solid, and then anhydrous $AlCl_3$ (0.2 g, 1.5 mmol) was added to the solution and stirred for 20 min at 0 °C under argon. In a separate flask, ferrocene (0.28 g, 1.5 mmol) was dissolved in 5 mL of anhydrous dichloromethane. The acid-chloride-containing solution was transferred to the ferrocene-containing solution via cannula over a period of 5 min. The solution turned purple during this addition. After stirring for 2 h, 5 mL of water was added slowly. After additional stirring for 10 min, the solution was diluted with 25 mL dichloromethane. The organic layer was collected, washed with water until the pH of the aqueous phase became neutral, and dried over $MgSO_4$. The solvent was removed, and then purified by silica gel column chromatography (eluent: dichloromethane) to give 16-bromo-1-oxohexadecylferrocene as an orange solid (0.65 g, 87%). ^{1}H-NMR ($CDCl_3$) δ 4.79 (t, J = 1.6 Hz, 2H, C_p), 4.50 (t, J = 1.6 Hz, 2H, C_p), 4.21 (s, 5H, $C_{p'}$), 3.42 (t, J = 6.8 Hz, 2H, CH_2Br), 2.70 (t, J = 7.4 Hz, 2H, $COCH_2$), 1.88 (m, 2H, CH_2), 1.71 (m, 2H, CH_2), 1.56-1.27 (m, 22H, $(CH_2)_{11}$). ^{13}C-NMR ($CDCl_3$) δ 205.06, 79.36, 72.31, 69.93, 69.53, 39.98, 34.37, 33.03, 29.85, 29.82, 29.74, 29.65, 28.98, 28.38, 24.86.

4.2.2.3. Synthesis of 6-Bromo-1-Oxohexylferrocene

6-Bromo-1-oxohexylferrocene as an orange oil was prepared from bromohexadecanoic acid by following the same procedure as 16-bromo-1-oxohexadecylferrocene (yield: 79%). ^{1}H-NMR ($CDCl_3$) δ 4.79 (t, J = 2.0 Hz, 2H, C_p), 4.50 (t, J = 2.0 Hz, 2H, C_p), 4.20 (s, 5H, $C_{p'}$), 3.43 (t, J = 6.8 Hz, 2H, CH_2Br), 2.75 (t, J = 7.2 Hz, 2H, $COCH_2$), 1.97 (m, 2H, CH_2), 1.75 (m, 2H, CH_2), 1.58 (m, 2H, CH_2).

4.2.2.4. Synthesis of 16-Acetyl-1-Oxohexadecylferrocene

16-Bromo-1-oxohexadecylferrocene (0.45 g, 0.89 mmol) was dissolved in 6 mL of ethanol, followed by addition of potassium acetate (3.51 g, 35 mmol) to the solution. The mixture was refluxed for 48 hours with stirring. The solvent was removed, and then purified by silica gel column chromatography (eluent: dichloromethane) to give 16-acetyl-1-oxohexadecylferrocene as an orange solid (0.31 g, 71%). ^{1}H-NMR ($CDCl_3$) δ 4.78 (t, J = 2.0 Hz, 2H, C_p), 4.49 (t, J = 1.8 Hz, 2H, C_p), 4.20 (s, 5H, $C_{p'}$), 4.05 (t, J = 7.0 Hz, 2H, CH_2O), 2.69 (t, J = 7.6 Hz, 2H, $COCH_2$), 2.05 (s, 3H, CH_3), 1.71 (m, 2H, CH_2), 1.62 (m, 2H, CH_2), 1.35-1.27 (m, 22H, $(CH_2)_{11}$). ^{13}C-NMR ($CDCl_3$) δ ($CDCl_3$) δ 204.92, 171.46, 79.44, 72.28, 69.94, 69.55, 64.89, 39.99, 29.86, 29.78, 29.76, 29.47, 28.82, 26.13, 24.87, 21.24.

4.2.2.5. Synthesis of 6-Acetyl-1-Oxohexylferrocene

6-Acetyl-1-oxohexylferrocene as an orange oil was prepared from 6-bromo-1-oxohexylferrocene by following the same procedure as 16-acetyl-1-oxohexadecylferrocene (yield: 75%). ^{1}H-NMR ($CDCl_3$) δ 4.79 (t, J = 2.0 Hz, 2H, C_p), 4.51 (t, J = 1.6 Hz, 2H, C_p), 4.20 (s, 5H, $C_{p'}$), 4.09 (t, J = 6.8 Hz, 2H, CH_2O), 2.72 (t, J = 7.2 Hz, 2H, $COCH_2$), 2.06 (s, 3H, CH_3), 1.75-1.46 (m, 6H, $(CH_2)_3$). ^{13}C-NMR ($CDCl_3$) δ 204.45, 171.44, 79.31, 72.38, 69.97, 69.53, 64.64, 39.70, 28.81, 26.14, 24.37, 21.25.

4.2.2.6. Synthesis of 16-Hydroxy-1-Oxohexadecylferrocene

16-Acetyl-1-oxohexadecylferrocene (0.30 g, 0.62 mmol) was mixed with sodium hydroxide solution (3 M, 15 mL), then refluxed for 48 h. The mixture was extracted by ethyl acetate (3 × 30 mL). The organic phase was washed by brine, and then dried over $MgSO_4$. The solvent was removed, and then purified by silica gel column chromatography (eluent: dichloromethane: ethyl acetate = 7:3) to give 16-hydroxy-1-oxohexadecylferrocene as an orange solid (0.26 g, 98%). ^{1}H-NMR ($CDCl_3$) δ 4.79 (t, J = 2.0 Hz, 2H, C_p), 4.49 (t, J = 1.8 Hz, 2H, C_p), 4.20 (s, 5H, $C_{p'}$), 3.65 (t, J = 6.4 Hz, 2H, CH_2OH), 2.70 (t, J = 7.4 Hz, 2H, $COCH_2$), 1.71 (m, 2H, CH_2), 1.57 (m, 2H, CH_2), 1.35-1.27 (m, 22H, $(CH_2)_{11}$). ^{13}C-NMR ($CDCl_3$) δ 205.02, 79.45, 72.31, 69.96, 69.78, 69.58, 63.34, 40.02, 33.05, 30.20, 29.86, 29.82, 29.81, 29.76, 29.65, 25.97, 24.90. FTIR (cm^{-1}): 3097, 2920, 2850, 1661, 1473, 1461, 1105, 836, 823, 719. Exact MS: m/z calculated for $C_{26}H_{41}O_2Fe$ (M + Na), 463.2290; found, 463.2275.

4.2.2.7. Synthesis of 6-Hydroxy-1-Oxohexylferrocene

6-Hydroxy-1-oxohexylferrocene as an orange oil was prepared from 6-acetyl-1-oxohexylferrocene by following the same procedure as 16-hydroxy-1-oxohexadecylferrocene (yield: 99%). ^{1}H-NMR ($CDCl_3$) δ 4.79 (t, J = 1.8 Hz, 2H, C_p), 4.50 (t, J = 1.6 Hz, 2H, C_p), 4.20 (s, 5H, $C_{p'}$), 3.70 (t, J = 6.4 Hz, 2H, CH_2O), 2.74 (t, J = 7.4 Hz, 2H, OCH_2), 1.75 (m, 2H, CH_2) , 1.65 (m, 2H, CH_2) , 1.47 (m, 2H, CH_2). ^{13}C-NMR ($CDCl_3$) δ 204.79, 79.32, 72.40, 69.99, 69.55, 62.93, 45.03, 39.79, 32.74, 25.83, 24.32. FTIR (cm^{-1}): 3343, 3095, 2917, 2848, 1661, 1470, 1462, 1377, 1105, 820, 718. Exact MS: m/z calculated for $C_{16}H_{20}O_2Fe$ (M + Na), 323.0715; found, 323.0710.

4.2.3. Preparation of PS-b-PMMA-Derived Nanoporous Films

PS-*b*-PMMA-derived nanoporous films on gold electrodes were prepared according to procedures reported previously.[18, 19, 23] Gold-coated Si wafers were sonicated in ultra pure water and ethanol for 30 min, and then cleaned in a Novascan PSD-UVT UV-ozone system for 60 min prior to use. Thin films of PS-*b*-PMMA were prepared on cleaned gold substrates by spin-coating (2000 rpm) from its toluene solution (0.6% (w/w)) and annealed at 170 °C in vacuum (ca. 0.3 Torr) for 60 h. According to AFM images, annealed PS-*b*-PMMA films with thickness of 20-35 nm comprised cylindrical PMMA domains oriented perpendicularly to the film surface. The PMMA domains were removed by irradiation with UV light using a Novascan PSDUVT UV-ozone system (ca. 20 mW/cm^2) under an Ar atmosphere and by subsequent immersing in AcOH. The thickness of annealed PS-*b*-PMMA films prior to the UV irradiation was measured using a J. A. Woollam alpha-SE spectroscopic ellipsometer. In addition, those before and after UV/acetic acid treatment were measured with a surface profiler (XP-2, Ambios Technology).

4.2.4. Surface Functionalization of PS-b-PMMA-Derived Nanopores

4.2.4.1. Aqueous-Phase Amidation

Aqueous-phase amidation mediated by EDC was performed according to previous procedure.[19, 20] PS-*b*-PMMA-derived nanoporous films on gold were immersed in aqueous solution containing EDC (0.2 g/mL) and *N*-hydroxysuccinimide (0.03 g/mL) in phosphate buffer (0.1 M, pH 6) for 7 h with gentle shaking. The films were then soaked in an aqueous phosphate

buffer (pH 6) containing an amine reactant (10 mM) for 24 h with gentle shaking. The samples were rinsed with phosphate buffer and then with water.

4.2.4.2. Organic-Phase Amidation and Esterification

PS-*b*-PMMA-derived nanoporous films on gold were immersed in oxalyl chloride, and heated at 50 ºC overnight. After excess oxalyl chloride was removed under vacuum, the films were soaked in a dichloromethane solution of amine or alcohol reactant (2 mM) at room temperature for 2 h. The samples were washed with dichloromethane and dried.

4.2.5. AFM Measurements

AFM images were obtained by contact mode imaging in air, using a Picoscan SPM (Molecular Imaging). Contact mode tips from Vista Probes (CS-25) were employed. These tips were first rinsed with ethanol and then cleaned in a Novascan PSD-UVT UV-ozone system for 20 min prior to use.

4.2.6. Determination of Free Surface –COOH Density via Cation Exchange

A freshly-prepared nanoporous film was immobilized at the bottom of a cell similar to those employed for electrochemical measurements.[18, 20] The area of a film in contact with the solution was defined by an O-ring (0.80 cm in diameter). The film was immersed in an aqueous solution of a probe (Rhodamine 6G or CsCl; 1 mM) overnight. The cell was thoroughly washed with ultrapure water, disassembled, and then further washed with ultrapure water to remove physisorbed probe cations. Then, the sample was immersed in 0.01 M HCl solution (2.00 mL) for 2 h. The amount of the released probe molecules in the HCl solution was measured with spectrofluorometry (for Rhodamine 6G) or ICP-MS (for Cs^+). For measurements with thionine acetate, the cell was soaked in an ethanol solution of thionine acetate (10 mM) overnight, thoroughly washed with ethanol, and then immersed in 0.01 M HCl (in a 1:1 mixture of ethanol and water).[26-27]

For spectrofluorometry, emission spectra at 525 nm (Rhodamine 6G) or 594 nm (thionine) as excitation wavelength were measured with an ISA-SPEX FluoroMax-2 spectrofluorometer. Fluorescence intensity at 550 nm (Rhodamine 6G) or 620 nm (thionine) was measured to determine the concentration of fluorescent probe cations released to the HCl solution (The fluorescence spectra of Rhodamine 6G and thionine are given in Figure 4.1).

Standard probe solutions (1 nM, 5 nM, 10 nM, 50 nM and 100 nM) were prepared to obtain a calibration curve for each day's measurements.

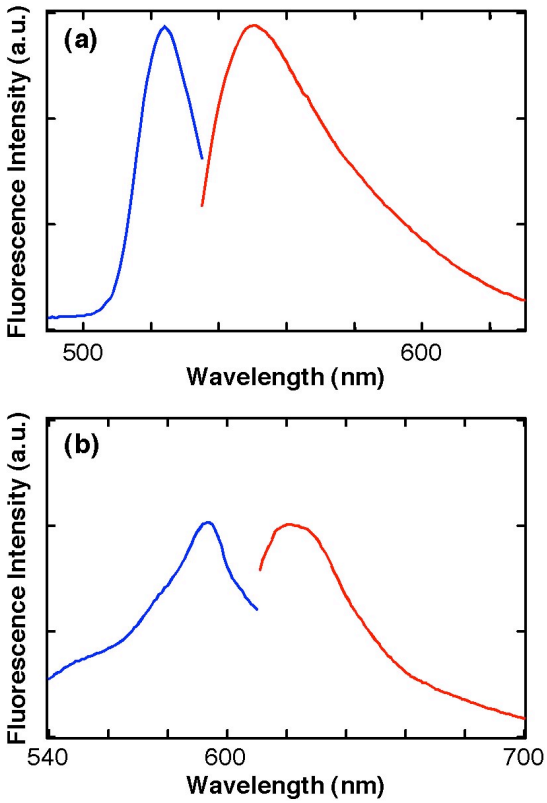

Figure 4.1 Excitation (blue) and emission (red) spectra of (a) Rhodamine 6G (0.01 mM, in 0.01 M HCl) and (b) thionine acetate (0.01 mM, in 0.01 M HCl in a 1:1 mixture of ethanol and water). The excitation spectra were measured at 550 nm (Rhodamine 6G) or 620 nm(thionine) as emission wavelength, and the emission spectra were obtained at 525 nm (Rhodamine 6G) or 594 nm (thionine) as excitation wavelength.

For ICP-MS, Cs^+ was employed because the influence of contamination was negligible. ICP-MS measurements were performed by Dr. Javier Seravall (Redox Biology Center, Department of Biochemistry, University of Nebraska-Lincoln). A calibration curve was prepared by mixing 14 µM CsCl (0.0, 1.0, 2.0, 3.0 or 4.0 µL) with 200 µL of solution containing 10 mM HCl, 0.1% HNO_3 and 50 ppb Ga^{3+} (as an internal standard). A Cs^+ signal intensity measured at m/z = 133 was normalized against the Ga signal for each sample solution. The detection limit was 0.11 nM, which was significantly higher than the Cs concentration measured in the sample solutions (20-65 nM).

4.3. Results and Discussion

The effective density of free -COOH groups on a nanoporous film was measured with ion-exchange processes as follows (Figure 4.2): A nanoporous film was immersed in an aqueous solution of neutral pH or in an ethanol solution containing a base (acetate ion)[29] to replace the proton of surface –COOH groups with monovalent probe cations (Q^+ in Figure 4.2). Subsequently, the probe-loaded film was soaked in a 0.01 M HCl solution (2.00 mL) to release the probe cations from the films. The amount of the released probes was determined from the probe concentration measured with spectrofluorometry or ICP-MS.

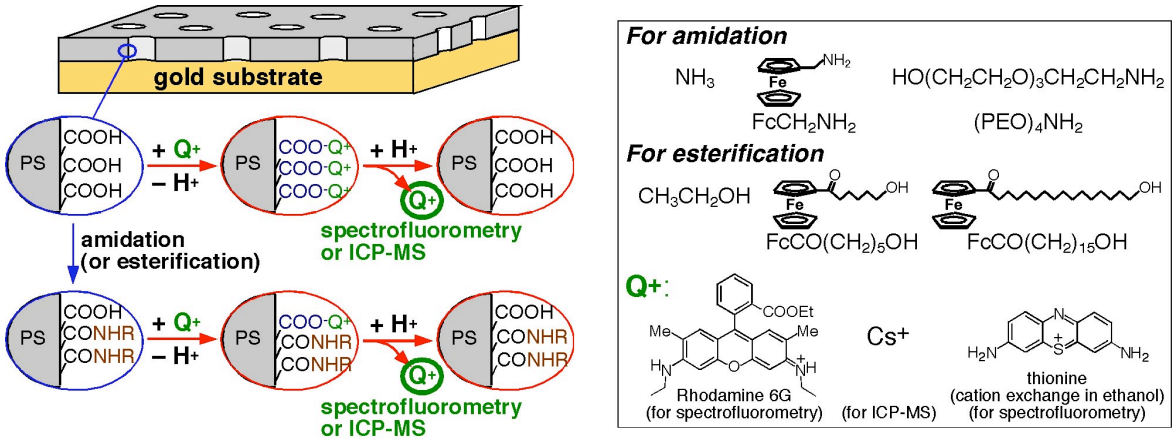

Figure 4.2 Experimental procedures for amidation/esterification of surface –COOH groups and measurements of surface free –COOH groups with monovalent probe cations (Q^+) via cation exchange processes. Amine and alcohol reactants employed for nanopore surface modification were also shown.

The -COOH density was calculated from the amount of probe cations released to 0.01 M HCl using the following equation:

$$(\text{-COOH density}) = \frac{(\text{the amount of probe cations released to 0.01 M HCl})}{\pi dLN} \quad \text{Eq 4.1}$$

In this equation, d is pore diameter obtained from AFM images (Figure 4.3), and L is pore length that corresponds to the thickness of the annealed PS-*b*-PMMA film. N is the total number of pores calculated from pore density obtained from AFM images (Figure 4.3) and film area in contact with solution defined by an O-ring (0.8 cm in diameter).

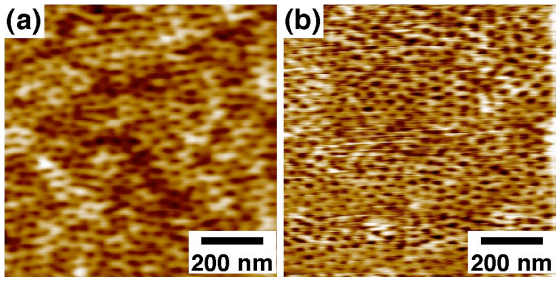

Figure 4.3 AFM images of a 57K PS-b-PMMA-derived nanoporous film (31 nm thick) on a gold substrate (a) before and (b) after organic-phase esterification with $FcCO(CH_2)_{15}OH$. Δz = 6.4 nm.

In this study, the ellipsometric thickness of an annealed film was used as *L*, the thickness of the nanoporous film obtained upon UV/AcOH treatment, because a change in film thickness was negligible for 20-35-nm thick films (Figure 4.4): Profilometry data did not exhibit detectable changes in film thickness between UV-exposed and unexposed areas in a film (Figure 4.4, top right). In addition, the thickness of a UV/AcOH-treated film, which was measured by dissolving the UV-unexposed region of the film with toluene, was almost the same as the ellipsometric thickness of the same film prior to the UV/AcOH treatment (Figure 4.4, bottom right). The ratio of these thicknesses, *i.e.,* the quotient of the profilometric thickness of a UV/AcOH-treated film divided by the ellipsometric thickness of the untreated film, measured on multiple different films was 0.99 ± 0.07.

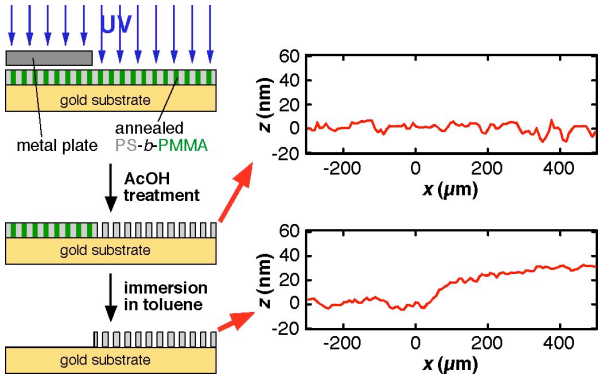

Figure 4.4 Sample preparation procedure for profilometry measurements to verify the changes in film thickness between UV-exposed and unexposed areas in a film (top right) and to determine the thickness of a UV/AcOH- treated film (bottom right). The ellipsometric thickness of the film prior to UV/AcOH treatment was 31 nm. In the profilometry data, the edge of the metal plate during the UV irradiation was located around *x* = 0.

The Eq 4.2 can be employed under the following two assumptions: (1) Most -COOH groups ($pK_a \sim 4.5$) were deprotonated at pH~7 and formed 1:1 ion pairs with probe cations. This assumption was validated by comparing the -COOH density values measured with three different cation-exchange-based approaches (*vide infra*). (2) All the nanopores were oriented perpendicularly to film surface, and had cylindrical shapes with uniform lengths and diameters. In addition, it was hypothesized that –COOH groups were mainly present on the etched, nanoporous PMMA surface, and negligible on PS-based film surface, which is indicated by our previous scanning probe microscopy results[21, 24]: Friction force images showed the etched PMMA surface was more hydrophilic due to the presence of surface –COOH groups at a higher density. And also, Anionic protein molecules were preferentially adsorbed onto the PS-based surface due to electrostatic repulsion from the negatively-charged, etched PMMA surface.

First, the effective density of free -COOH groups was determined for unmodified (native) nanoporous films. Three cation-exchange-based methods were employed for 57K PS-*b*-PMMA-derived nanoporous films (Table 4.1): spectrofluorometric method in aqueous solution with Rhodamine 6G; spectrofluorometric method in ethanol solution with thionine acetate, and ICP-MS method in aqueous solution with Cs^+. Among them, the second method was previously employed to measure the effective –COOH density,[27, 28] because the acetate ion leads to the deprotonation of a surface –COOH group as a base[29] to form a 1:1 ion pair of thionine cation and surface $–COO^-$ group. As shown in Table 4.1, the -COOH density values measured in aqueous solution with Rhodamine 6G (0.79 ± 0.14 /nm^2) was very similar to that (0.86 ± 0.08 /nm^2) measured in ethanol solution with thionine acetate. This result indicates that most of the surface -COOH groups formed 1:1 ion pairs with Rhodamine 6G under the experimental condition. In addition, the density value obtained with Cs^+ (0.81 ± 0.32 /nm^2) was almost identical to that with Rhodamine 6G, indicating that the density values were primarily determined by surface –COOH groups and were not limited by the probe cation size. Based on these results, it is concluded that the three cation-exchange-based methods can be similarly employed to determine the effective surface –COOH density on a nanoporous film. Because of the experimental simplicity, the spectrofluorometric method in aqueous solution with Rhodamine 6G was used for the further investigations.

Table 4.1 Pore Diameters, Densities, and Effective Surface -COOH Densities in PS-b-PMMA-Derived Nanoporous Films.

MW of polymer	Diameter (nm)[a]	Pore density (/μm^2)[a]	-COOH density (/nm^2)
82 000 (82K)	30 ± 3	570 ± 50	0.93 ± 0.12 [7][b]
57 000 (57K)	20 ± 3	890 ± 70	0.79 ± 0.14 [9][b]
			0.81 ± 0.32 [4][c]
			0.86 ± 0.08 [6][d]
43 000 (43K)	14 ± 1	1220 ± 70	0.78 ± 0.07 [6][b]

[a] Measured from AFM images of three separate samples. [b] The average and standard deviation of surface -COOH density measured using Rhodamine 6G as a counter cation. The numbers of samples examined are shown in square brackets. [c] The average and standard deviation of surface -COOH density measured using Cs^+ as a counter cation. The numbers of samples examined are shown in parentheses. [d] The average and standard deviation of surface -COOH density measured using thionine acetate (in ethanol) as a counter cation.[26,27] The numbers of samples examined are shown in parentheses.

Next, the effective surface –COOH density was measured on nanoporous films derived from three types of PS-*b*-PMMA with different molecular weights (82K, 57K and 43K) (Table 4.1). These polymers offer nanoporous films with different pore diameters, and thus were used to investigate the effect of pore diameter on surface –COOH density. The effective density values were very similar for the three types of films. This result indicates the involvement of the same reaction(s) in nanopore formation.

Subsequently, surface -COOH densities were measured on 57K PS-*b*-PMMA-derived nanoporous films modified via amidation or esterification. EDC-mediated aqueous-phase amidation led to decreases in surface –COOH density (Table 4.2 (a)), reflecting the amidation of surface –COOH groups with amine reactants. However, the amidation yields were relatively low (20-30%) under the experimental condition examined (in 0.1 M phosphate buffer, pH 6), as inferred by previous electrochemical results.[19] The low amidation yields were probably

determined by the low efficiency of intermediate reaction with *N*-hydroxysuccinimide in phosphate buffer of pH 6.[13, 30]

Table 4.2 Effective Surface –COOH Densities and Surface Modification Yields on 57K PS-b-PMMA-Derived Nanoporous Films.

Reactant	-COOH density (/nm^2)[a]	Functionalization Yield (%)[b]
(a) Aqueous-phase modification mediated by EDC		
H_2O[c]	0.65 ± 0.03 [4]	18
NH_3 (10 mM in water)	0.56 ± 0.02 [3]	29
$FcCH_2NH_2$[d] (10 mM in water)	0.63 ± 0.01 [3]	20
$(PEO)_4NH_2$[d,e] (10 mM in water)	0.58 ± 0.14 [4]	26
(b) Organic-phase modification using oxalyl chloride		
H_2O	0.82 ± 0.09 [7]	–
ethanol (2 mM in CH_2Cl_2)	0.10 ± 0.01 [4]	88
$FcCO(CH_2)_5OH$[d] (2 mM in CH_2Cl_2)	0.09 ± 0.01 [6]	88
$FcCO(CH_2)_{15}OH$[d] (2 mM in CH_2Cl_2)	0.10 ± 0.02 [12]	87
$FcCH_2NH_2$[d] (2 mM in CH_2Cl_2)	0.10 ± 0.03 [4]	88
$(PEO)_4NH_2$[d,e] (2 mM in CH_2Cl_2)	0.09 ± 0.02 [5]	89

[a] The average and standard deviation of surface –COOH density determined using Rhodamine 6G as a counter cation. The numbers of samples examined are shown in square brackets. [b] The yield was calculated from the average surface –COOH density values for 57K PS-b-PMMA-derived nanoporous films with and without surface modification. [c] Represents the yield of intermediate reaction with *N*-hydroxysuccinimide. [d] The chemical structures are shown in Figure 4.2. [e] Tetraethyleneglycol monoamine.

In addition, the nanopore surface was functionalized via organic-phase amidation/esterification using oxalyl chloride. The organic-phase reactions were applicable for PS-*b*-PMMA-derived nanopores because of their high stability under organic environments: As shown in Figure 4.3, a PS-*b*-PMMA-derived nanoporous film retained the nanoporous structure after organic-phase esterification with $FcCO(CH_2)_{15}OH$. Very similar pore diameters for AFM images in Figure 4.3a and 4.3b (20 ± 3 nm and 19 ± 2 nm, respectively) indicate the high solvent-resistance of the films due to the crosslinking of the PS matrix during UV irradiation.[7, 26, 31] The surface –COOH density after the hydrolysis of acid chloride with water (0.82 ± 0.09 /nm^2; Table 4.2 (b)) was very similar to that of native films (0.79 ± 0.14 /nm^2; Table 4.1), supporting the high stability of the nanoporous structure. Importantly, as compared with aqueous-phase amidation, organic-phase reactions led to much larger decreases in surface –COOH density (Table 4.2 (b)). The surface modification yields were 87–89%, indicating that organic-phase reactions provide efficient means for modifying the nanopore surface. The modification yields were very similar for the different reactants examined, indicating that these reactants were sufficiently small as compared to the pore size and thus could easily access the nanopore surface.

4.4. Conclusions

In this chapter, the density and modification of surface –COOH groups on PS-*b*-PMMA-derived nanoporous films were quantitatively assessed from the amount of probe cations released via cation exchange. Aqueous-phase amidation mediated by EDC is suitable to immobilize biological molecules that are insoluble or denatured in organic solvents. The yields measured in this study were not high, probably due to the presence of phosphate in the solutions.[13, 30] The yield of EDC-mediated aqueous phase amidation can be improved by using an appropriate buffer such as a 2-morpholinoethanesulfonic acid.[13] In contrast, organic-phase amidation and esterification using oxalyl chloride are suitable for functionalizing the solvent-resistive nanoporous films with high modification yields. The high resistance of these films to organic solvents makes it possible to employ various organic-phase reactions for functionalizing the nanopore surface. An appropriate modification method should be chosen according to the applications of nanoporous films. Quantitative information on the surface functionalization will

enable systematic studies of the influences of the surface modification efficiency on the performances of the nanoporous films as chemical separation membranes.

References

1. Hillmyer, M. A. *Adv. Polym. Sci.*, **2005**, 190, 137-181.
2. Olson, D. A.; Chen, L.; and Hillmyer, M. A. *Chem. Mater.*, **2008**, 20, 869-890.
3. Bang, J.; Jeong, U.; Ryu, D. Y.; Russell, T. P.; and Hawker, C. J. *Adv. Mater.*, **2009**, 21, 4769-4792.
4. Ito, T.; and Perera, D. M. N. in *Trace Analysis with Nanomaterials*, eds. D. T. Pierce and J. X. Zhao, Wiley-VCH, Weinheim, Editon edn., **2010**, pp. 341-358.
5. Jackson, E. A.; and Hillmyer, M. A. *ACS Nano*, **2010**, 4, 3548-3553.
6. Yang, S. Y.; Ryu, I.; Kim, H. Y.; Kim, J. K.; Jang, S. K.; and Russell, T. P. *Adv. Mater.*, **2006**, 18, 709-712.
7. Yang, S. Y.; Park, J.; Yoon, J.; Ree, M.; Jang, S. K.; and Kim, J. K. *Adv. Funct. Mater.*, **2008**, 18, 1371-1377.
8. Nuxoll, E. E.; Hillmyer, M. A.; Wang, R.; Leighton, C.; and Siegel, R. A. *ACS Appl. Mater. Interfaces*, **2009**, 1, 888-893.
9. Phillip, W. A.; O'Neill, B.; Rodwogin, M.; Hillmyer, M. A.; and Cussler, E. L. *ACS Appl. Mater. Interfaces*, **2010**, 2, 847-853.
10. Yang, S. Y.; Yang, J.-A.; Kim, E.-S.; Jeon, G.; Oh, E. J.; Choi, K. Y.; Hahn, S. K.; and Kim, J. K. *ACS Nano*, **2010**, 4, 3817-3822.
11. Baker, L. A.; Jin, P.; and Martin, C. R. *Crit. Rev. Solid State Mater. Sci.*, **2005**, 30, 183-205.
12. Zalusky,A. S.; Olayo-Valles, R.; Wolf, J. H.; and Hillmyer, M. A. *J. Am. Chem. Soc.*, **2002**, 124, 12761-12773.
13. Rzayev, J.; and Hillmyer, M. A. *J. Am. Chem. Soc.*, **2005**, 127, 13373-13379.
14. Bailey, T. S.; Rzayev, J.; and Hillmyer, M. A. *Macromolecules*, **2006**, 39, 8772-8781.
15. Klaikherd, A.; Ghosh, S. and Thayumanavan, S. *Macromolecules*, **2007**, 40, 8518-8520.
16. Ryu, J.-H.; Park, S.; Kim, B.; Klaikherd, A.; Russell, T. P.; and Thayumanavan, S. *J. Am. Chem. Soc.*, **2009**, 131, 9870-9871.
17. Yang, S. Y.; Son, S.; Jang, S.; Kim, H.; Jeon, G.; Kim, W. J.; and Kim, J. K. *Nano Lett.*, **2011**, 11, 1032-1035.
18. Li, Y.; Maire, H. C.; and Ito, T. *Langmuir*, **2007**, 23, 12771-12776.
19. Li, Y.; and Ito, T. *Langmuir*, **2008**, 24, 8959-8963.

20. Li, Y.; and Ito, T. *Anal. Chem.*, **2009**, 81, 851-855.
21. Ibrahim, S.; and Ito, T. *Langmuir*, **2010**, 26, 2119-2123.
22. Thurn-Albrecht, T.; Steiner, R.; DeRouchey, J.; Stafford, C. M.; Huang, E.; Bal, M.; Tuominen, M.; Hawker, C. J.; and Russell, T. P. *Adv. Mater.*, **2000**, 12, 787-791.
23. Maire, H. C.; Ibrahim, S.; Li, Y.; and Ito, T. *Polymer*, **2009**, 50, 2273-2280.
24. Ito, T.; Grabowska, I.; and Ibrahim, S. *Trends Anal. Chem.*, **2010**, 29, 225-233.
25. Bard, A. J.; and Faulkner, L. R. *Electrochemical Methods, Fundamentals and Applications, 2nd Ed.*, Wiley, New York, **2001**.
26. Jeong, U., Ryu, D. Y.; Kim, J. K.; Kim, D. H.; Russell, T. P.; and Hawker, C. J. *Adv. Mater.*, **2003**, 15, 1247-1250.
27. Papra, A.; Hicke, H.-G. and Paul, D. *J. Appl. Polym. Sci.*, **1999**, 74, 1669-1674.
28. Geismann, C.; and Ulbricht, M. *Macromol. Chem. Phys.*, **2005**, 206, 268-281.
29. Odashima, K.; Ito, T.; Tohda, K.; and Umezawa, Y. *Chem. Pharm. Bull.*, **1998**, 46, 1248-1253.
30. Gilles, M. A.; Hudson, A. Q.; and Borders, Jr., C. L. *Anal. Biochem.*, **1990**, 184, 244-248.
31. Perera, D. M. N. T.; Pandey, B.; and Ito, T. *Langmuir*, **2011**, DOI: 10.1021/la202005n.
32. Baramee, A.; Coppin, A.; Mortuaire, M.; Pelinski, L.; Tomavo, S.; and Brocard, J. *Bioorg. Med. Chem.*, **2006**, 14, 1294-1302.
33. Creager, S. E.; and Rowe, G. K. *J. Electroanal. Chem.*, **1994**, 370, 203-211.

Chapter 5 - Linker-Based Control of Electron Propagation through Ferrocene Moieties Covalently Anchored onto Insulator-Based Nanopores Derived from a Polystyrene-Poly(methylmethacrylate) Diblock Copolymer

Reproduced by permission of The American Chemical Society
Published as: Li, F., Pandey, B., Ito, T. *Langmuir.* **2012**, *28*, 16496-16500

5.1. Introduction

Electron propagation through redox sites plays an essential role in the function of redox polymers consisting of isolated (unconjugated) redox moieties covalently or electrostatically linked to polymer backbones.[1,2] Redox polymer films have been deposited on electrodes, and employed for electrocatalysis[3] and electrochemical sensing.[4] For these applications, electrons (or holes) generated by redox reaction on the electrode surface need to efficiently propagate through the film. Knowledge of the charge propagation mechanism is required to design redox polymer films suitable for the aforementioned applications. In addition, the knowledge may also provide valuable insight into long-range electron transfer in biological systems (e.g., photosynthesis)[5] and organic electronics.[6,7]

Although the characteristics of electron propagation in redox polymer films were investigated extensively and systematically, they could not be directly correlated with molecular-level mechanisms because of the undefined distribution of the redox sites. Thus, investigations of electron propagation were attempted for more controlled, surface/interface-localized redox amphiphiles, including monolayers deposited on hydrophobic anodic alumina nanopores[8,9] and Langmuir-Blodgett monolayers at the air-solution interface.[10,11] However, since the amphiphiles in these monolayers were not covalently anchored onto immobile supports, their physical diffusion and aggregate formation made the quantitative discussion of electron propagation difficult. More recently, electron propagation through redox moieties covalently anchored onto insulator-based nanoscale structures such as dendrimers,[12,13] silica nanoparticles[14,15] and

nanocrystalline cellulose[16] was investigated. Since the redox moieties were covalently anchored to the nanostructure surfaces, electron propagation through the anchored redox moieties originated from electron hopping based on bounded diffusion.[17] According to the theoretical study,[17] the apparent diffusion coefficient controlled by bounded diffusion (D_{ap}) should be affected by the range of the physical displacement of redox moieties. However, to the best of our knowledge, there is no report that has experimentally demonstrated the effects of physical displacement range on electron propagation efficiency.

In this chapter we will discuss the effects of alkyl linker length on the efficiency of electron propagation through ferrocene moieties covalently anchored onto insulator-based nanopores (Figure 1).

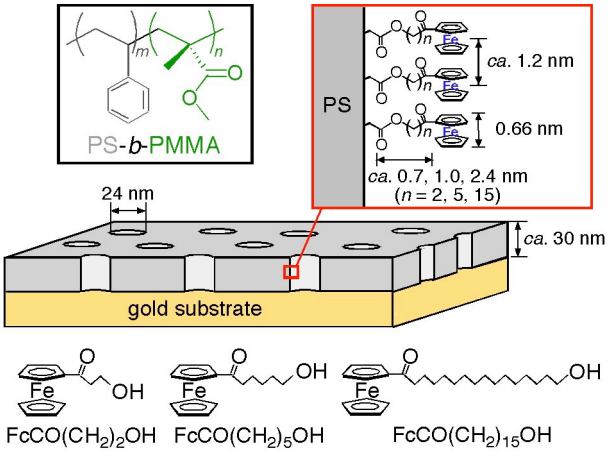

Figure 5.1 Schematic illustration of a gold-supported CF-PS-*b*-PMMA-derived nanoporous film decorated with ferrocene moieties. The molecular structures of PS-*b*-PMMA and $FcCO(CH_2)_nOH$ (n = 2, 5, 15) are also shown.

Polystyrene-based films (*ca.* 30 nm thick) comprising cylindrical nanopores (24 nm in diameter) oriented perpendicular to an underlying gold electrode were fabricated from a cylinder-forming polystyrene-poly(methylmethacrylate) diblock copolymer (CF-PS-*b*-PMMA).[18,19] The surface of the nanopores was subsequently modified via esterification of surface COOH groups with ferrocene derivatives with different alkyl linker lengths ($FcCO(CH_2)_nOH$; n = 2, 5, 15).[20] These nanopores directly contacted to the underlying electrode with no leakage, permitting for direct electrochemical measurements of electron propagation from/toward the redox sites anchored onto the insulator-based nanopore surface. Average spacing between adjacent ferrocene moieties (ca. 1.2 nm) was larger than the size of ferrocene (ca. 0.66 nm in diameter),[21] and thus electron propagation could take place only when adjacent

ferrocene moieties could approach closely enough for electron self-exchange reaction. The linker length defined the physical displacement range of surface-anchored ferrocene moieties, leading to the control of electron propagation efficiency.

5.2. Experimental Section

5.2.1. Chemicals and Materials

CF-PS-*b*-PMMA (71K CF-PS-*b*-PMMA: M_n = 48 000 g/mol for PS and 23 000 g/mol for PMMA, M_w/M_n = 1.07) were purchased from Polymer Source and used as received. Oxalyl chloride (Acros), dichloromethane (Fisher), ferrocene (Aldrich), aluminum chloride ($AlCl_3$, Acros), 3-bromopropanoic acid (Aldrich), magnesium sulfate (Fisher), Rhodamine 6G (Aldrich), 1-hexadecanethiol (Acros), sodium tetrafluoroborate (Acros) and glacial acetic acid (AcOH) were used as received. Gold-coated Si wafers, which were prepared by sputtering 10 nm of Ti followed by 200 nm of Au onto Si (100) wafers, were purchased from LGA Thin Films (Foster City, CA). 16-hydroxy-1-oxohexadecylferrocene and 6-hydroxy-1-oxohexylferrocene was synthesized in chapter 4. All aqueous solutions were prepared with water having a resistivity of 18 MΩ cm or higher (Barnstead Nanopure Systems).

5.2.2. Synthesis of 3-Hydroxy-1-Oxopropylferrocene

^{1}H- and ^{13}C-NMR spectra were measured on a Varian INOVA 400 Fourier transform NMR spectrometer, and chemical shifts were reported in δ values in ppm downfield of tetramethylsilane. FTIR-ATR spectra were measured on an Agilent Cary 630 spectrophotometer. Exact MS data were measured at the Mass Spectroscopy Laboratory, University of Kansas.

5.2.2.1. Synthesis of 3-Bromo-1-Oxopropylferrocene

3-Bromopropanoic acid (0.3 g, 1.96 mmol) and oxalyl chloride (3 mL, 35 mmol) were mixed together and stirred at room temperature overnight. The extra oxalyl chloride was removed under vacuum to obtain a colorless solid. Anhydrous dichloromethane (5 mL) was added to the flask to dissolve the solid, and then anhydrous $AlCl_3$ (0.31 g, 2.30 mmol) was added to the solution and stirred for 20 min at 0 °C under argon. In a separate flask, ferrocene (0.43 g, 2.30 mmol) was dissolved in 5 mL of anhydrous dichloromethane. The acid-chloride-containing

solution was transferred to the ferrocene-containing solution via cannula over a period of 5 min. The solution turned purple during this addition. After stirring for 2 h, 5 mL of water was added slowly. After additional stirring for 10 min, the solution was diluted with 25 mL dichloromethane. The organic layer was collected, washed with water until the pH of the aqueous phase became neutral, and dried over $MgSO_4$. The solvent was removed, and then purified by silica gel column chromatography (eluent: dichloromethane) to give 3-bromo-1-oxopropylferrocene as an orange solid (0.54 g, 85%). ^{1}H-NMR ($CDCl_3$) δ 4.81 (t, J = 2.0 Hz, 2H, C_p), 4.55 (t, J = 2.0 Hz, 2H, C_p), 4.27 (s, 5H, $C_{p'}$), 3.75 (t, J = 6.4 Hz, 2H, CH_2Br), 3.32 (t, J = 6.4 Hz, 2H, $COCH_2$). ^{13}C-NMR ($CDCl_3$) δ 200.86, 78.49, 72.80, 70.16, 69.47, 42.57, 26.24.

5.2.2.2. Synthesis of 3-Hydroxy-1-Oxopropylferrocene

3-Bromo-1-oxopropylferrocene (0.30 g, 0.93 mmol) was mixed with sodium hydroxide solution (3 M, 15 mL), and then refluxed for 1 hour. The mixture was extracted by ethyl acetate (3 × 30 mL). The organic phase was washed by brine, and then dried over $MgSO_4$. The solvent was removed, and then purified by silica gel column chromatography (eluent: dichloromethane: ethyl acetate = 7:3) to give 3-hydroxy-1-oxopropylferrocene as an orange oil (0.21 g, 89%). ^{1}H-NMR ($CDCl_3$) δ 4.81 (t, J = 2.0 Hz, 2H, C_p), 4.55 (t, J = 1.8 Hz, 2H, C_p), 4.24 (s, 5H, $C_{p'}$), 2.99 (t, J = 5.2 Hz, 2H, $COCH_2$), 2.80 (t, J = 6.0 Hz, 2H, CH_2OH). ^{13}C-NMR ($CDCl_3$) δ 205.52, 78.75, 72.85, 70.21, 69.52, 58.55, 41.36. FTIR (cm^{-1}): 3341, 3098, 2938, 2883, 1643, 1452, 1378, 1261, 1224, 1080, 1055, 1027, 1002, 822. Exact MS: *m/z* calculated for $C_{13}H_{14}O_2Fe$ (M + H), 259.0421; found, 259.0401.

5.2.3. Preparation of CF-PS-b-PMMA-Derived Nanoporous Films

CF-PS-*b*-PMMA-derived nanoporous films on gold electrodes were prepared according to procedures reported chapter 4. Gold-coated Si wafers were sonicated in ultra pure water and ethanol for 30 min, and then cleaned in a Novascan PSD-UVT UV-ozone system for 60 min prior to use. Thin films of CF-PS-*b*-PMMA were prepared on cleaned gold substrates by spin-coating (2000 rpm) from its toluene solution (0.6% (w/w)) and annealed at 170 °C in vacuum (ca. 0.3 Torr) for 60 h. According to AFM images, annealed CF-PS-*b*-PMMA films with thickness of *ca.* 30 nm comprised cylindrical PMMA domains oriented perpendicularly to the film surface. The PMMA domains were removed by irradiation with UV light using a Novascan

PSD-UVT UV-ozone system (ca. 20 mW/cm^2) under an Ar atmosphere and by subsequently immersing in AcOH.

The thickness of annealed CF-PS-*b*-PMMA films prior to the UV irradiation was measured using a J. A. Woollam alpha-SE spectroscopic ellipsometer. The ellipsometric thickness of an annealed film was used as the thickness of the nanoporous film obtained by the UV/AcOH treatment.

5.2.4. Surface Functionalization of CF-PS-b-PMMA-Derived Nanopores

CF-PS-*b*-PMMA-derived nanoporous films on gold were immersed in oxalyl chloride, and heated at 50 ºC overnight. After excess oxalyl chloride was removed under vacuum, the films were soaked in a dichloromethane solution of an alcohol reactant (2 mM) at room temperature for 2 h. The samples were washed with dichloromethane and dried. The surface COOH density and surface functionalization yield were determined via a cation exchange method with Rhodamine 6G. Molecular lengths shown in Figure 5.1 were estimated with Avogadro.

5.2.5. Electrochemical Measurements

CV measurements were performed in a three-electrode cell containing a Ag/AgCl (3 M KCl) reference electrode and a Pt counter electrode using a CH Instruments model 618B electrochemical analyzer.[2-4] A polymer-coated gold substrate (serving as the working electrode) was immobilized at the bottom of the cell. The diameter of the film area in contact with the solution, which was defined by an O-ring between the upper cell and the working electrode, was 0.8 cm. CV measurements were performed in aqueous solutions deoxygenated by bubbling and purging with Ar at room temperature (*ca*. 20 °C).

5.3. Results and Discussion

5.3.1. Total Contact Length Determinations of Functionalized Nanoporous Films

The total contact length between nanopores and gold electrode (L) was calculated using the following equation by assuming that all the nanopores have a cylindrical shape of d = 24 nm:

$$L = \pi d N_{\text{pore}} \qquad \text{Eq 5.1}$$

The number of open nanopores in a film (N_{pore}) was estimated from a charge originating from the reductive desorption of a 1-hexadecanethiol monolayer formed on the gold surfaces exposed at the bottom of the nanopores.[22,23] An electrode employed for CV measurements in 0.1 M $NaBF_4$ was washed with water and then ethanol without disassembling the cell. Subsequently, an ethanolic solution of 1-hexadecanethiol (0.1 mM) was placed into the reservoir overnight for the formation of a self-assembled monolayer (SAM) of 1-hexadecanethiol on the exposed gold surface. After washing with ethanol and water, 0.5 M KOH was placed into the reservoir. A charge due to the reductive desorption of 1-hexadecanethiol around -1.1 V was measured to calculate the exposed gold area (A_{gold}) from a comparison with that at planar gold substrates modified with 1-hexadecanethiol SAMs. CV is shown in Figure 5.2.

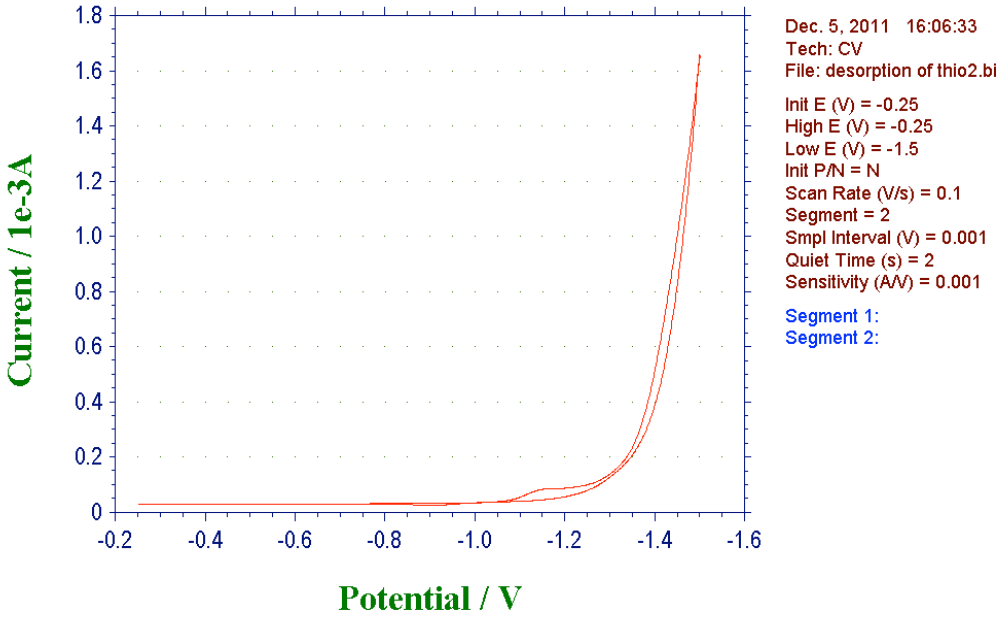

Figure 5.2 CV of due to the reductive desorption of 1-hexadecanethiol in 0.5M KOH

The number of open nanopores (N_{pore}) was estimated using the following equation by assuming that the pores were perfectly cylindrical and the pore radius ($r = d/2$; d: pore diameter) was uniform; $N_{pore} = A_{gold}/\pi r^2$. The line electrode was calculated using **Eq 5.1,** where d is the diameter of the nanopore measured by AFM (24nm). Due to the variation of the density of nanopores penetrating through a film to an underlying gold electrode,[24,25] L of films employed in this work varied in the range between 4.5 x 10^4 cm and 1.4 x 10^5 cm. Very similar CV data were repeatedly obtained for a gold-supported, ferrocene-modified nanoporous film during a series of measurements for more than 3 hours.

Table 5.1 Surface Density of Ferrocene Moieties (Γ), Apparent Diffusion Coefficients (Dap), and Maximum Electron Propagation Distances (h) Measured at CF-PS-b-PMMA-Derived Nanoporous Films Modified with Ferrocene Derivatives.

Reactant	Γ(mol/cm^2) [a]	D_{ap} (cm^2/s) [b]	h (nm) [b]
$FcCO(CH_2)_{15}OH$	(1.33 ± 0.10) x 10^{-10} [3]	(2.3 ± 1.7) x 10^{-12} [7]	7.3 ± 3.1 [7]
$FcCO(CH_2)_5OH$	(1.31 ± 0.04) x 10^{-10} [3]	(2.8 ± 2.4) x 10^{-13} [4]	2.6 ± 1.0 [4]
$FcCO(CH_2)_2OH$	(1.33 ± 0.15) x 10^{-10} [4]	–[c] [3]	–[c] [3]

[a] The average and standard deviation of Γ calculated from the difference in surface -COOH densities between native nanoporous films (0.90 ± 0.08 nm^{-2}; Newly measured on nanoporous films derived from 71K CF-PS-*b*-PMMA) and ferrocene-modified nanoporous films, which were measured based on the cation exchange method with fluorescence spectrometry. The yields of the surface esterification were 88-89%. Detailed procedures were reported previously.[20] The number of samples examined are shown in square brackets. [b] The average and standard deviation obtained from CV data. The standard deviation values are calculated from data measured at different samples independently prepared on different days. The numbers of samples examined are shown in square brackets. [c] Electron propagation was not observed.

5.3.2. Effect of Linker Length on Electon Hopping Process

Figure 5.3 shows CV data measured at different scan rates (v) in 0.1 M $NaBF_4$ for gold-supported nanoporous films modified with (a) $FcCO(CH_2)_{15}OH$, (b) $FcCO(CH_2)_5OH$ and (c) $FcCO(CH_2)_2OH$. Redox peaks around +0.2 ~ +0.4 V (vs. Ag/AgCl) were clearly observed for films decorated with the ferrocene derivatives having relatively long alkyl chains (Figure 5.3 a,b). Since there was no free ferrocene molecule dissolved in the solution, the Faradaic peaks should originate from the surface-anchored ferrocene moieties. In contrast, no redox peak was observed for the ferrocene derivative with the shortest alkyl chain (Figure 5.3c). The average spacing between adjacent ferrocene moieties (ca. 1.2 nm, calculated from the Γ values in Table 5.1) was larger than the size of the ferrocene moiety (ca. 0.66 nm in diameter).[21] Thus, adjacent ferrocene moieties anchored to the nanopore surface needed to approach closely enough for electron self-exchange reaction. The CV data indicate that the ferrocene moieties with the

shortest chain could not be close enough for electron propagation due to their limited physical displacement range reflecting the short linker length (*ca.* 0.7 nm) and also their restricted mobility by the covalent attachment to the nanopore surface. It should be noted that physisorbed ferrocenes did not offer the Faradaic peaks as shown in Figure 5.3 (a,b): As a control experiment, no Faradaic peak around the potential range was observed for gold-supported nanoporous films that were immersed in solutions of the ferrocene derivatives without oxalyl chloride treatment.

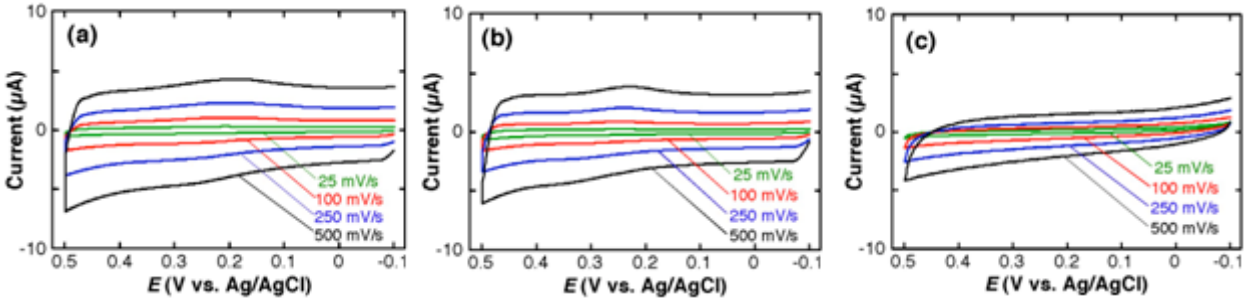

Figure 5.3 Cyclic voltammograms obtained for gold-supported nanoporous films modified with (a) $FcCO(CH_2)_{15}OH$ (L = 3.5 x 10^4 cm), (b) $FcCO(CH_2)_5OH$ (L = 1.4 x 10^5 cm) and (c) $FcCO(CH_2)_2OH$ (L = 4.0 x 10^4 cm). Measured in aqueous 0.1 M $NaBF_4$ at room temperature (ca. 20 °C).

Figure 5.4 shows the relationship between anodic peak current divided by L and $v^{1/2}$ ($i_p/(L \bullet v^{1/2})$) as a function of $v^{1/2}$.[12,13] For both $FcCO(CH_2)_{15}OH$ and $FcCO(CH_2)_5OH$, $i_p/(L \bullet v^{1/2})$ increased proportionally to $v^{1/2}$ at the slower v, and then became similar at the faster v. The former was consistent with a voltammogram for surface-adsorbed redox species, reflecting the Faradaic reaction of all the ferrocene moieties (= $Lh\Gamma$) within the maximum electron hopping length (h). Thus, $i_p/(L \bullet v^{1/2})$ obtained at the slower v followed Eq 5.2:

$$\frac{i_p}{Lv^{1/2}} = \frac{F^2}{4RT} h\Gamma v^{1/2} \qquad \text{Eq 5.2}$$

In this equation for a one-electron Faradaic reaction, R, T and F are the gas constant, temperature and Faraday's constant, respectively. At the faster v, only ferrocene moieties close to the electrode could react during the time scale of the CV measurements, which corresponds to a diffusion-controlled voltammogram. Thus, $i_p/(L \bullet v^{1/2})$ obtained at the faster v was almost constant regardless of $v^{1/2}$, as described by Eq 5.3:[10,11]

$$\frac{i_p}{Lv^{1/2}} = 2.69 \times 10^5 \Gamma D_{ap}^{1/2} \qquad \text{Eq 5.3}$$

Thus, D_{ap}, the apparent diffusion coefficient due to electron hopping, could be determined from the $i_p/(L \bullet v^{1/2})$ values at the plateau. The larger $i_p/(L \bullet v^{1/2})$ for $FcCO(CH_2)_{15}OH$ as compared with $FcCO(CH_2)_5OH$ shown in Figure 5.4 reflected the larger D_{ap}, and thus more efficient electron propagation. Indeed, the D_{ap} value for $FcCO(CH_2)_{15}OH$ was reproducibly one-order larger than that for $FcCO(CH_2)_5OH$ (Table 5.1) in spite of the variation of L. These results, including no electron propagation for $FcCO(CH_2)_2OH$, revealed that electron propagation was more efficient through redox sites anchored by longer linkers. Considering that the longer linker gave the larger physical displacement range for the anchored redox moieties, the trend shown here was consistent with the theoretical study for electron hopping based on bounded diffusion.[17] On the other hand, the D_{ap} values ($10^{-12} \sim 10^{-13}$ cm^2/s) were much smaller than the diffusion coefficient of ferrocene compounds dissolved in aqueous solution (ca. 5×10^{-6} cm^2/s).[26] The small D_{ap} may be ascribed to the restricted mobility of the surface-anchored ferrocene moieties. Even smaller D_{ap} (*ca.* 10^{-15} cm^2/s) was recently reported for electron propagation through ferrocene moieties anchored to nanocrystalline cellulose, which would reflect the limited mobility of the redox moieties tethered in close proximity to the solid surface through rigid linkers.[16]

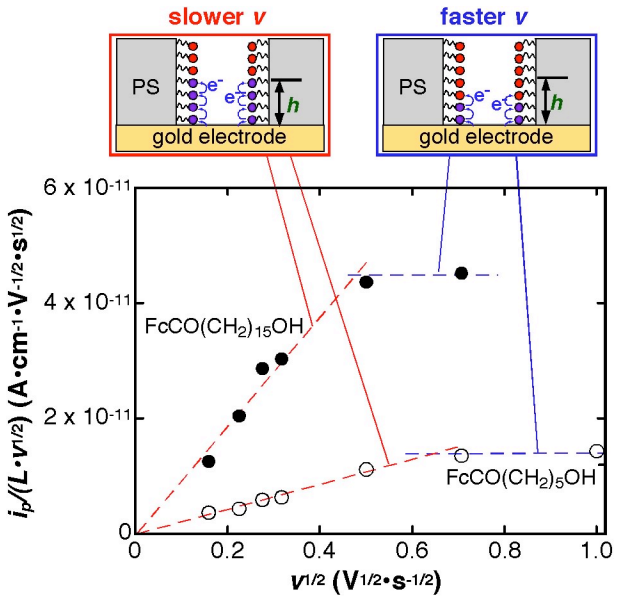

Figure 5.4 Relationship between $i_p/(L \bullet v^{1/2})$ and $v^{1/2}$ obtained at gold-supported nanoporous films modified with $FcCO(CH_2)_{15}OH$ (filled circles) and $FcCO(CH_2)_5OH$ (open circles). CVs of these films are shown in Figure 5.2a and 5.2b, respectively.

5.3.4. Effect of Linker Length on Maximum Electron Propagation Distance

The maximum electron propagation distance, h, can be obtained from the transition scan rate (v_t), which is determined from the intersection of the two lines obtained from Eq 5.2 and Eq 5.3:

$$h = \frac{D_{ap}^{1/2}}{3.492 v_t^{1/2}} \qquad \text{Eq 5.4}$$

As summarized in **Table 5.1**, h was larger with the longer linker. Furthermore, the h values (*ca.* 7 nm for $FcCO(CH_2)_{15}OH$; *ca.* 3 nm for $FcCO(CH_2)_5OH$) were significantly smaller than the film thickness (*ca.* 30 nm), indicating that not all the anchored ferrocene moieties could react. This observation was supported by the anodic charges measured from the CVs: The number of ferrocene moieties oxidized at v = 25 mV/s provided the electron propagation distances of 4.5 ± 2.2 and 1.8 ± 0.6 nm for $FcCO(CH_2)_{15}OH$ and $FcCO(CH_2)_5OH$ as shown in table 5.2, respectively. The limited electron propagation distance may attribute to the presence of defects in the ferrocene layers or non-uniform surface distribution of ferrocene moieties.

Table 5.2 Maximum Electron Hopping Distance (h) Between the Value Calculated from Charge Values Obtained from CV Data and from the Faradiac Current.

Reactant	Γ(mol/cm^2)	h (nm) [a]	h (nm) [b]
$FcCO(CH_2)_{15}OH$	(1.33 ± 0.10) x 10^{-10} [3]	4.5 ± 2.2 [7]	7.3 ± 3.1 [7]
$FcCO(CH_2)_5OH$	(1.31 ± 0.04) x 10^{-10} [3]	1.8 ± 0.6 [4]	2.6 ± 1.0 [4]
$FcCO(CH_2)_2OH$	(1.33 ± 0.15) x 10^{-10} [4]	–[c] [3]	–[c] [3]

[a] The average and standard deviation of h calculated from the charge obtained from CV data. [b] The average and standard deviation obtained from CV data. The standard deviation values are calculated from data measured at different samples independently prepared on different days. The numbers of samples examined are shown in square brackets. [c] Electron propagation was not observed.

5.4. Conclusions

This chapter In conclusion, this study experimentally showed the influence of linker length on electron propagation through ferrocene moieties anchored to an insulator-based nanopore surface. The cylindrical nanopores with well-defined shapes and surface properties made it possible to estimate the parameters representing the electron propagation such as very small D_{ap} and nanoscale h. Ferrocene moieties anchored through the longer linkers exhibited more efficient electron propagation, as shown by the theoretical study about electron hopping based on bounded diffusion.[17] This trend suggests that electron propagation efficiency through redox sites anchored to an insulator-based surface can be controlled by varying the properties of a linker. The linker-based control of electron propagation will lead to designing novel electronic devices and electrochemical sensors based on insulator surfaces modified with redox moieties.[27]

References

1. Majda, M. *Molecular Design of Electrode Surfaces*; Murray, R. W., Ed.; Wiley & Sons: New York, **1992**; pp 159-206.
2. Kaneko, M. *Prog. Polym. Sci.* **2001**, *26*, 1101-1137.
3. Andrieux, C. P.; Saveant, J.-M. *Molecular Design of Electrode Surfaces*; Murray, R. W., Ed.; Wiley & Sons: New York, **1992**; pp 207-270.
4. Wilson, G. S.; Hu, Y. *Chem. Rev.* **2000**, *100*, 2693-2704.
5. Giese, B.; Graber, M.; Cordes, M. *Curr. Opin. Chem. Biol.* **2008**, *12*, 755-759.
6. Terrill, R. H.; Murray, R. W., *Molecular Electronics: A 'Chemistry for the 21st Century' Monograph*; Jortner, J.; Ratner, M., Eds.; Blackwell Science: Malden, MA, USA, **1997**; pp 215-239.
7. Oyaizu, K.; Nishide, H. *Adv. Mater.* **2009**, *21*, 2339-2344.
8. Miller, C. J.; Widrig, C. A.; Charych, D. H.; Majda, M. *J. Phys. Chem.* **1988**, *92*, 1928-1936.
9. Goss, C. A.; Miller, C. J.; Majda, M. *J. Phys. Chem.* **1988**, *92*, 1937-1942.
10. Lee, W.-Y.; Hostetler, M. J.; Murray, R. W.; Majda, M. *Isr. J. Chem.* **1997**, *37*, 213-223.
11. Lee, W.-Y.; Majda, M.; Brezeinski, G.; Wittek, M.; Mobius, D. *J. Phys. Chem. B* **1999**, *103*, 6950-6956.
12. Amatore, C.; Bouret, Y.; Maisonhaute, E.; Goldsmith, J. I.; Abruna, H. D. *ChemPhysChem* **2001**, *2*, 130-134.
13. Amatore, C.; Bouret, Y.; Maisonhaute, E.; Goldsmith, J. I.; Abruna, H. D. *Chem. Eur. J.* **2001**, *7*, 2206-2226.
14. Budny, A.; Novak, F.; Plumere, N.; Schetter, B.; Speiser, B.; Straub, D.; Mayer, H. A.; Reginek, M. *Langmuir* **2006**, *22*, 10605-10611.
15. Beasley, C. A.; Murray, R. W. *Langmuir* **2009**, *25*, 10370-10375.
16. Eyley, S.; Shariki, S.; Dale, S. E. C.; Bending, S.; Marken, F.; Thielemans, W. *Langmuir* **2012**, *28*, 6514-6519.
17. Blauch, D. N.; Saveant, J.-M. *J. Am. Chem. Soc.* **1992**, *114*, 3323-3332.
18. Li, Y.; Maire, H. C.; Ito, T. *Langmuir* **2007**, *23*, 12771-12776.
19. Maire, H. C.; Ibrahim, S.; Li, Y.; Ito, T. *Polymer* **2009**, *50*, 2273-2280.
20. Li, F.; Diaz, R.; Ito, T. *RSC Adv.* **2011**, *1*, 1732-1736.

21. Landis, E. C.; Hamers, R. J. *J. Phys. Chem. C* **2008**, *112*, 16910-16918.
22. Widrig, C. A.; Chung, C.; Porter, M. D. *J. Electroanal. Chem.* **1991**, *310*, 335–359.
23. Ito, T. *J. Electroanal. Chem*. **2001**, *495*, 87–97.
24. Perera, D. M. N. T.; Pandey, B.; Ito, T. *Langmuir* **2011**, *27*, 11111-11117.
25. Pandey, B.; Tran Ba, K. H.; Li, Y.; Diaz, R.; Ito, T. *Electrochim. Acta* **2011**, *56*, 10185-10190.
26. Fan, F.-R. F. *J. Phys. Chem. B* **1998**, *102*, 9777-9782.
27. Fabre, B. *Acc. Chem. Res.* **2010**, *43*, 1509-1518.

Chapter 6 - Recessed Nanodisk-Array Electrodes with Ferrocene-Functionalized Nanopores for Electrochemical Sensing

6.1. Introduction

Ferrocene containing structures with molecular recognition binding sites have received much attention in recent years since ferrocene is a good candidate for designing redox molecular switches and sensors by conjugation with molecules involved in molecular recognition processes. Previous studies using ferrocene containing structures for electrochemical sensing mainly focus on developing redox receptors for anions and cations.[1-4] In this chapter, a construction of redox switches and sensors for neutral organic molecules in aqueous solution based on the control of electron hopping via host-guest complexation in nanopores derived from PS-b-PMMA thin films will be introduced.

Electron hopping through redox sites in the redox polymer films consisting of isolated (unconjugated) redox moieties covalently or electrostatically linked to polymer backbones plays an essential role in the function of electrochemical sensing. [5-7] As shown in our previous studies in chapter 4 and 5, polystyrene-based films (*ca.* 30 nm thick) comprising cylindrical nanopores (24 nm in diameter) oriented perpendicular to an underlying gold electrode can be fabricated from a cylinder-forming polystyrene-poly(methylmethacrylate) diblock copolymer (CF-PS-*b*-PMMA).[8,9] The inner surface of nanopores covered by COOH groups with average spacing of 1.3 nm for 71K PS-b-PMMA derived nanopores and 1.2 nm for 57K PS-b-PMMA derived nanopores have been proved in our previous works.[10,11] The surface of the nanopores can be subsequently modified with redox active functional groups via esterification or amidation in aqueous or organic solution.[12-14] According to the theoretical study, the apparent diffusion coefficient of the electron hopping through those anchored redox sites is affected by the range of the physical displacement of redox moieties. The controlling of the electron hopping efficiency based on the changing the linker length between redox centers and anchor sites has been clearly demonstrated in previous work.[14] Another way to control the efficiency of the electron transport is controlling the number of redox sites according to the theory.

The covalent incorporation of redox active groups onto macromolecules based nanostructures such as dendrimers have been an important area of chemical research. These nanostructures have been employing as scaffolds for controlling the number of multiple functional groups on their periphery by applying the interactions between a nonelectroactive host and an electroactive guest. Lots of modified electrode surface having molecular recognition properties for sensing enzymes,[15,16] genetic materials,[17,18] antibodies have been produced based on these nanostructures.[19,20]

Electrochemical studies for the formation of host-guest inclusion complexes by following the changes in the redox activity behavior of an electroactive moiety have been studied for decades. [21-23] Ferrocene containing molecules have been used for electrochemical studies as common electroactive moieties due to their electrochemical properties. [21] The most common molecule to form a complex with ferrocene moieties is cyclodextrin.[22,23] Cyclodextrins have a basket like structure by linking cyclic oligomers of D-(+)-glucopyranose units through an alfa-1,4-glycoside bond. This structure gives cyclodextrins the most important features: hydrophilic exterior and hydrophobic cavity. Thus cyclodextrins can catch hydrophobic compounds with size and shape matching their cavity such as ferrocene to form 1:1 host-guest complexes in aqueous solution. Kaifer's group did the electrochemistry measurement on a self-assembled monolayer with β-cyclodextrin (β-CD) as ferrocene redox moiety receptor.[24] According to Kaifer's results, by forming complexes between ferrocene and β-CD receptor on the electrode surface, a decrease in the peak current are observed in voltammograms which can be explained by the fact that the electron transfer reaction in the presence of the cyclodextrin will only take place on the free ferrocene after decomplexation from β-CD.[25] Same electrochemical phenomenon has been reported on a PAMAM dendrimers modified with ferrocene which tethered on to electrode surface treated by β-CD with varies concentrations.[32] Given this electrochemical behavior, the attachment of Fc to β-CD should enable the construction of redox switches and sensors for organic molecules in aqueous solution. The sensing system would be based on competition between the covalently attached Fc and the guest for the CD cavity. Thus, guest binding to CD must be preceded by decomplexation of the Fc moiety.

In this chapter, we present covalent modification of cylindrical nanopores based on polystyrene thin films with ferrocene. With these modified thin films coated on gold electrodes, we have conducted electrochemical studies. This study investigates the electron hopping

efficiency affected by controlling the number of redox sites resulting from the interfacial formation of 1:1 complexes of ferrocene and β-CD. According to our observation, the electron hopping efficiency indicated by faradic currents decreased with increasing the concentration of β-CD in aqueous solution. The current could be recovered by adding redox-inactive guest molecules of adamantanol to the solution. These results indicate that knowledge of this mechanism for this system may provide valuable convenient model to design redox switches and sensors for neutral organic molecules in aqueous solution based on redox-involved electron hopping and host-guest chemistry.

6.2. Experimental Section

6.2.1. Chemicals and Materials

CF-PS-*b*-PMMA (71K CF-PS-*b*-PMMA: M_n = 48 000 g/mol for PS and 23 000 g/mol for PMMA, M_w/M_n = 1.07; 57K PS-*b*-PMMA: M_n = 39 800 g/mol for PS and 17 000 g/mol for PMMA, M_w/M_n = 1.06) were purchased from Polymer Source and used as received. Oxalyl chloride (Acros), dichloromethane (Fisher), β-cyclodextrin (Fisher), 1-adamantanol (Fisher), 1-hexadecanethiol (Acros), sodium tetrafluoroborate (Acros) and glacial acetic acid (AcOH) were used as received. Gold-coated Si wafers, which were prepared by sputtering 10 nm of Ti followed by 200 nm of Au onto Si (100) wafers, were purchased from LGA Thin Films (Foster City, CA). 16-hydroxy-1-oxohexadecylferrocene was synthesized in chapter 4. All aqueous solutions were prepared with water having a resistivity of 18 MΩ cm or higher (Barnstead Nanopure Systems).

6.2.2. Preparation of CF-PS-b-PMMA-Derived Nanoporous Films

CF-PS-*b*-PMMA-derived nanoporous films on gold electrodes were prepared according to procedures reported chapter 4 and 5. Gold-coated Si wafers were sonicated in ultra pure water and ethanol for 30 min, and then cleaned in a Novascan PSD-UVT UV-ozone system for 60 min prior to use. Thin films of CF-PS-*b*-PMMA were prepared on cleaned gold substrates by spin coating (2000 rpm) from its toluene solution (0.6% (w/w)) and annealed at 170 °C in vacuum (ca. 0.3 Torr) for 60 h. The PMMA domains were removed by irradiation with UV light using a Novascan PSD-UVT UV-ozone system (ca. 20 mW/cm^2) under an Ar atmosphere and by subsequently immersing in AcOH.

The thickness of annealed CF-PS-*b*-PMMA films prior to the UV irradiation was measured using a J. A. Woollam alpha-SE spectroscopic ellipsometer. The ellipsometric thickness of an annealed film was used as the thickness of the nanoporous film obtained by the UV/AcOH treatment.

6.2.3. Surface Functionalization of CF-PS-b-PMMA-Derived Nanopores

The surface functionalization of CF-PS-*b*-PMMA-derived nanoporous films on gold was prepared according to procedures reported chapter 4 and 5. The nanopores film on gold were immersed in oxalyl chloride, and heated at 50 ºC for two hours. After excess oxalyl chloride was removed under vacuum, the films were soaked in a dichloromethane solution of a 16-hydroxy-1-oxohexadecylferrocene reactant (2 mM) at room temperature for 2 h. The samples were washed with dichloromethane and dried. The surface COOH density and surface functionalization yield were determined via a cation exchange method with Rhodamine 6G as shown in chapter 4 and 5.

6.2.4. Electrochemical Measurements

As shown in chapter 5, CV measurements in this chapter were also performed in a three-electrode cell containing an Ag/AgCl (3 M KCl) reference electrode and a Pt counter electrode using a CH Instruments model 618B electrochemical analyzer. A polymer-coated gold substrate (serving as the working electrode) was immobilized at the bottom of the cell. The diameter of the film area in contact with the solution, which was defined by an O-ring between the upper cell and the working electrode, was 0.8 cm. CV measurements were performed in aqueous solutions deoxygenated by bubbling and purging with Ar at room temperature (*ca*. 20 °C).

6.3. Results and Discussion

6.3.1. Effect of β-CD and AdOH Addition on Electron Hopping

In a study on the complexation of ferrocenecarboxylic acid by β-CD in aqueous solution, Evans and coworkers[25] reported that no direct oxidation of the inclusion ferrocene- β-CD complex is observed. And also Kaifer explained that the decreasing in the peak current in voltammograms is because the electron transfer reaction in the presence of the cyclodextrin will only take place on the free ferrocene after decomplexation from β-CD.[24] As we shown in previous chapter, cyclic voltammograms measured at ferrocene-functionalized nanoporous thin

films derived from PS-b-PMMA diblock copolymer in aqueous 0.1 M $NaBF_4$ exhibited faradic currents originating from redox-involved electron hopping through the ferrocene moieties covalently bonded onto the insulator surface. By adding β-cyclodextrin in aqueous solutions, the faradic currents dramatically decreased as shown in Figure 6.1.

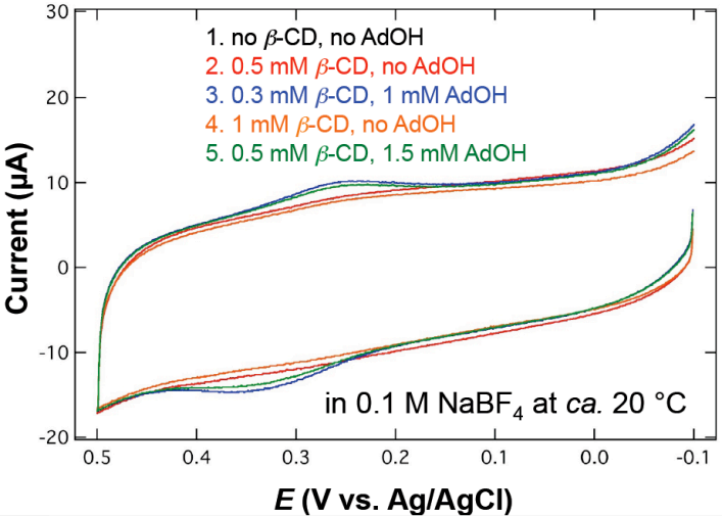

Figure 6.1 Cyclic voltammograms for the ferrocene moieties coated nanopores derived from 71K PS-b-PMMA thin films after β-cyclodextrin and 1-adamatanol treatment. Scan rate is 500 mV/s.

The reason of this phenomenon is the formation of 1:1 Fc·β-CD complexes between the β-CD in the solution and the immobilized ferrocenyl on the nanopore surface. By forming the complex, the electron transfer is inhibited because the complex is redox-inactive. Electron transfer only takes place immediately after dissociation of the interfacial inclusion complex. The current could be recovered by adding redox-inactive guest molecules of 1-adamantanol (1-AdOH) to the solution. The recovery of the faradiac current is because the difference of the complex fomation constant between Fc·β-CD and 1-AdOH·β-CD. According to the literature, the complex formation constant for Fc·β-CD that is around 2200 M^{-1} in solution is much smaller than the formation constant of 1-AdOH·β-CD (34100 M^{-1}). [26,27] When the 1-AdOH was added to the solution, Fc moities in the complex were replaced by 1-AdOH. The redox-inactived Fc by β-CD in the complex becomes redox-actived again.

6.3.2. Effect of β-CD Concentration on Electron Hopping

The strength of the interactions that promote the formation of 1:1 Fc·β-CD complexes between the β-CD in the solution and the immobilized ferrocenyl on the nanopore surface was

investigated by observing the adsorption of β-CD from aqueous solution as a function of β-CD concentration. By adding known amounts of β-CD in aqueous solutin, the resulting change in faradic current originating from electron hopping through the ferrocene moieties described in chapter 5 was observed as shown in Figure 6.2.

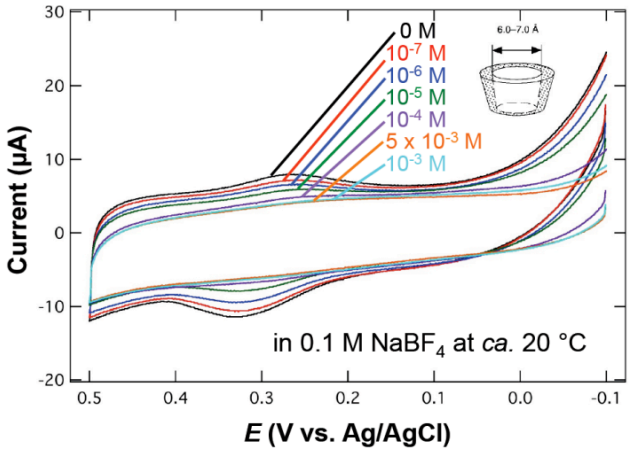

Figure 6.2 Cyclic voltammograms for the rerrocene moieties coated nanopores derived from 71K PS-b-PMMA thin films after cyclodextrin treatment of different contiontration at scan rate of 250 mV/s.

This observation is interpreted in terms of the following two reactions:

PS-linker-Fc·β-CD ↔ PS-linker-Fc + β-CD Eq 6.1

PS-linker-Fc ↔ PS-linker-Fc $^{+}$ + e^{+} Eq 6.2

This electrochemical oxidation mechanism of ferrocene derivatives in the presence of β-CD is widely accepted.[31] When the β-CD added to the solution, the Fc immobilized on the surface formed the 1:1 complex with β-CD. The complex formation reaction between β-CD and Fc is an equilibrium reaction. According to the CE mechanism (electron-transfer preceded by a chemical step) first reported by Evan's group, that electron transfer does not take place from the inclusion complex. The complex must first dissociate before the electrochemical oxidation reaction.[25, 26, 28-30] Thus, the faradiac current shown in the Figure 6.2 is coming from the free Fc from complex, as shown in Eq 6.1. By increasing the concentration of β-CD, the equilibrium of the reaction goes to the right, which indicates the decrease of the Fc moities coverage on the nanopore surface. As a result, the faradiac current decreases with increase of the β-CD concentration. Faradaic current reduction was observed even in the presence of 10^{-7} M β-CD. These small detection limits indicate that this recessed nanodis array electrodes functionalized

with redox moieties provide unique platforms for electroanalytical sensing based on redox-involved electron hopping and host-guest chemistry.

6.3.3. Effect of Pore Size on Electron Hopping

Table 6.1Apparent Diffusion Coefficients (D_{ap}) and Maximum Electron Propagation Distances (*h*) Measured at CF-PS-b-PMMA-Derived Nanoporous Films Modified with Ferrocene Derivatives after Cyclodextrin Treatment of Different Contiontration.

β-CD concentration (μM)	D_{ap} (x 10^{-13} cm^2/s)		*h (nm)*	
	57K[a]	71K[b]	57K[a]	71K[b]
0	3.34; 2.36	21.3 ± 5.7	3.4; 2.8	9.1 ± 0.8
0.0001	1.25; 1.02	17.7 ± 10.4	2.0; 1.8	7.5 ± 2.5
0.001	0.71; 0.39	12.2 ± 10.3	1.5; 1.1	5.8 ± 3.2
0.01	0.34; 0.32	7.07 ± 6.23	1.0; 1.0	4.6 ± 2.5
0.1	0.14; 0.28	4.12 ± 4.49	0.8; 0.9	2.8 ± 1.1

[a] The datas for ferrocene-modified 57K PS-b-PMMA nanoporous films obtained from 2 sets of CV data. [b] The average and standard deviation for ferrocene-modified 71K PS-b-PMMA nanoporous films obtained from 3 sets of CV data.

Apparent diffusion coefficients due to electron hopping through the anchored ferrocene moieties in the nanoporous films are calculated using the method shown in previous chapter. The values were shown in Table 6.1. With increase of the β-CD concentration, the apparent diffusion coefficiency decreased. According to the equation 5.3 in chapter 5, the apparent diffusion coefficient due to electron hopping is related to the surface coverage of the ferrocene redox moieties. Accroding to the CE mechanism mentioned previously, that electron transfer does not take place from the inclusion complex. By forming the complex, the number of redox active Fc on the surface decreases. The decrease of the apparent diffusion coefficient in Table 6.1 should be due to the decrease of redox active ferrocene surface. Next, the apparent diffusion coefficiencies were measured on nanoporous films derived from two types of PS-*b*-PMMA with different molecular weights (71K and 57K) (Table 6.1). Fifure 6.3 is showing that the CVs

obtained for gold-supported nanoporous films derived from 57K PS-*b*-PMMA diblock copolymer modified with $FcCO(CH_2)_{15}OH$.

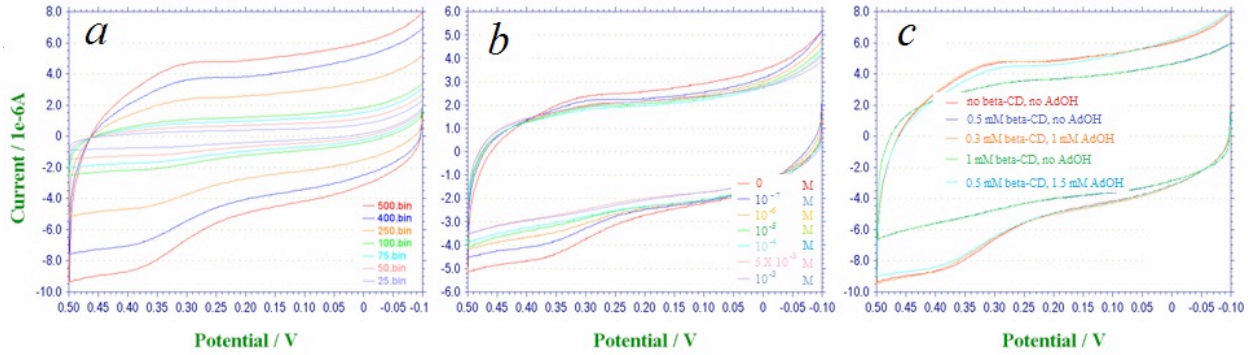

Figure 6.3 Cyclic voltammograms obtained for gold-supported nanoporous films derived from 57K PS-*b*-PMMA diblock copolymer modified with $FcCO(CH_2)_{15}OH$ a) at different scan rate; b) after cyclodextrin treatment of different contiontration at scan rate of 250 mV/s; c) after β-cyclodextrin and 1-adamatanol treatment. Scan rate is 500 mV/s. Measured in aqueous 0.1 M NaBF4 at room temperature (ca. 20 °C).

These two polymers offer nanoporous films with different pore diameters, and thus were used to investigate the effect of pore diameter on electron hopping efficiency.By decreasing the pore diameter from 24 nm (71K) to 19 nm (57K), the D_{ap} decrease about one order which is out of our expection. Theoritically, by decreasing the nanopore diameter, the anchored redox moieties become closer. According to chapter 5, the electron hopping efficiency will increase with decrease the distance between redox moieties. The reson of this phenomenon probably because the linker length we used in this research is around 2.4 nm, which is much smaller comparing to the pore diameter. The difference of the pore diameter is probably not large enough to show the effect on the electron hopping efficiency. The difference on the D_{ap} shown in Table 6.1 maybe because the redox moiety surface coverage on two type of pore surface are different ($(1.33 \pm 0.10)X10^{-10}$ mol/cm^2 on 71K and $(1.22 \pm 0.27)X10^{-10}$ mol/cm^2 on 57K).

6.3. Conclusion

This study showed electrochemical sensing with planar gold electrodes coated with thin insulator films comprising vertically-aligned cylindrical nanopores functionalized with ferrocene moieties. The nanoporous thin films were fabricated from a cylinder-forming polystyrene–poly(methylmethacrylate) diblock copolymer. Ferrocene moieties were covalently immobilized to the nanopore surface via esterification through surface -COOH groups. Cyclic

voltammograms measured at ferrocene-functionalized vertically-aligned cylindrical nanopores in aqueous 0.1 M $NaBF_4$ exhibited faradic currents originating from redox-involved electron hopping through the ferrocene moieties anchored onto the insulator surface. Interestingly, such faradic currents decreased with increasing the concentration of β-CD in aqueous solution. The current could be recovered by adding redox-inactive guest molecules of β-CD to the solution. These results indicate that RNEs functionalized with redox moieties provide unique platforms for electroanalytical sensing based on redox-involved electron hopping and host-guest chemistry.

References

1. Beer, P. D.; Hayes, E. J., *Coord. Chem. Rev.* **2003**, 240, 167 –189.
2. Willener, Y.; Joly, K. M.; Moody, C. J.; Tucker, J. H. R. *J. Org. Chem.* **2008**, 73, 1225-1233.
3. Oton, F.; T_rraga, A.; Espinosa, A.; Velasco, M. D.; Bautista, D.; Molina, P. *J. Org. Chem.* **2005**, 70, 6603-6608.
4. Caballero, A.; Garc_a, R.; Espinosa, A.; T_rraga, A.; Molina, P. J. Org. Chem. 2007, 72, 1161-1173.
5. Wilson, G. S.; Hu, Y. *Chem. Rev.* **2000**, 100, 2693-2704.
6. Majda, M. *Molecular Design of Electrode Surfaces*; Murray, R. W., Ed.; Wiley & Sons: New York, **1992**; pp 159-206.
7. Kaneko, M. *Prog. Polym. Sci.* **2001**, 26, 1101-1137.
8. Li, Y.; Maire, H. C.; Ito, T. *Langmuir* **2007**, 23, 12771-12776.
9. Maire, H. C.; Ibrahim, S.; Li, Y.; Ito, T. *Polymer* **2009**, 50, 2273-2280.
10. Y. Li, H. C. Maire and T. Ito, *Langmuir* **2007**, 23, 12771-12776.
11. S. Ibrahim and T. Ito, *Langmui,* **2010**, 26, 2119-2123.
12. Li, Y.; and Ito, T. *Langmuir* **2008**, 24, 8959-8963.
13. Li, F.; Diaz, R.; Ito, T. *RSC Adv*. **2011**, 1, 1732-1736.
14. Li, F.; Pandey, B.; Ito, T. *Langmuir* **2012**, 28, 16496-16500.
15. Yoon, H. C.; Hong, M.-Y.; Kim, H.-S. *Anal. Chem.* **2000**, 72, 4420-4427.
16. Yoon, H. C.; Hong, M.-Y.; Kim, H.-S. *Anal. Biochem.* **2000**, 282, 121-128.
17. Kim, E.; Kim, K.; Yang, H.; Kim, Y. T.; Kwak, J. *Anal. Chem.* **2003**, 75, 5665-5672.
18. Sato, S.; Nojima, T.; Kaki, M.; Takenaka, S. *Molecules* **2005**, 10, 693-707.
19. Yoon, H. C.; Lee, D.; Kim, H.-S.; *Anal. Chim. Acta*. **2002**, 456, 209-218.
20. Kwon, S. J.; Kim, E.; Yang, H.; Kwak, J. *Analyst* **2006**, 131, 402-406.
21. Kaifer, A. E.; Gomez-Kaifer, M. *Supramolecular Electrochemistry*, Wiley-VCH: Weinheim, **1999**.
22. Saenger, W. *Angew. Chem. Int. Ed. Engl*. **1980**, 19, 344-362
23. Bersier, P. M.; Bersier, J.; Klinggert, B. *Electroanalysis*, **1991**, 3, 443-448.
24. Rojas, M. T.; Koniger, R.; Stoddart, J. F.; Kaifer, A. E. *J. Am. Chem. Soc.*, **1995**, 117, 336–343.

25. Kaifer, A. E. *Acc. Chem. Res.* **1999**, 32, 62-71.
26. Matsue, T.; Evans, D. H.; Osa, T.; Kobayashi, N. *J. Am. Chem. Soc.*, **1985**, 107, 3411–3417.
27. Becuwe, M.; Landy, D.; Delattre, F.; Cazier, F.; Fourmentin, S. *Sensors* **2008**, 8, 3689-3705.
28. Isnin, R.; Salam, C.; Kaifer, A. E. *J. Org. Chem.***1991**, 56, 35
29. Mirzoian, A.; Kaifer, A. E. *Chem. Eur. J.* **1997**, 3, 1052.
30. Wang, Y.; Mendoza, S.; Kaifer, A. E. *Inorg. Chem.***1998**, 37, 317.
31. Cardona, C. M.; McCarley, T. D.; Kaifer, A. E. *J. Org. Chem.* **2000**, 65, 1857-1864.
32. Bustos, E.; Manriquez, J.; Juaristi, E.; Chapman, T. W.; and Godinez, L. A. *J. Braz. Chem. Soc.* **2008**, 19, 1010-1016.

Chapter 7 - General Conclusions

Polymer thin films have become an important part of research and industrial processes and are presenting anywhere in our everyday lives. Nevertheless, we are undoubtedly still making new discoveries about their structure, behavior and applications. In summary, this thesis explored through case studies of two major topics based on the science of polymer thin films including photopolymerized self-assembled monolayer and nanoporous thin film derived from diblock copolymer.

The first project related to polymer thin film investigated the photopolymerization behavior of diacetylenic functional group in self-assembled monolayers on GaN semiconductior surface. As a good alternative of silicon, group III nitrides including GaN have been employed as components of chemical and biological sensors for gas and solution samples. Due to limitation number of chemical species of GaN sensors resulting from the low chemical selectivity of the material, the surface modification of the GaN with self-assembled monolayer having chemical recognition functional groups will be applied. First, we checked the formation of self assembled monolayers of five primaryly substitued hydrocarbons on GaN substrates. According to the results, the ODPA with phosphonic acid group have highest affinity to the UV/O_3 treatment GaN surface comparing to other hydrocarbons. Well-packed monolayer can be formed with ODPA on UV/O_3 treatment GaN surface. To improve the stabiliy, alkylphosphonate self assembled monolayers having diacetylenic group have been formed on AlGaN/GaN substrates. The UV-initiated photopolymerization of diacetylenic alkylphosphonate SAMs have reduced desorption in aqueous solution. And also, the photopolymerization efficiency of the SAMs is affected by the position of polymerization functional group in the alkyl chain: SAMs containing diacetylenic moieties located farther from terminal phosphonate groups exhibited more efficient photopolymerization.

Chapter 4 to 6 introduced the functionalization, electrochemisry and sensing application of nanoporous thin film derived from diblock copolymer. As we know the diblock copolymer with immiscible blocks can microphase separate as a function of composition into a variety of morphologies, including spheres, cylinders, bicontinuous gyroids, and lamellae. In this research, PS-b-PMMA diblock copolymer was used. The polystyrene-based films comprising cylindrical nanopores oriented perpendicular to an underlying gold electrode was fabricated from a cylinder-

forming polystyrene-poly (methylmethacrylate) diblock copolymer (CF-PS-*b*-PMMA). The surface of the nanopores has been proved that it is covered with COOH group, which can be subsequently modified via esterification of surface COOH groups with ferrocene derivatives with different alkyl linker lengths. Using ion-exchange approach, we quantitatively measured the surface modification efficiency on these nanoporous films with different nanopore diameters. This quantitative information is a base parameter for the project in chapter 5.

In chapter 5, the chemical modification of the nanopores with ferrocene redox moieties was described. These modified nanopores directly contacted to the underlying electrode with no leakage, permitting for direct electrochemical measurements of electron propagation from/toward the redox sites anchored onto the insulator-based nanopore surface. Average spacing between adjacent ferrocene moieties (ca. 1.2 nm) that obtained in the chapter 4 was larger than the size of ferrocene (ca. 0.66 nm in diameter). In this chapter, we studied the electron hopping efficiency through these anchored redox moities affected by the linker length. Here, the redox moities are covalently bonded on the nanopore surface, so no physical diffusion of the redox moities involved in the electron hopping process. The electron hopping could take place only when adjacent ferrocene moieties could approach closely enough for electron self-exchange reaction. The linker length defined the physical displacement range of surface-anchored ferrocene moieties, leading to the control of electron propagation efficiency.

In chapter 6, we showed another approach to control the electron propagation efficiency by controlling the number of redox sites resulting from the interfacial formation of 1:1 complexs of ferrocene and β-cyclodextrin. Here, the cyclic voltammograms measured at ferrocene-functionalized nanoporous block copolymer thin films in aqueous 0.1 M $NaBF_4$ exhibited faradic currents originating from redox-involved electron hopping through the ferrocene moieties anchored onto the insulator surface. Interestingly, such faradic currents decreased with increasing the concentration of beta-cyclodextrin (b-CD) in aqueous solution. The current could be recovered by adding redox-inactive guest molecules of adamantanol to the solution. These results indicate that the nanoporous diblock copolymer thin film functionalized with redox moieties provide unique platforms for electroanalytical sensing based on redox-involved electron hopping and host-guest chemistry.

Appendix A - Spectrum

Spectrum for Diacetylenic Alkylphosphonic Acids and Their Intermidiates

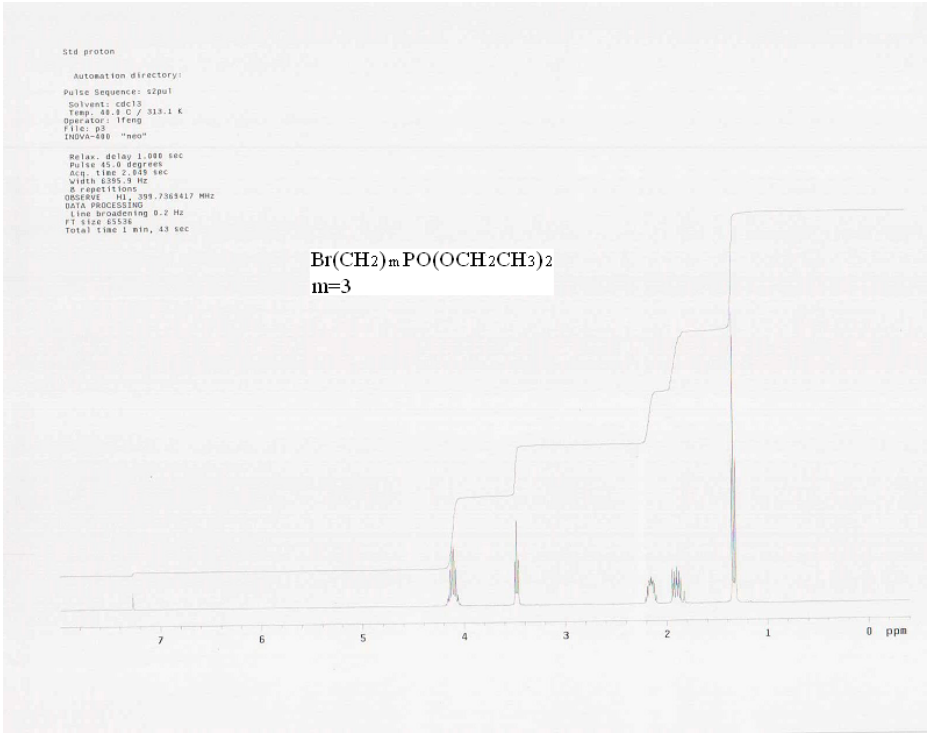

Figure A.1 ^{1}H-NMR spectrum of *Diethyl (w-bromoalkyl)phosphonates* 2a (m = 3) in $CDCl_3$

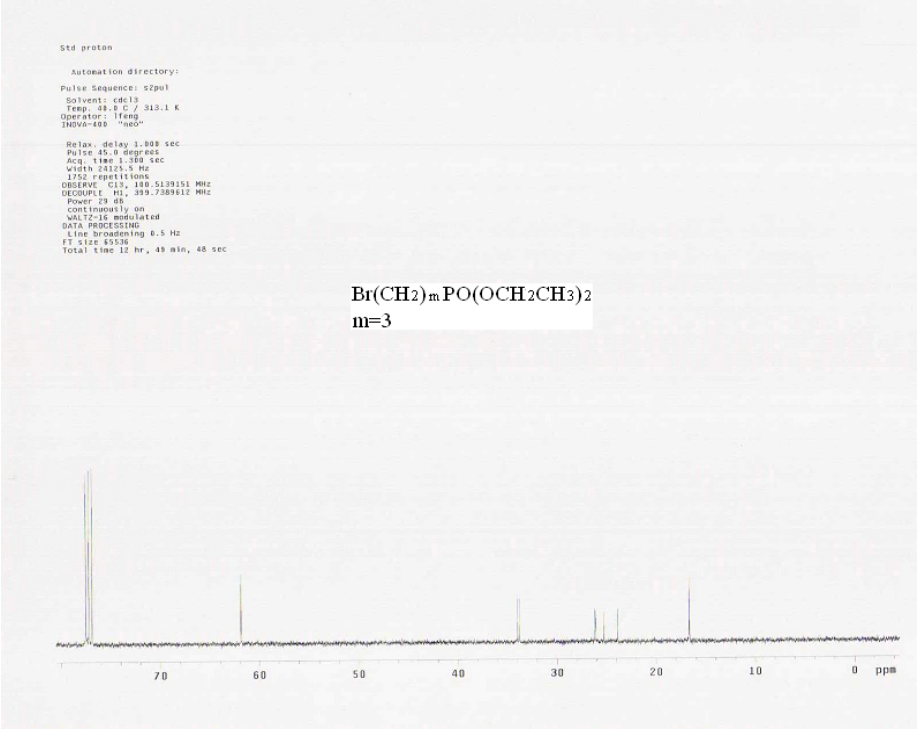

Figure A.2 ^{13}C-NMR spectrum of *Diethyl (ω-bromoalkyl)phosphonates* 2a (m = 3) in $CDCl_3$

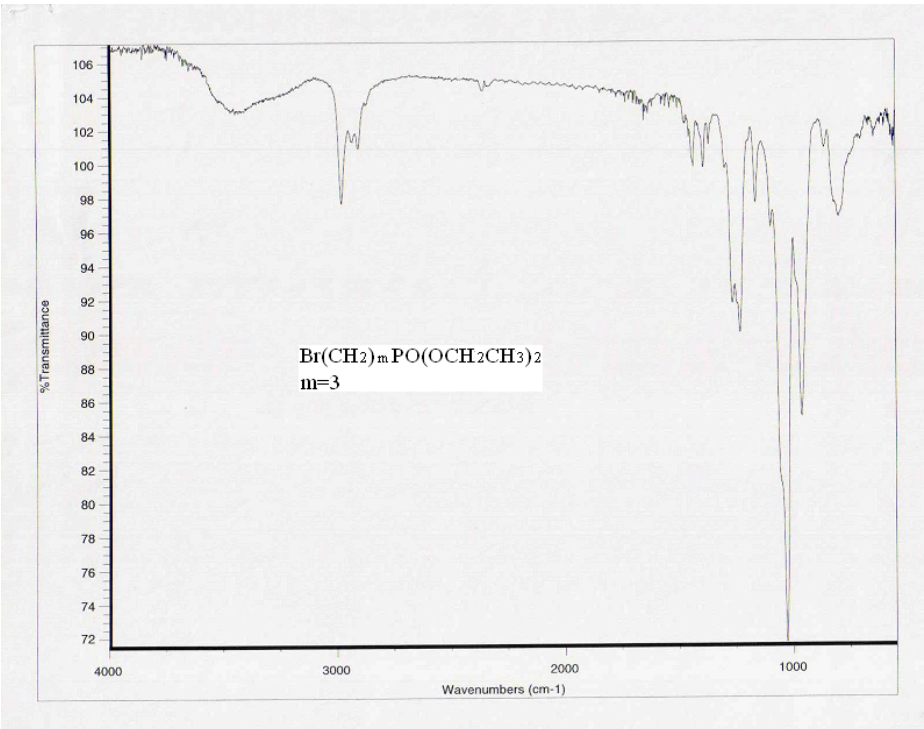

Figure A.3 IR spectrum of *Diethyl (ω-bromoalkyl)phosphonates* 2a (m = 3)

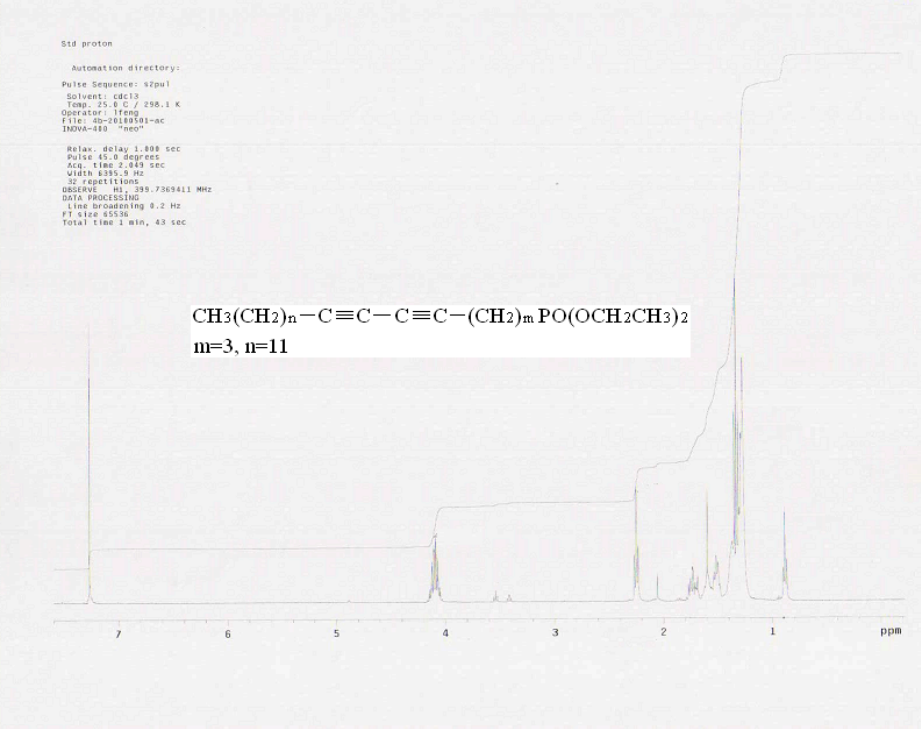

Figure A.4 ^{1}H-NMR spectrum of *Diethyl Alkadiyn-1-phosphonates* 4a (m = 3, n =11) in $CDCl_3$

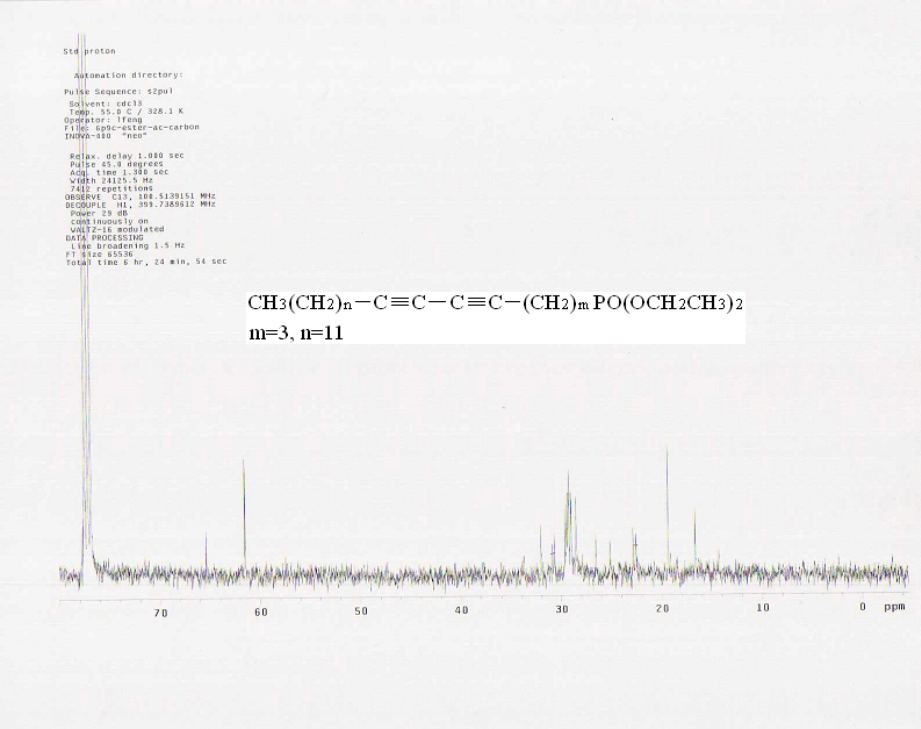

Figure A.5 ^{13}C-NMR of spectrum of *Diethyl Alkadiyn-1-phosphonates* 4a (m = 3, n =11) in $CDCl_3$

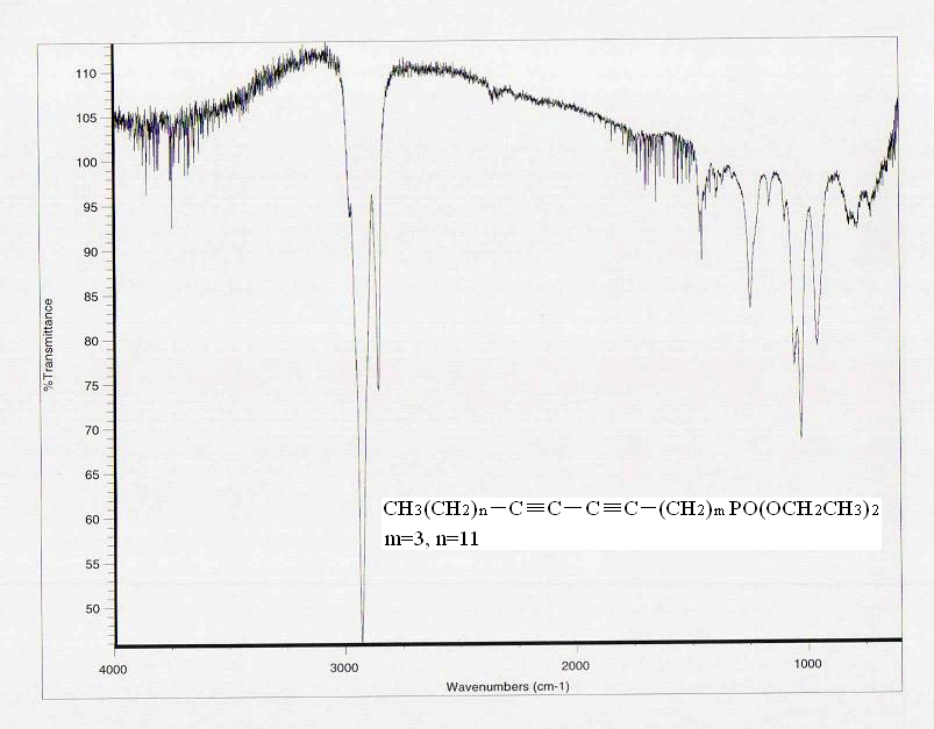

Figure A.6 IR spectrum of *Diethyl Alkadiyn-1-phosphonates* 4a (m = 3, n =11)

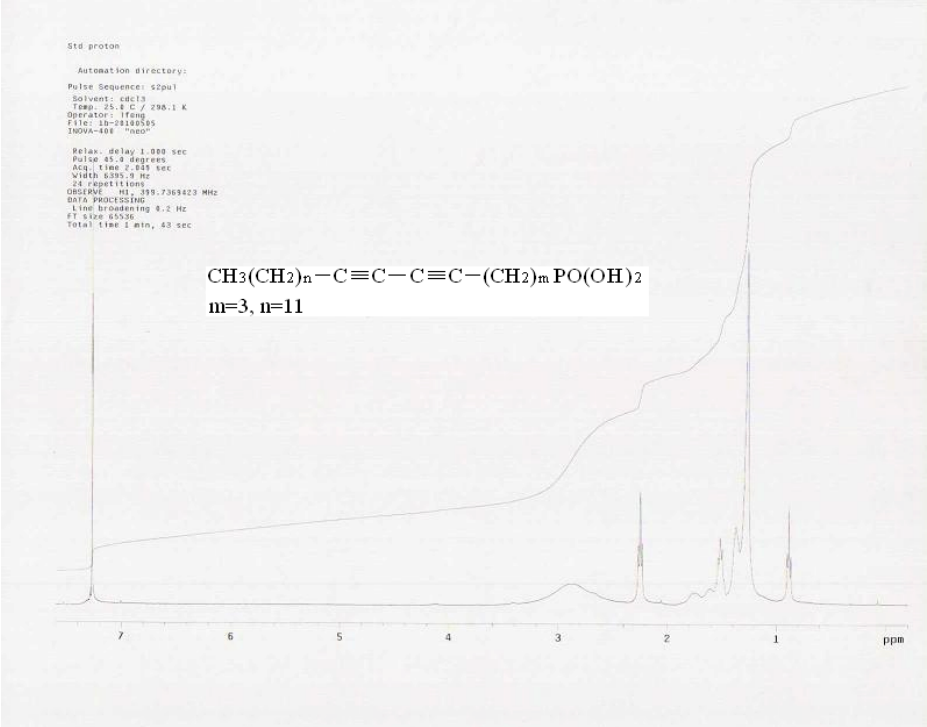

Figure A.7 ^{1}H-NMR spectrum of *Diacetylenic Alkylphosphonic Acids* 1a (m = 3, n =11) in $CDCl_3$

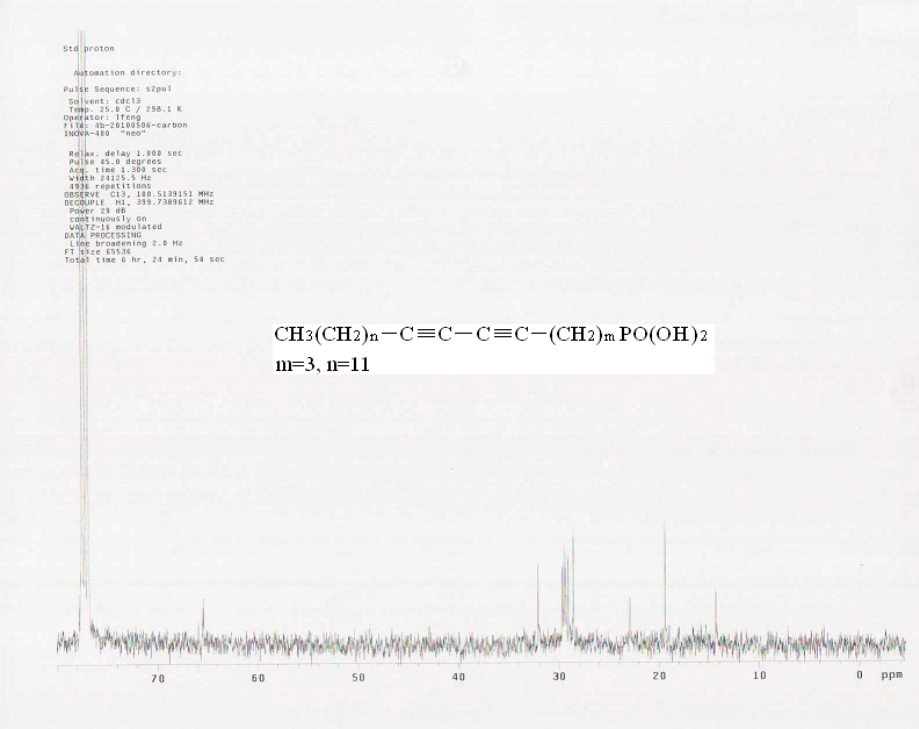

Figure A.8 ^{13}C-NMR spectrum of *Diacetylenic Alkylphosphonic Acids* 1a (m = 3, n =11) in $CDCl_3$

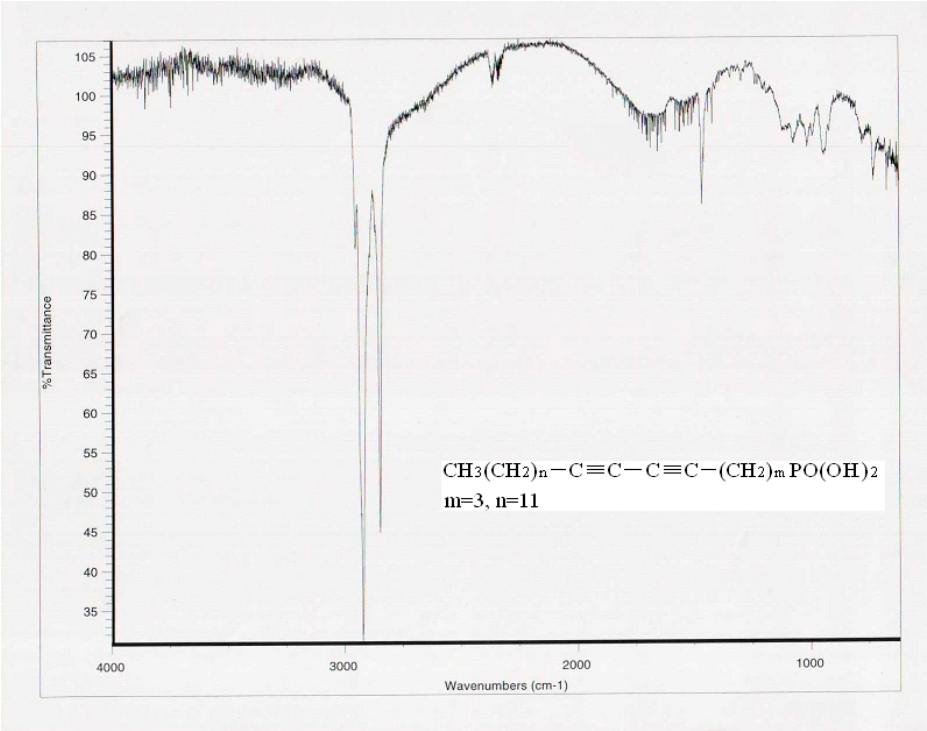

Figure A.9 IR spectrum of *Diacetylenic Alkylphosphonic Acids* 1a (m = 3, n =11)

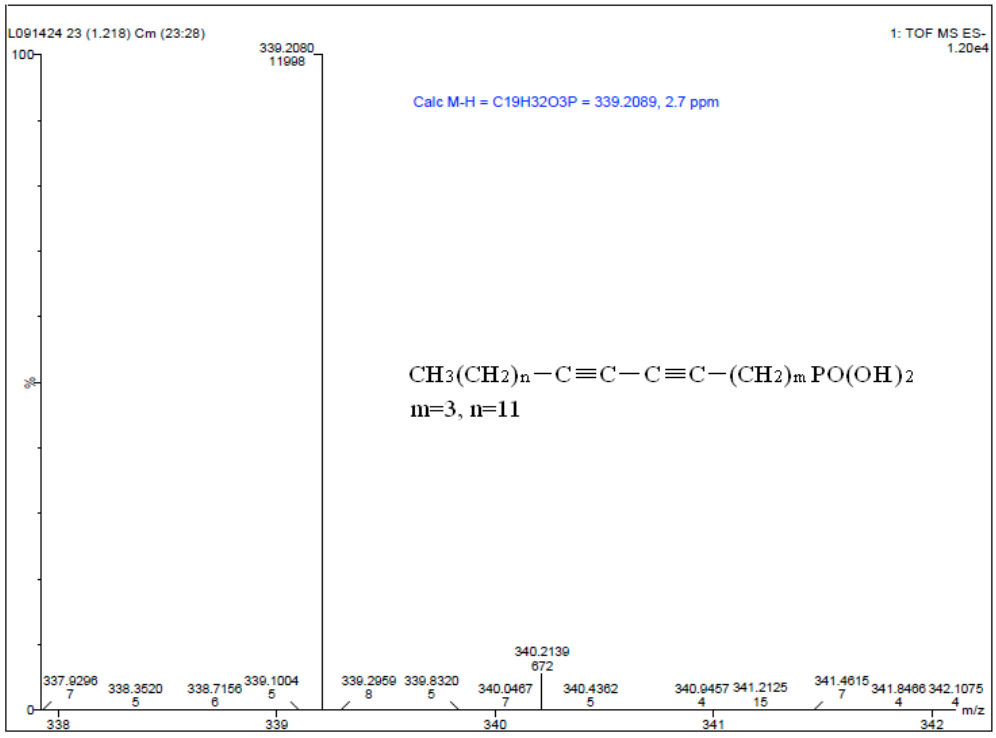

Figure A.10 Mass spectrum of *Diacetylenic Alkylphosphonic Acids* 1a (m = 3, n =11)

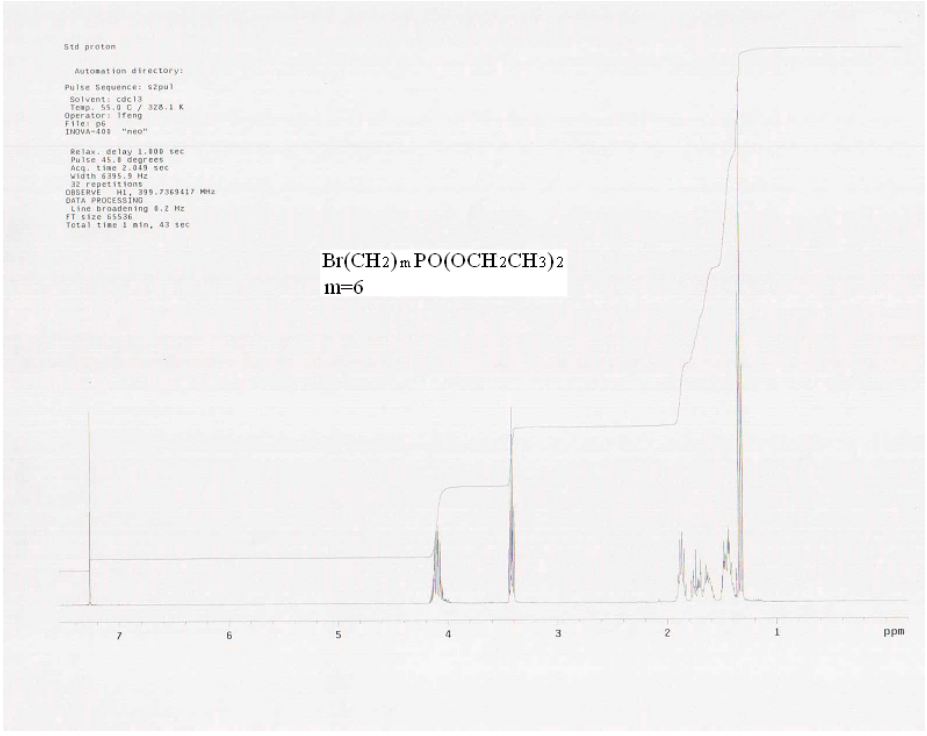

Figure A.11 ^{1}H-NMR spectrum of *Diethyl (w-bromoalkyl)phosphonates* 2b (m = 6) in $CDCl_3$

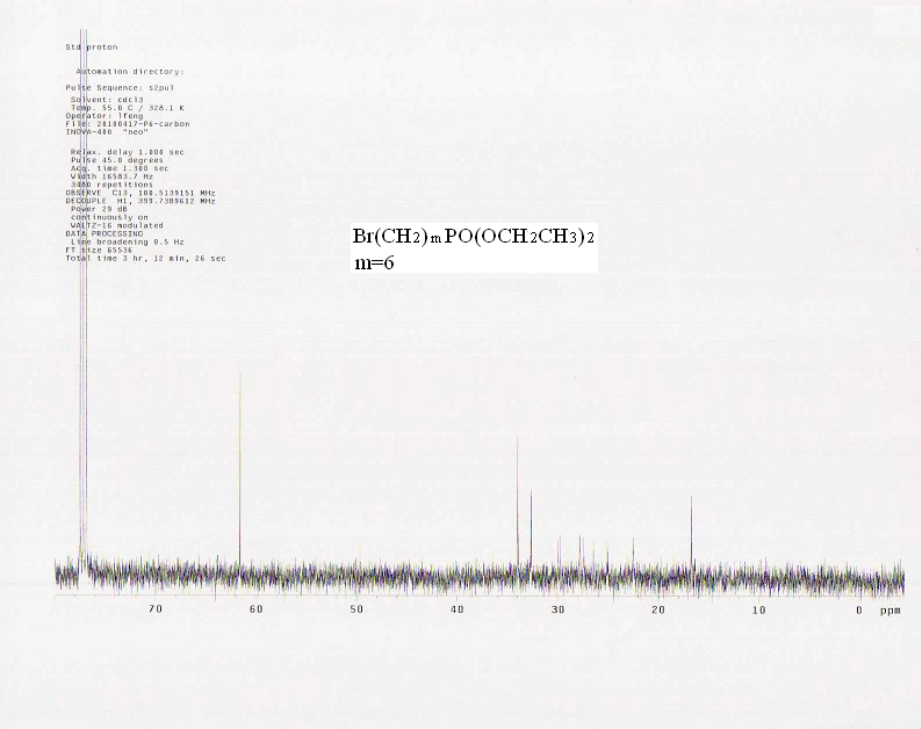

Figure A.12 ^{13}C-NMR spectrum of *Diethyl (w-bromoalkyl)phosphonates* 2b (m = 6) in $CDCl_3$

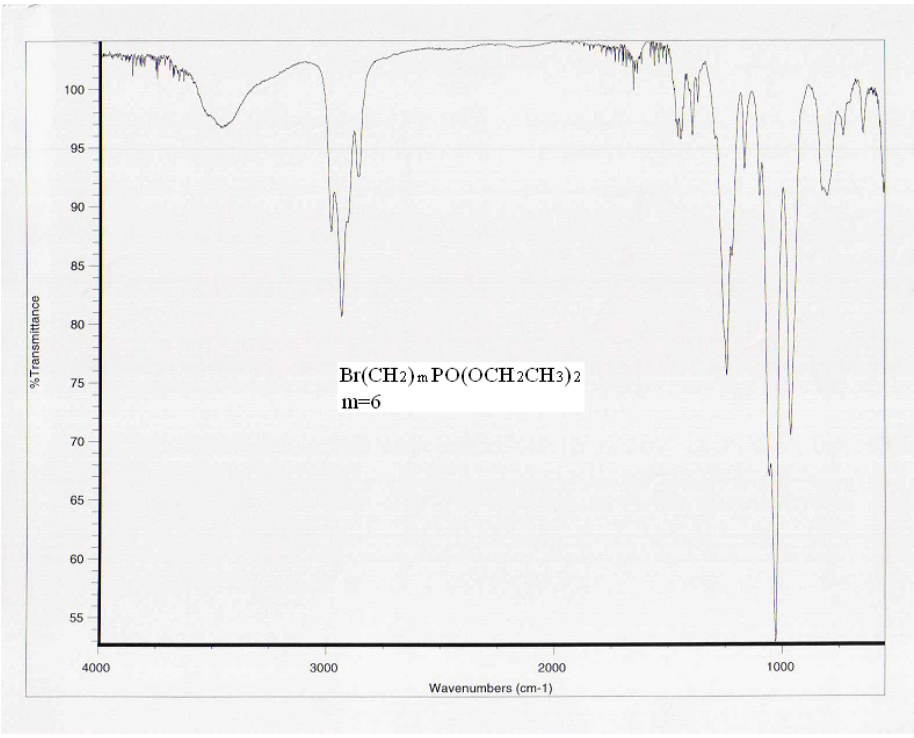

Figure A.13 IR spectrum of *Diethyl (w-bromoalkyl)phosphonates* 2b (m = 6)

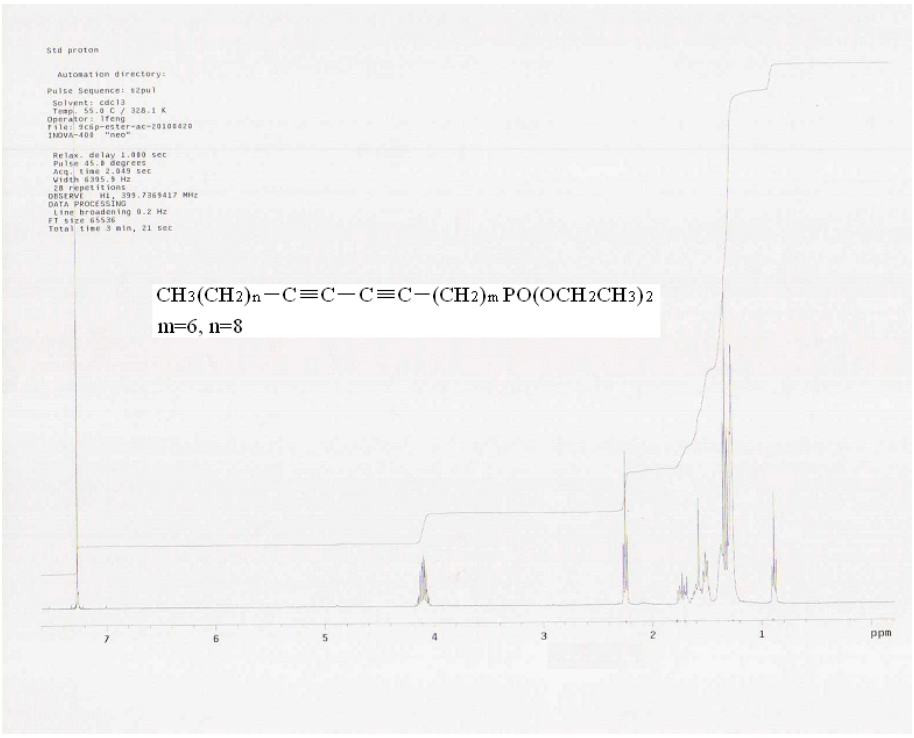

Figure A.14 ^{1}H-NMR spectrum of *Diethyl Alkadiyn-1-phosphonates* 4b (m = 6, n =8) in $CDCl_3$

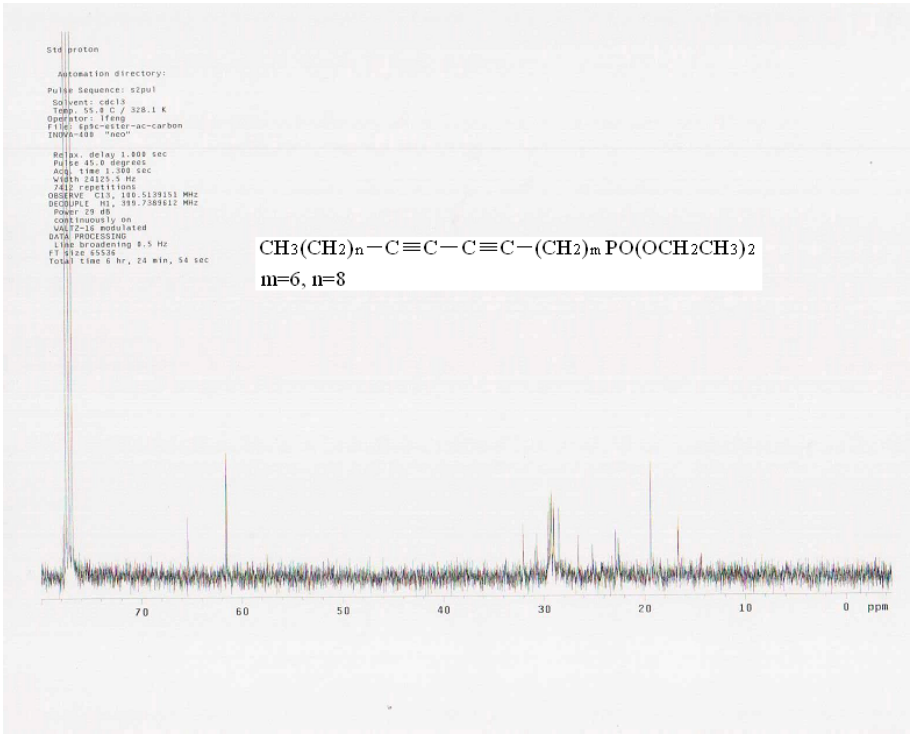

Figure A.15 ^{13}C-NMR spectrum of *Diethyl Alkadiyn-1-phosphonates* 4b (m = 6, n =8) in $CDCl_3$

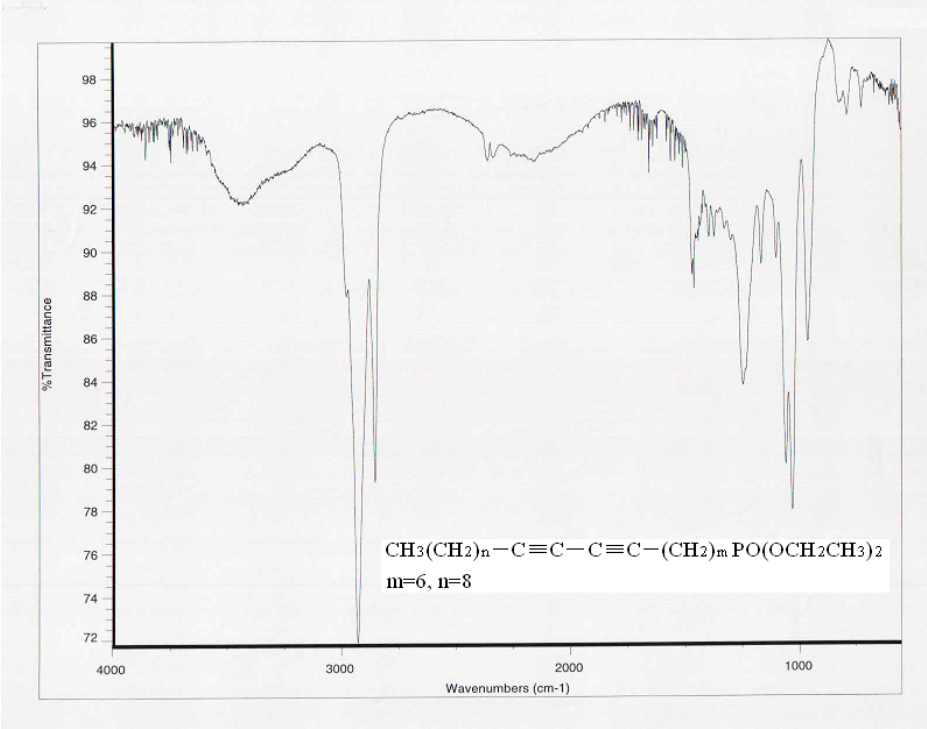

Figure A. 16 IR spectrum of *Diethyl Alkadiyn-1-phosphonates* 4b (m = 6, n =8)

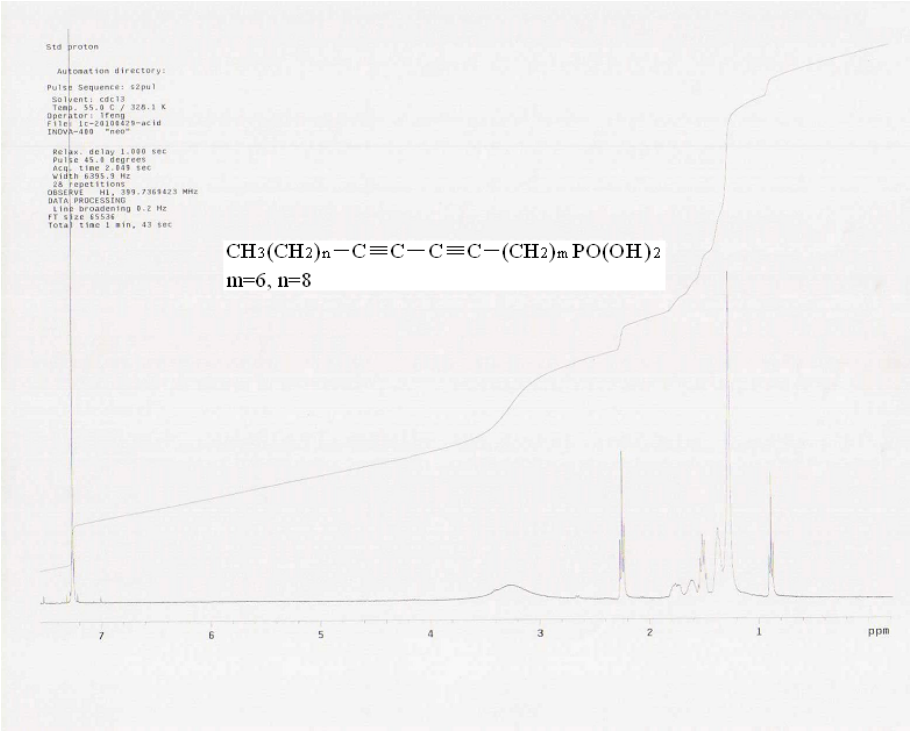

Figure A.17 ^{1}H-NMR spectrum of *Diacetylenic Alkylphosphonic Acids* 1b (m = 6, n =8) in $CDCl_3$

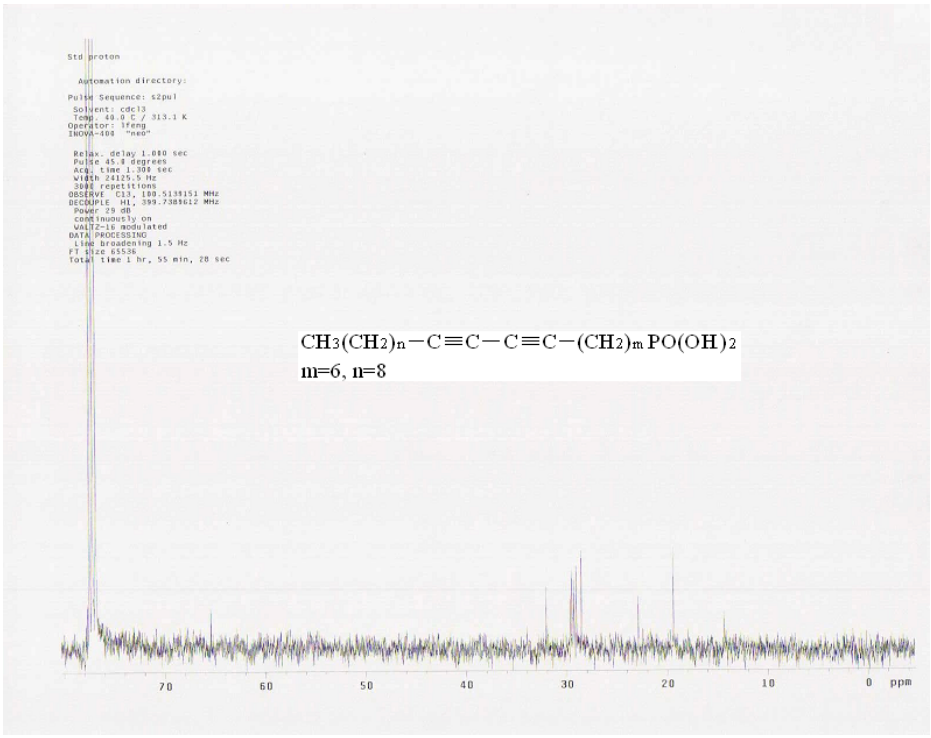

Figure A.18 ^{13}C-NMR spectrum of *Diacetylenic Alkylphosphonic Acids* 1b (m = 6, n =8) in $CDCl_3$

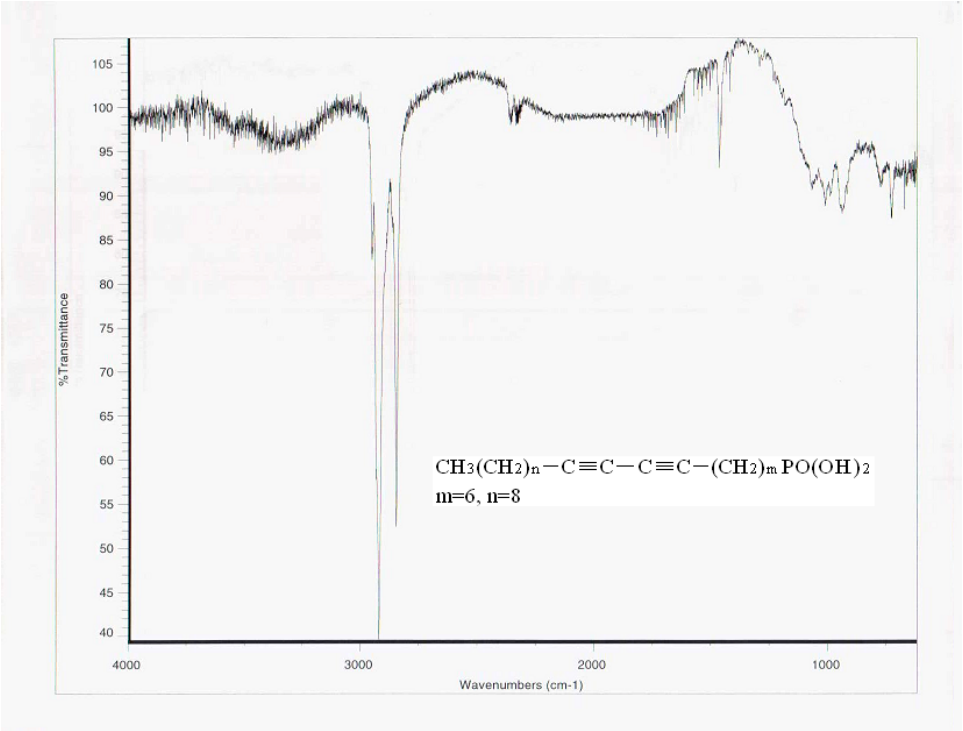

Figure A.19 IR spectrum of *Diacetylenic Alkylphosphonic Acids* 1b (m = 6, n =8)

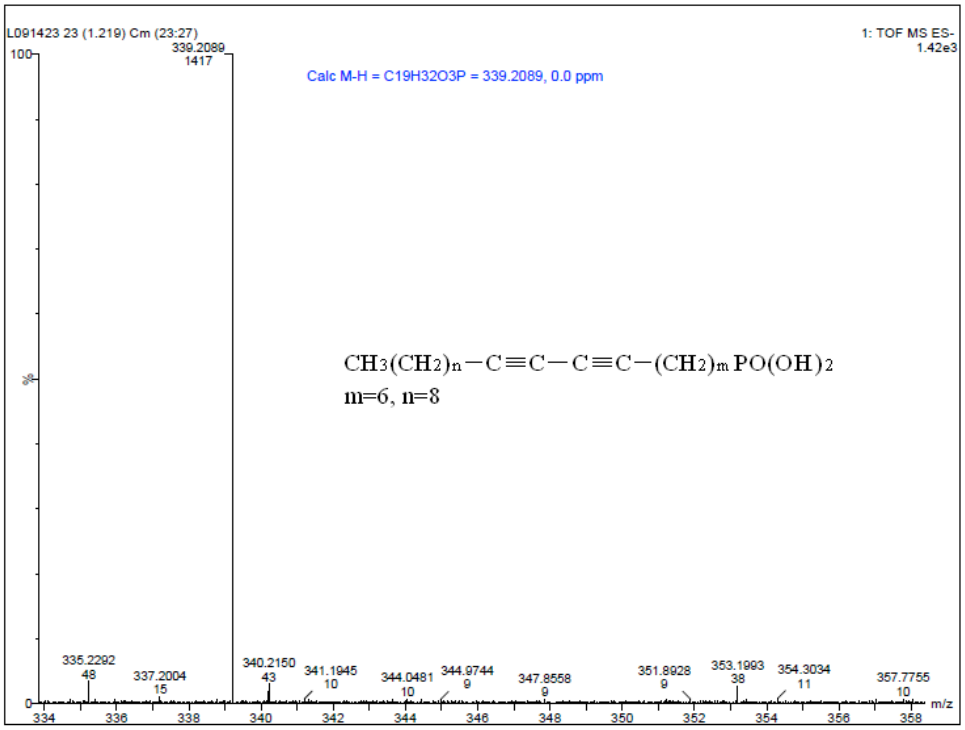

Figure A. 20 Mass spectrum of *Diacetylenic Alkylphosphonic Acids* 1b (m = 6, n =8)

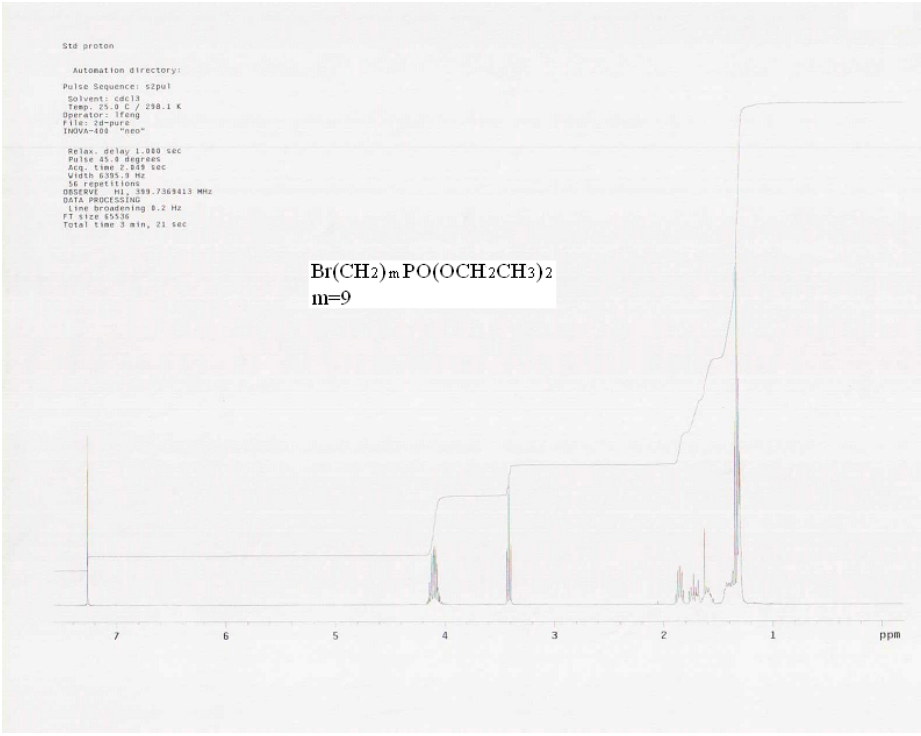

Figure A.21 ^{1}H-NMR spectrum of *Diethyl (w-bromoalkyl)phosphonates* 2c (m = 9) in $CDCl_3$

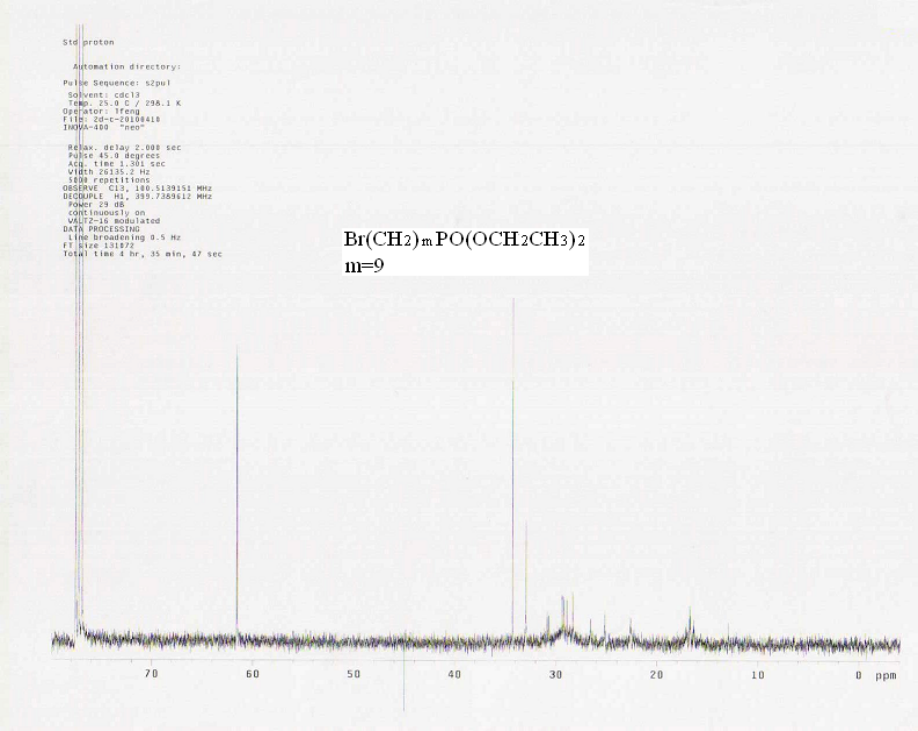

Figure A.22 ^{13}C-NMR spectrum of *Diethyl (w-bromoalkyl)phosphonates* 2c (m = 9) in $CDCl_3$

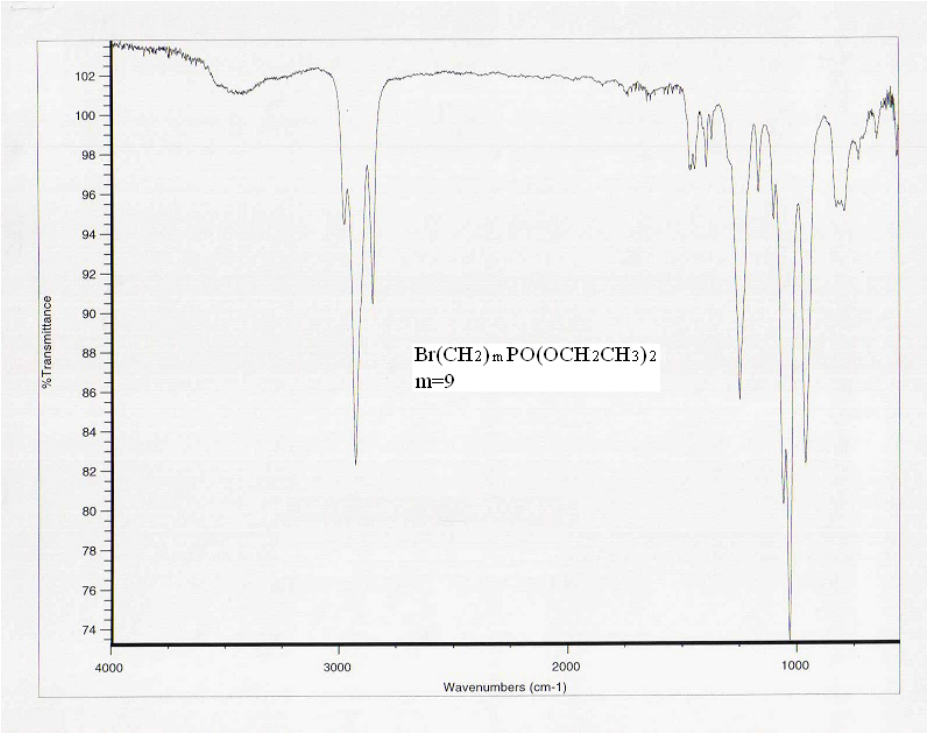

Figure A.23 IR spectrum of *Diethyl (w-bromoalkyl)phosphonates* 2c (m = 9)

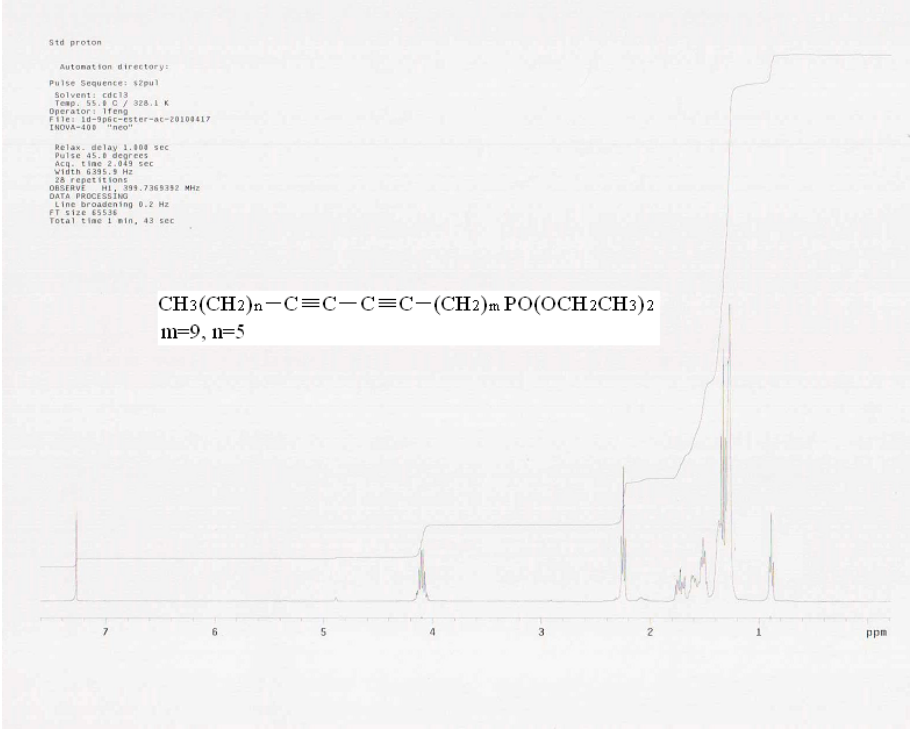

Figure A.24 ^{1}H-NMR spectrum of *Diethyl Alkadiyn-1-phosphonates* 4c (m = 9, n =5) in $CDCl_3$

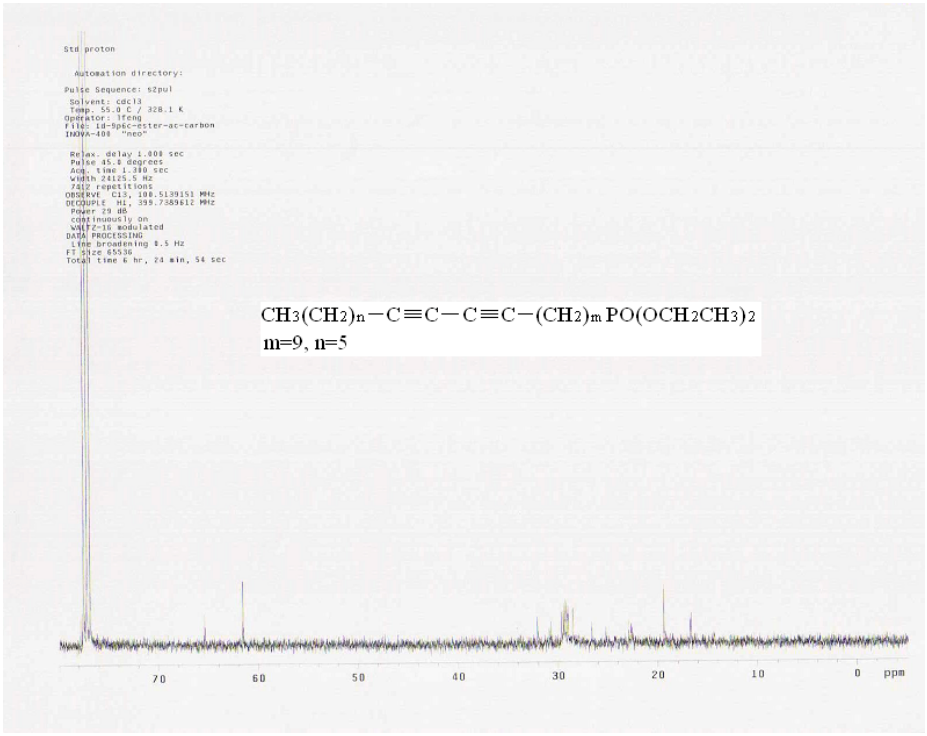

Figure A.25 ^{13}C-NMR spectrum of *Diethyl Alkadiyn-1-phosphonates* 4c (m = 9, n =5) in $CDCl_3$

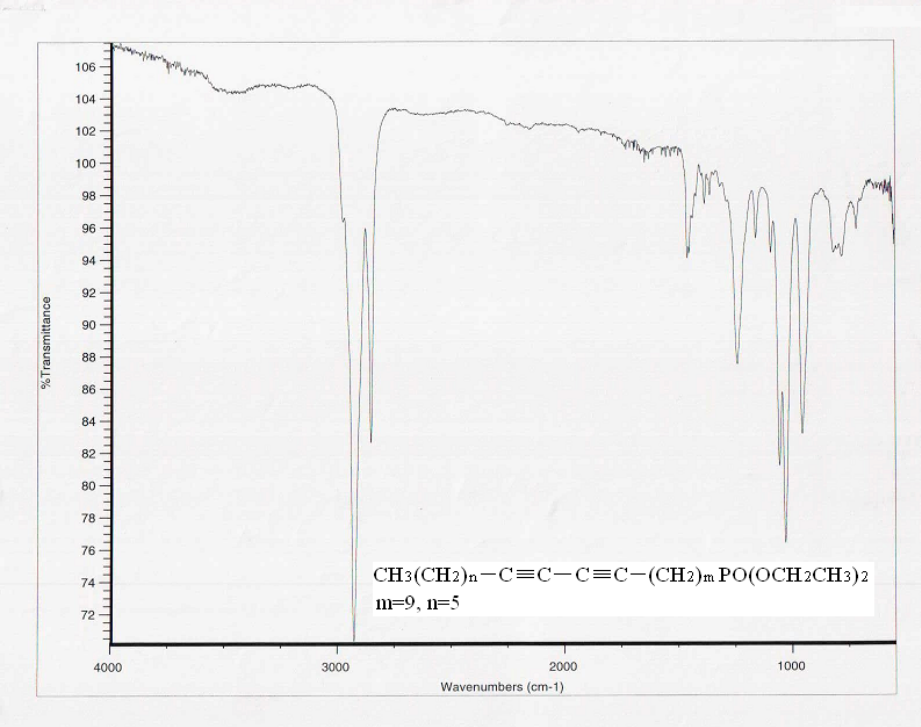

Figure A.26 IR spectrum of *Diethyl Alkadiyn-1-phosphonates* 4c (m = 9, n =5)

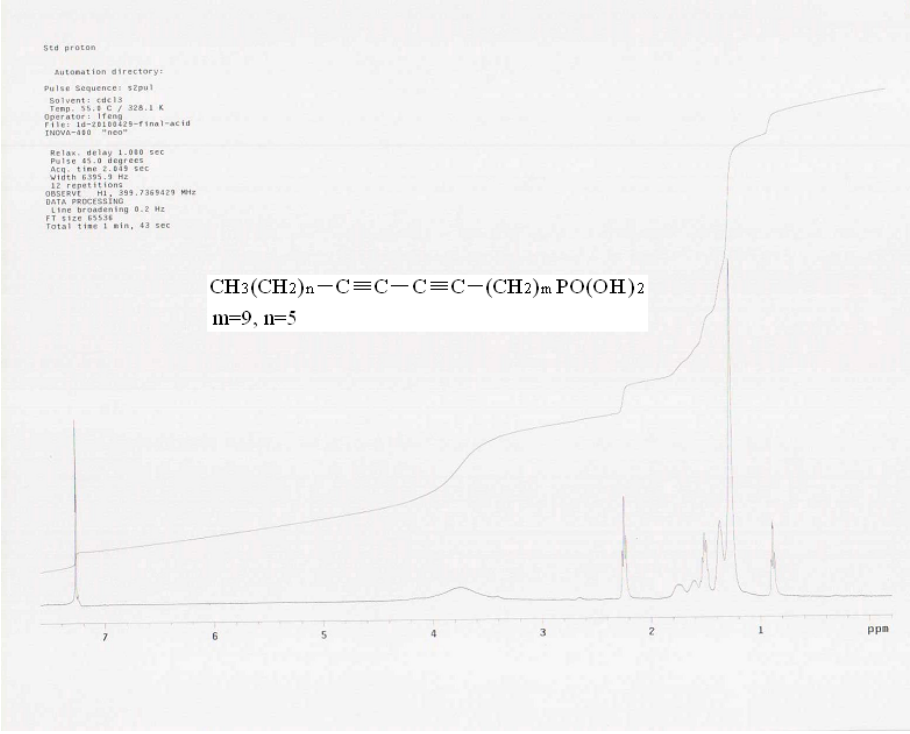

Figure A.27 ^{1}H-NMR spectrum of *Diacetylenic Alkylphosphonic Acids* 1c (m = 9, n =5) in $CDCl_3$

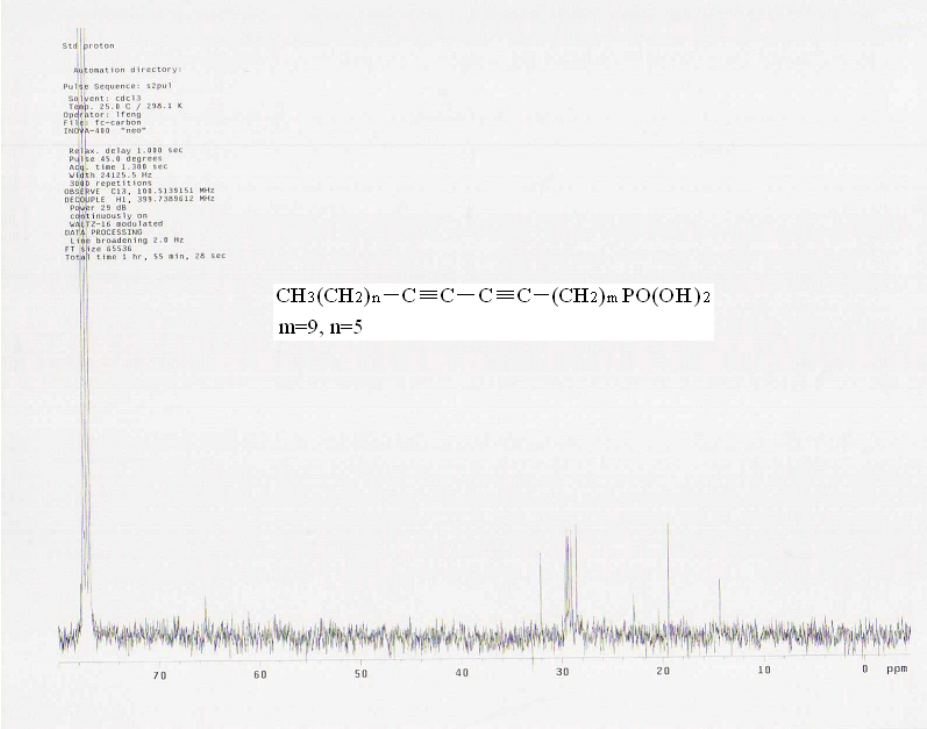

Figure A.28 ^{13}C-NMR spectrum of *Diacetylenic Alkylphosphonic Acids* 1c (m = 9, n =5) in $CDCl_3$

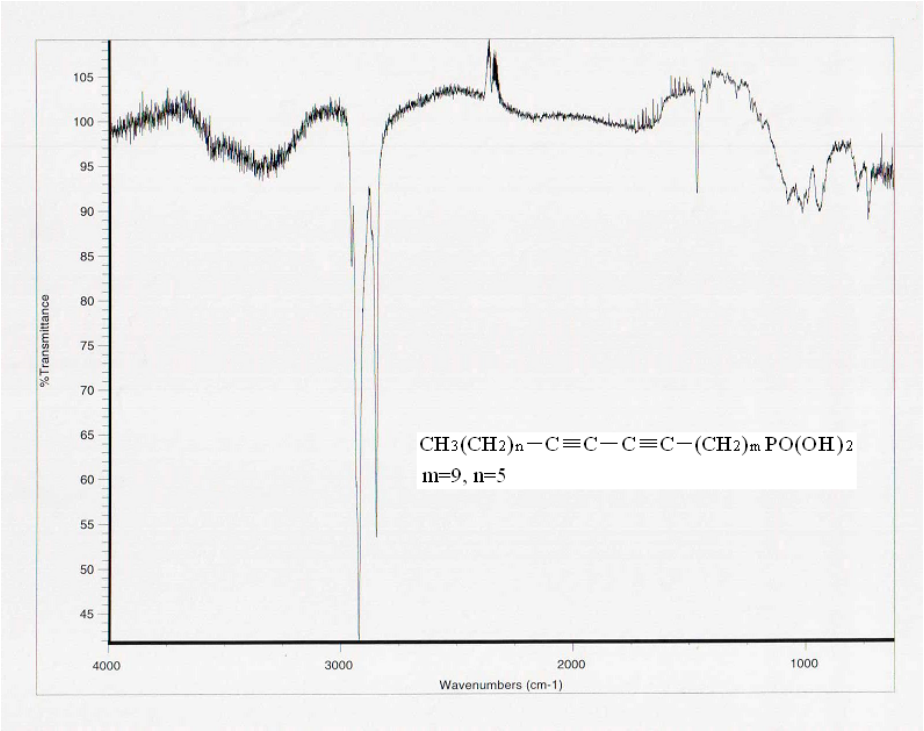

Figure A.29 IR spectrum of *Diacetylenic Alkylphosphonic Acids* 1c (m = 9, n =5)

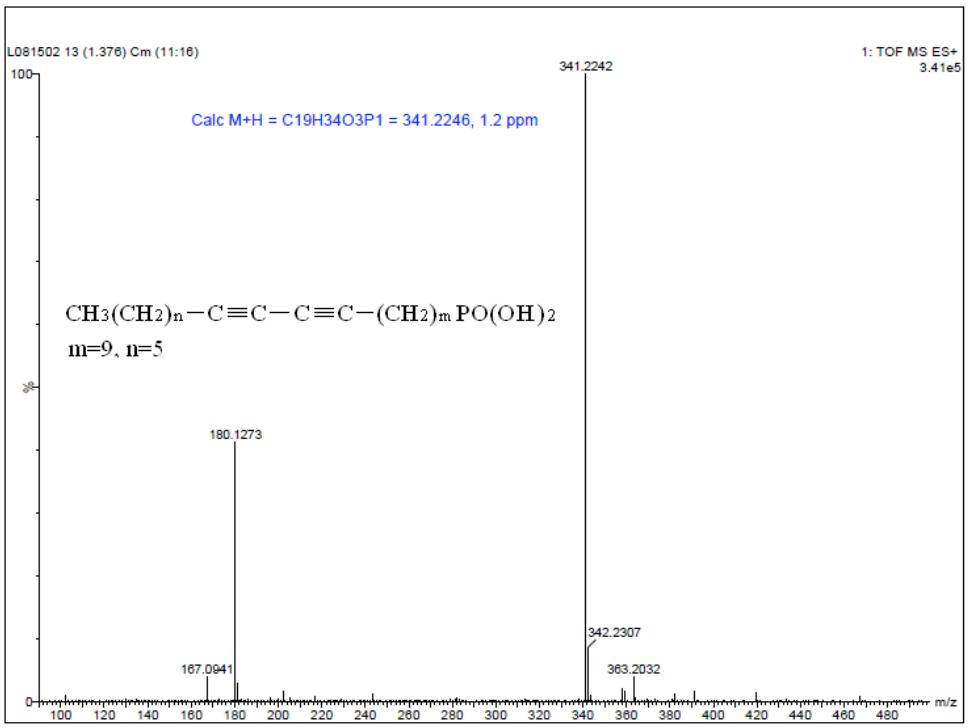

Figure A.30 Mass spectrum of *Diacetylenic Alkylphosphonic Acids* 1c (m = 9, n =5)

Spectrum for Ferrocene Moieties and Their Intermidiates

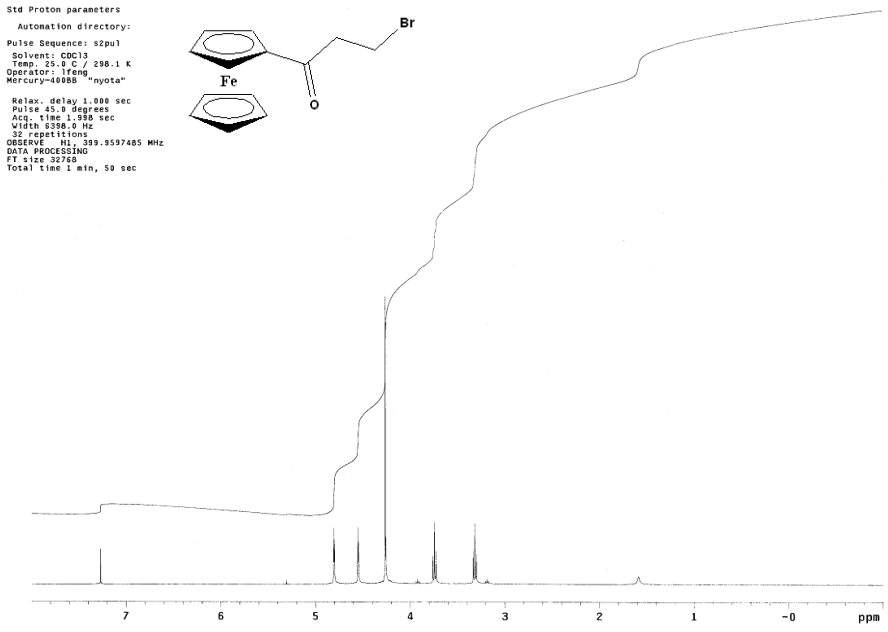

Figure A.31 ^{1}H-NMR Spectrum of *3-Bromo-1-Oxopropylferrocene*

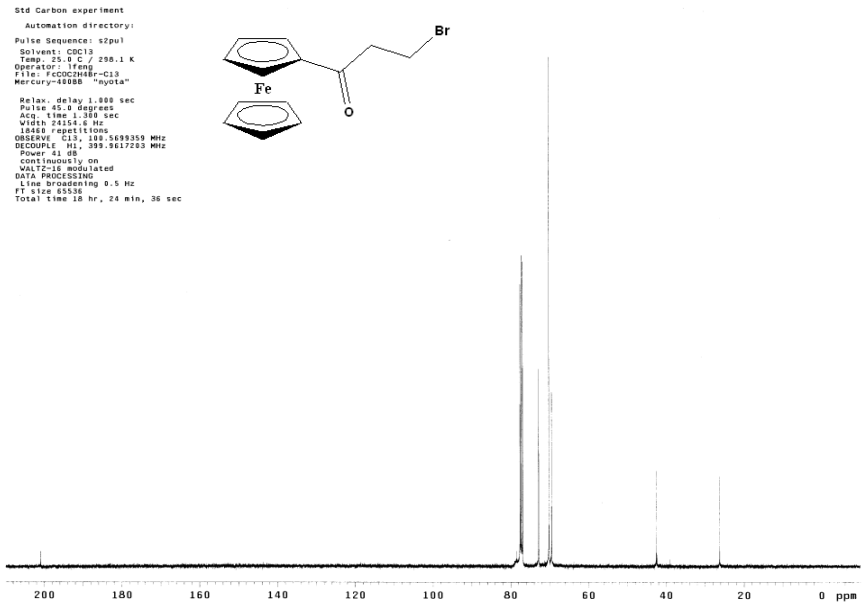

Figure A.32 ^{13}C-NMR Spectrum of *3-Bromo-1-Oxopropylferrocene*

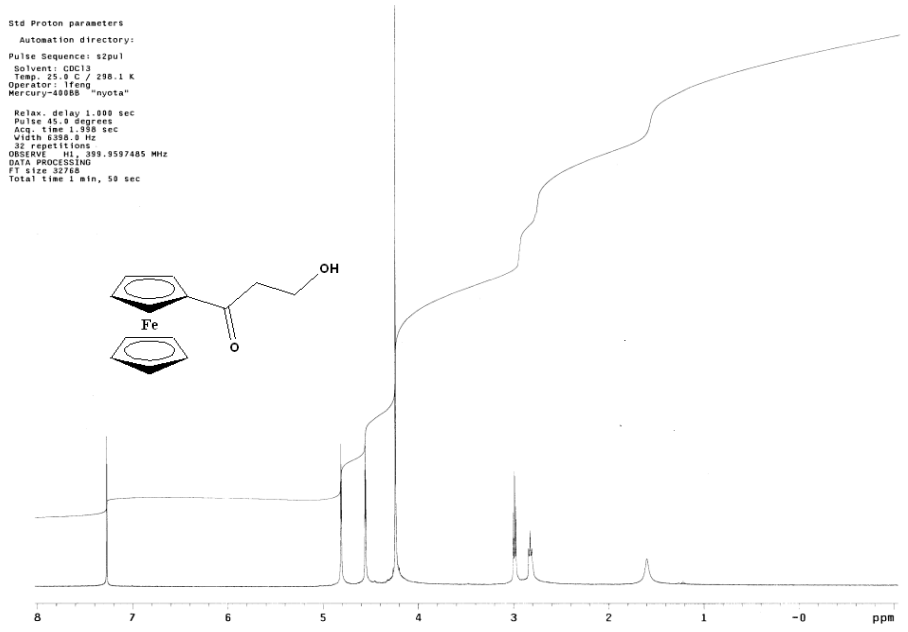

Figure A.33 ^{1}H-NMR Spectrum of *3-Hydroxy-1-Oxopropylferrocene*

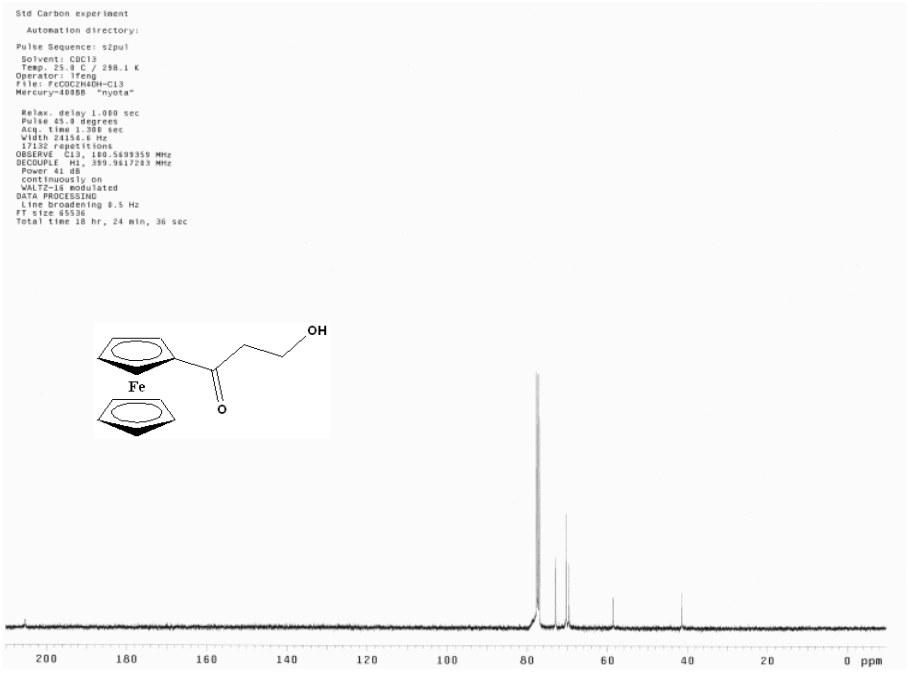

Figure A.34 ^{13}C-NMR Spectrum of *3-Hydroxy-1-Oxopropylferrocene*

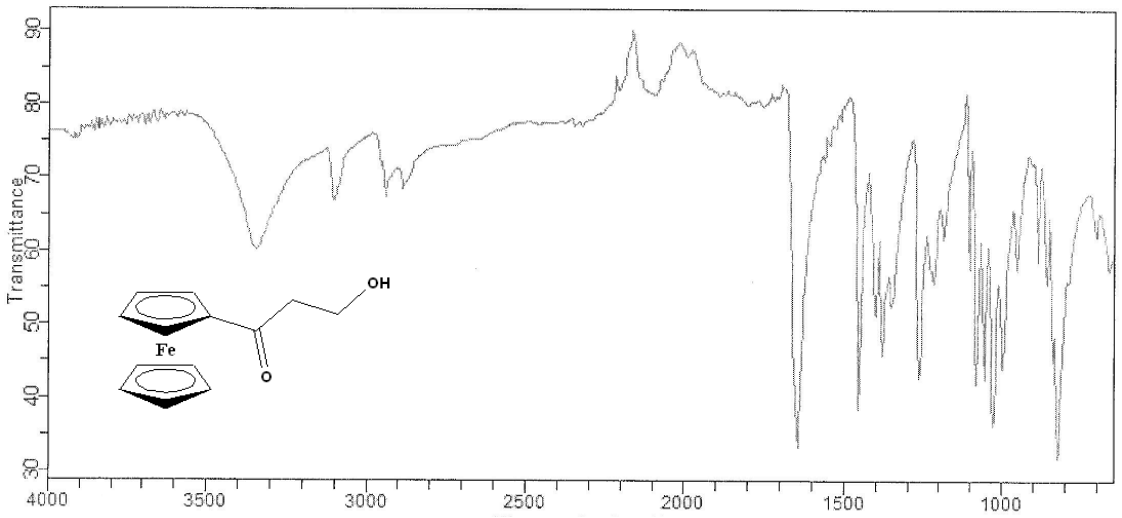

Figure A.35 FTIR-ATR Spectrum of *3-Hydroxy-1-Oxopropylferrocene*

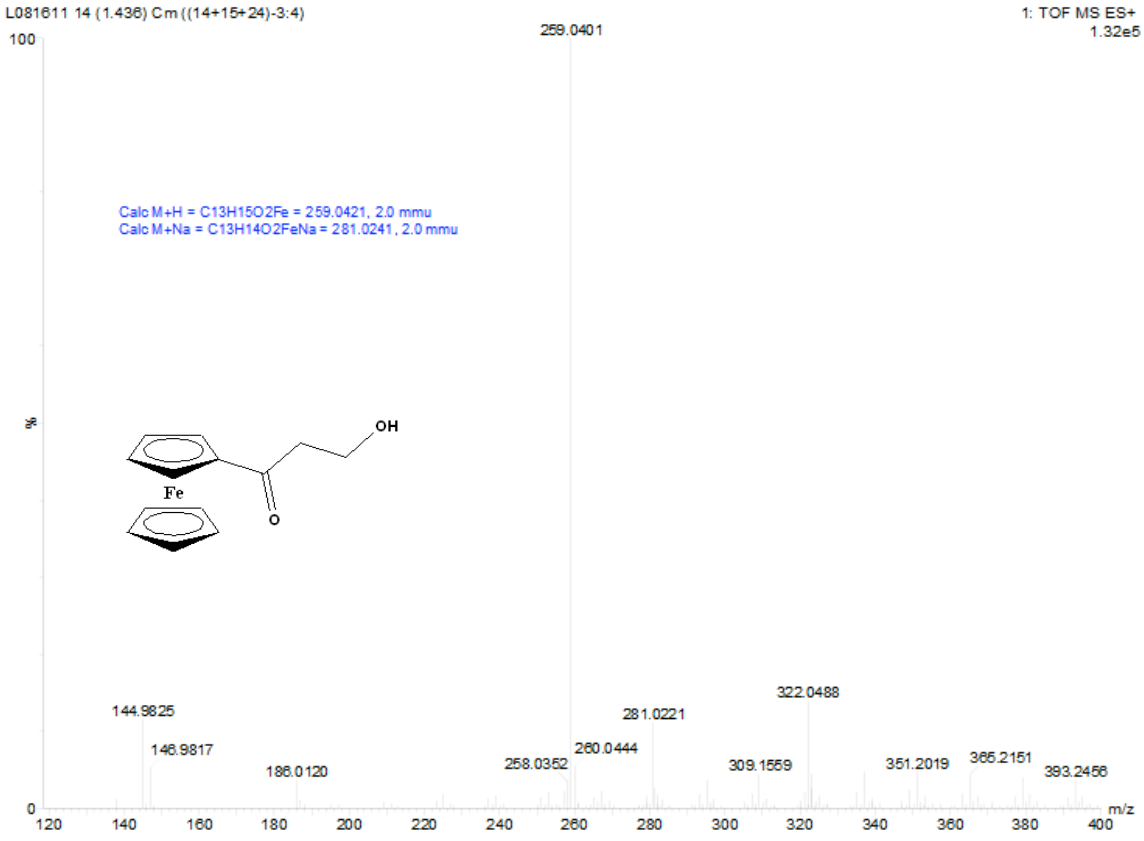

Figure A. 36 Mass Spectrum of *3-Hydroxy-1-Oxopropylferrocene*

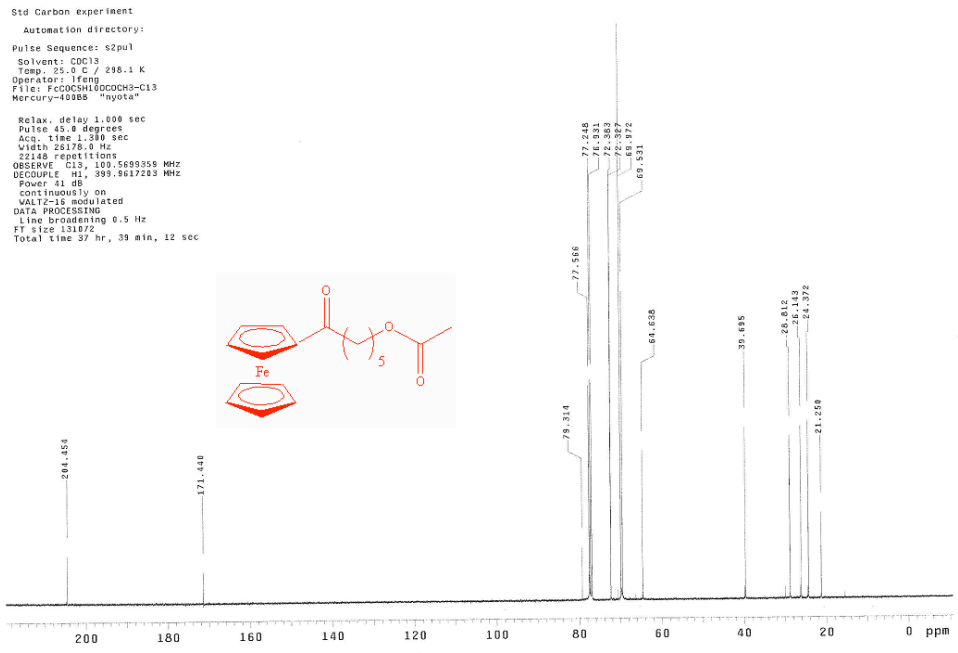

Figure A.37 ^{1}H-NMR Spectrum of *6-Acetyl-1-Oxohexylferrocene*

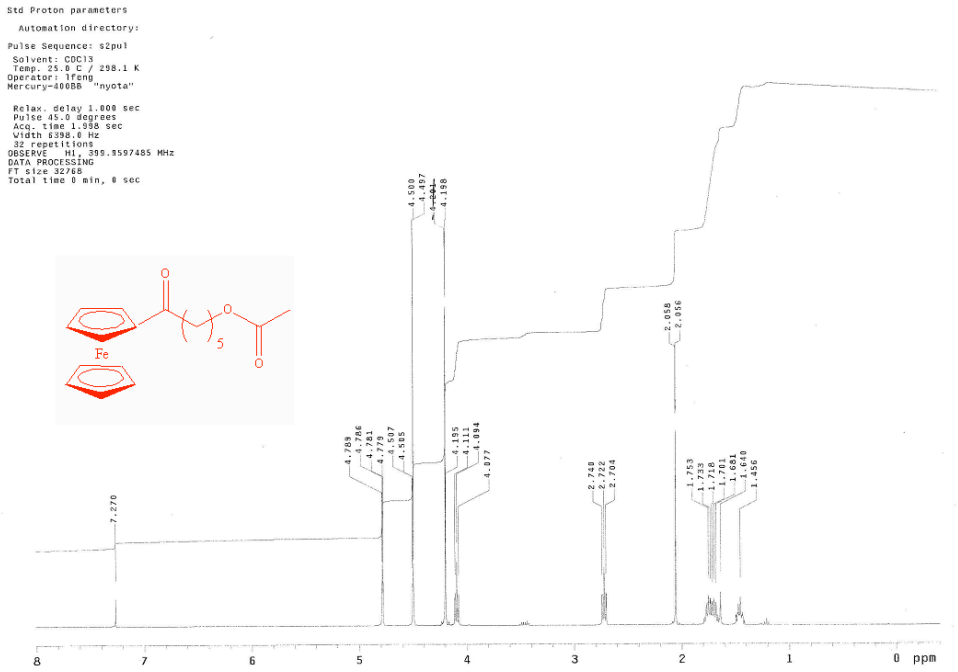

Figure A.38 ^{13}C-NMR Spectrum of *6-Acetyl-1-Oxohexylferrocene*

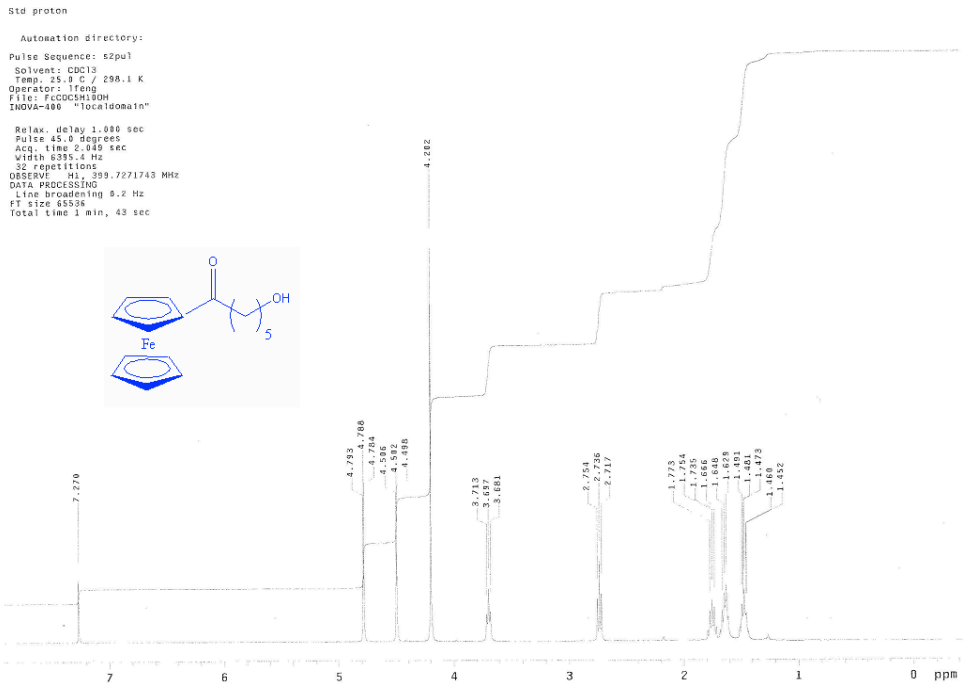

Figure A.39 ^{1}H-NMR Spectrum of *6-Hydroxy-1-Oxohexylferrocene*

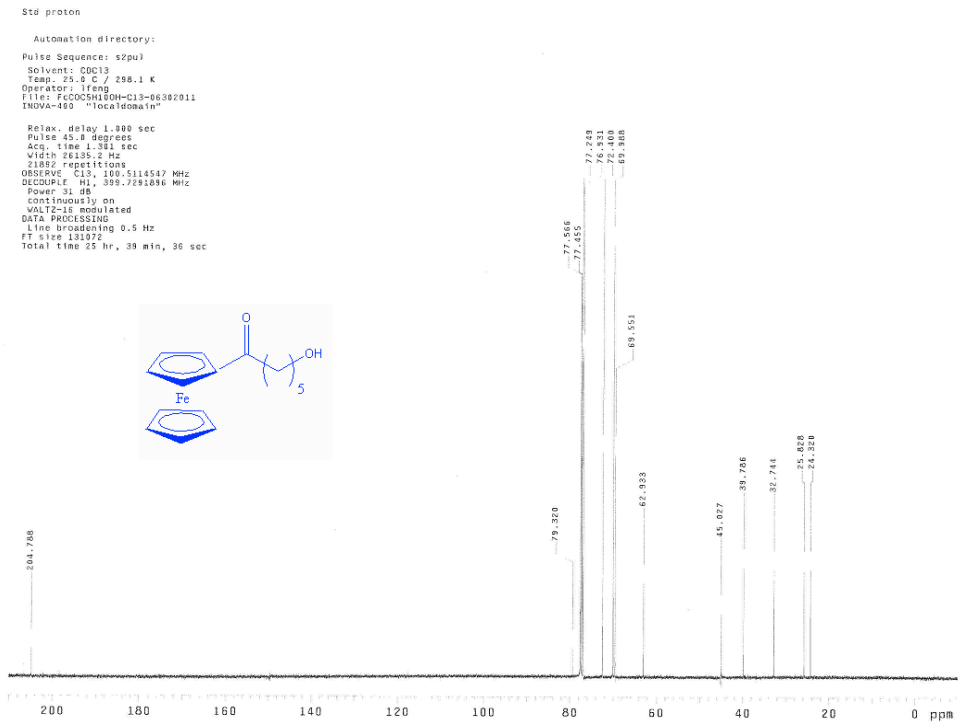

Figure A.40 ^{13}C-NMR Spectrum of *6-Hydroxy-1-Oxohexylferrocene*

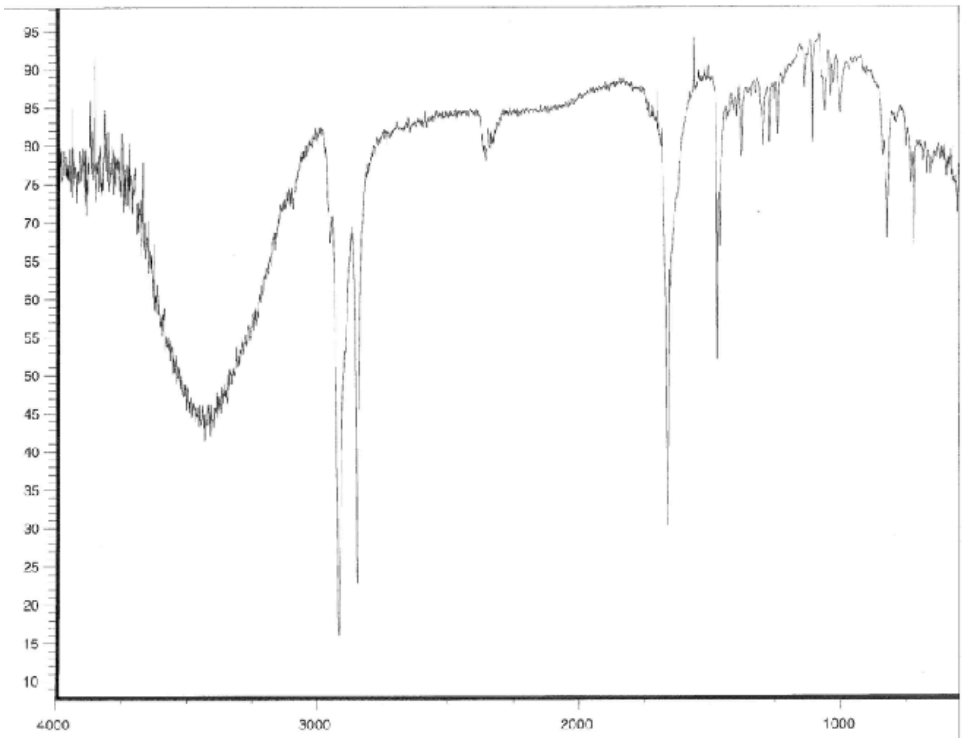

Figure A.41 FTIR Spectrum of *6-Hydroxy-1-Oxohexylferrocene*

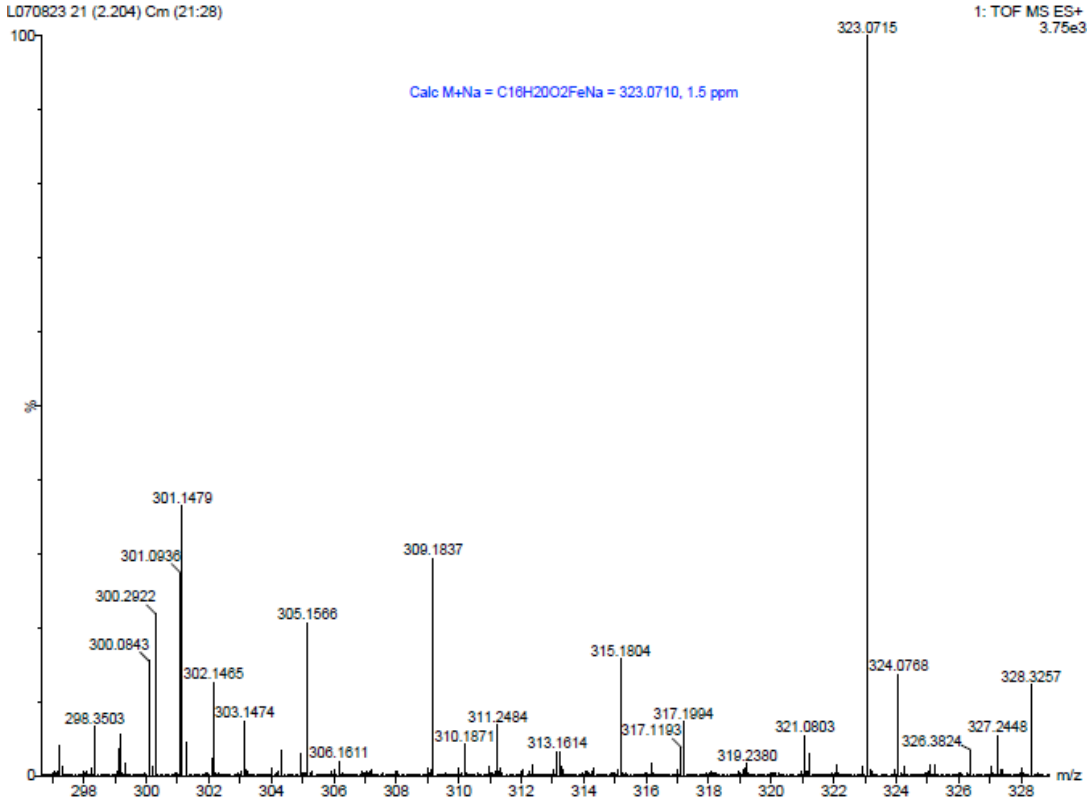

Figure A.42 Mass Spectrum of *6-Hydroxy-1-Oxohexylferrocene*

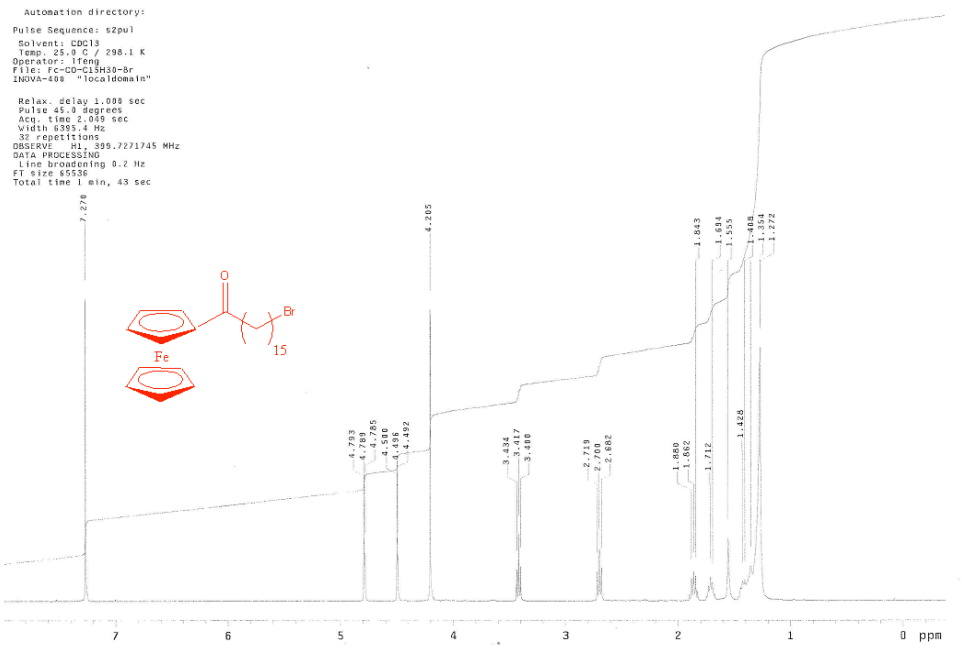

Figure A.43 ^{1}H-NMR Spectrum of *16-Bromo-1-Oxohexadecylferrocene*

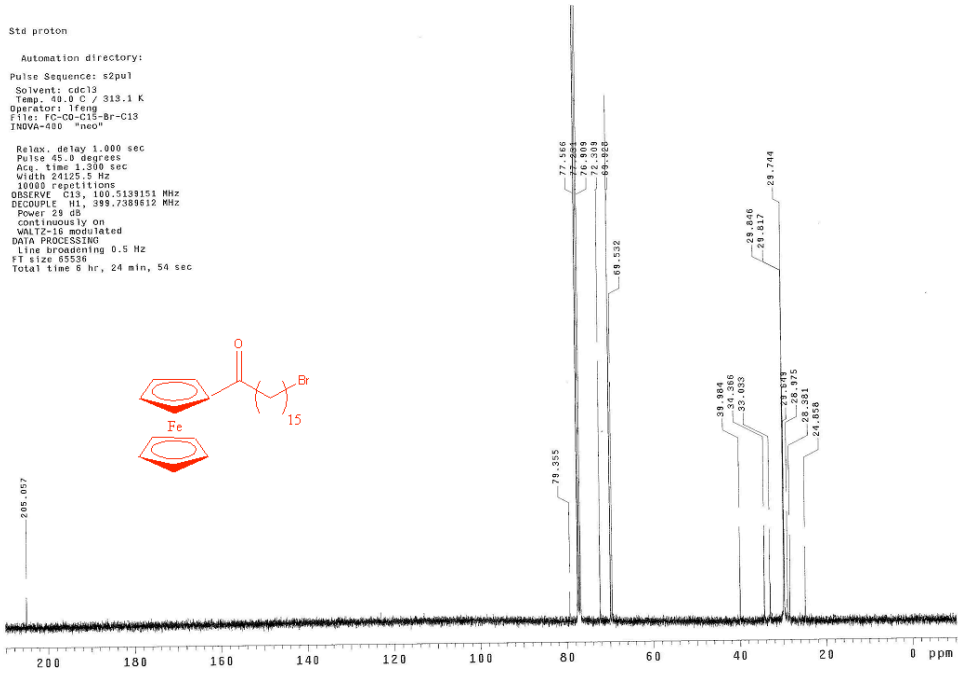

Figure A.44 ^{13}C-NMR Spectrum of *16-Bromo-1-Oxohexadecylferrocene*

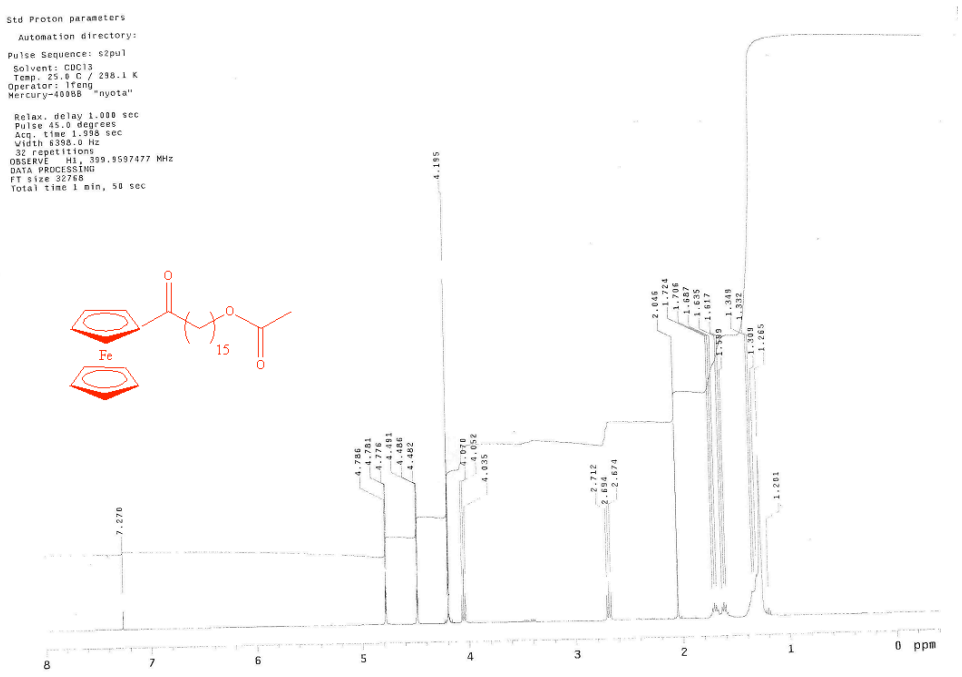

Figure A.45 ^{1}H-NMR Spectrum of *16-Acetyl-1-Oxohexadecylferrocene*

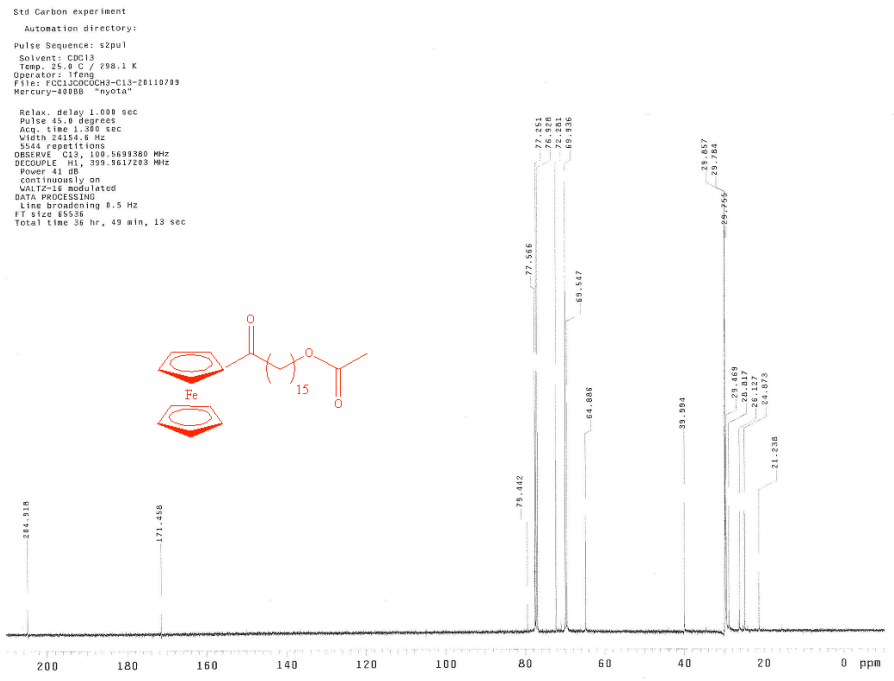

Figure A.46 ^{13}C-NMR Spectrum of *16-Acetyl-1-Oxohexadecylferrocene*

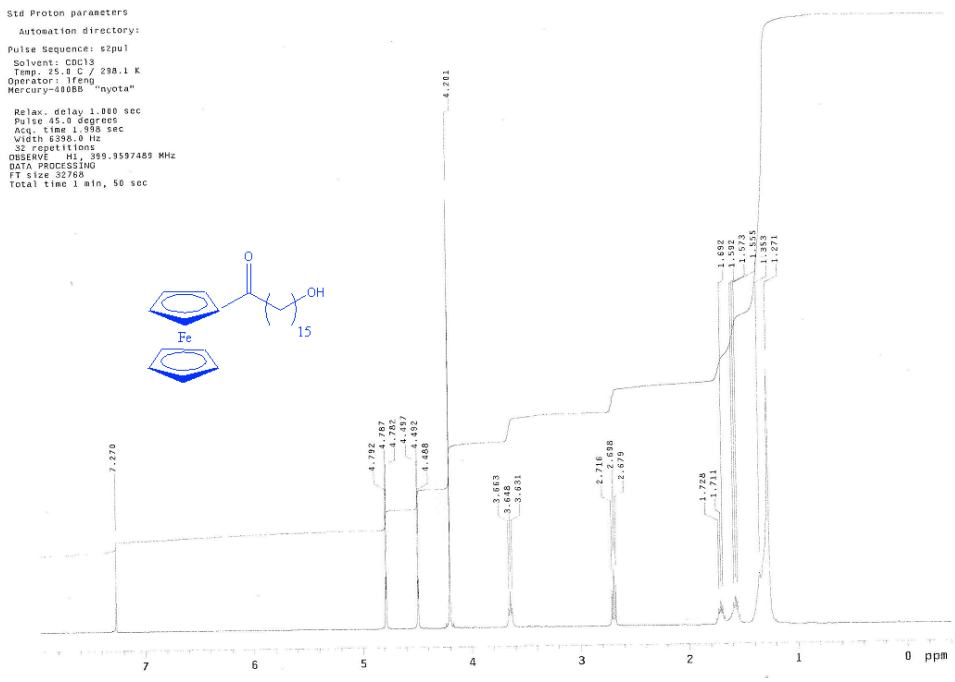

Figure A.47 ^{1}H-NMR Spectrum of *16-Hydroxy-1-Oxohexadecylferrocene*

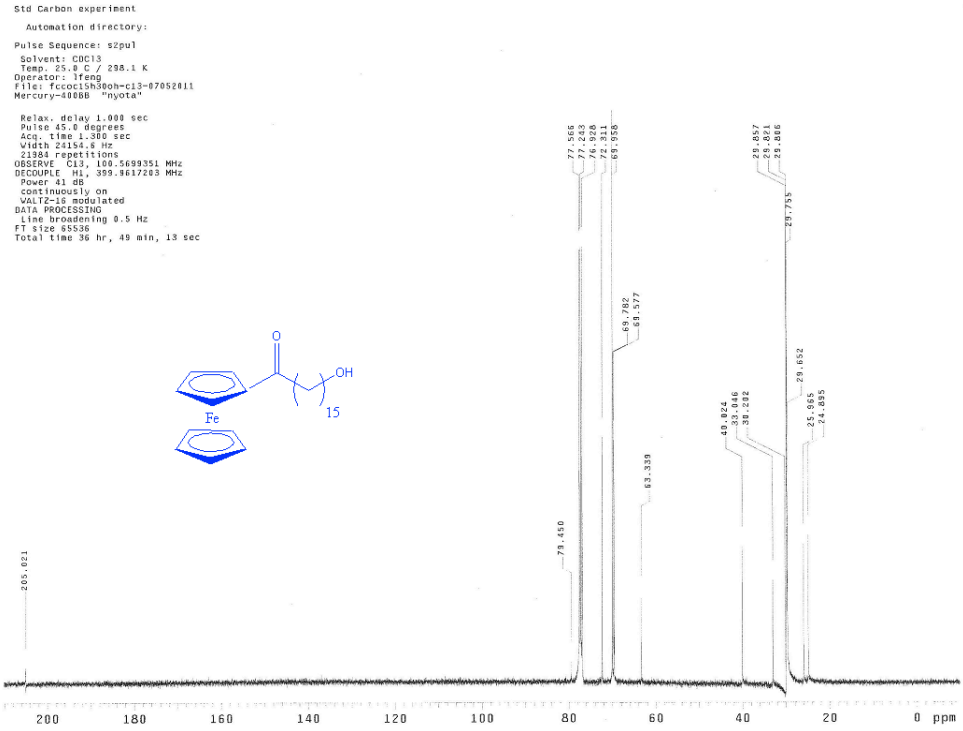

Figure A.48 ^{13}C-NMR Spectrum of *16-Hydroxy-1-Oxohexadecylferrocene*

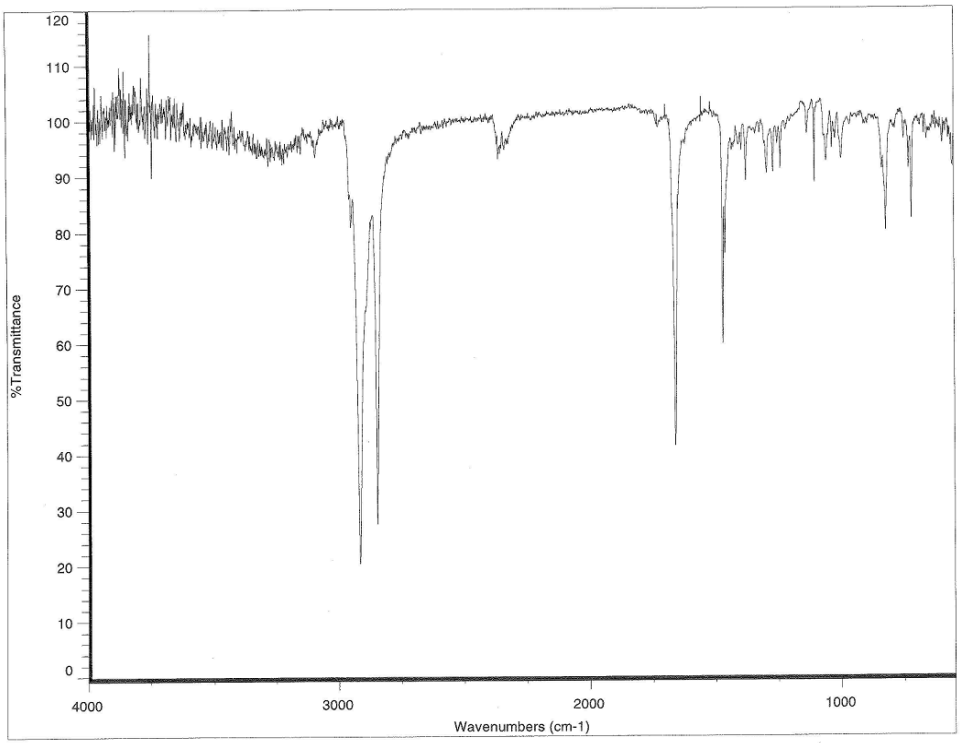

Figure A.49 FTIR Spectrum of 16-Hydroxy-1-Oxohexadecylferrocene

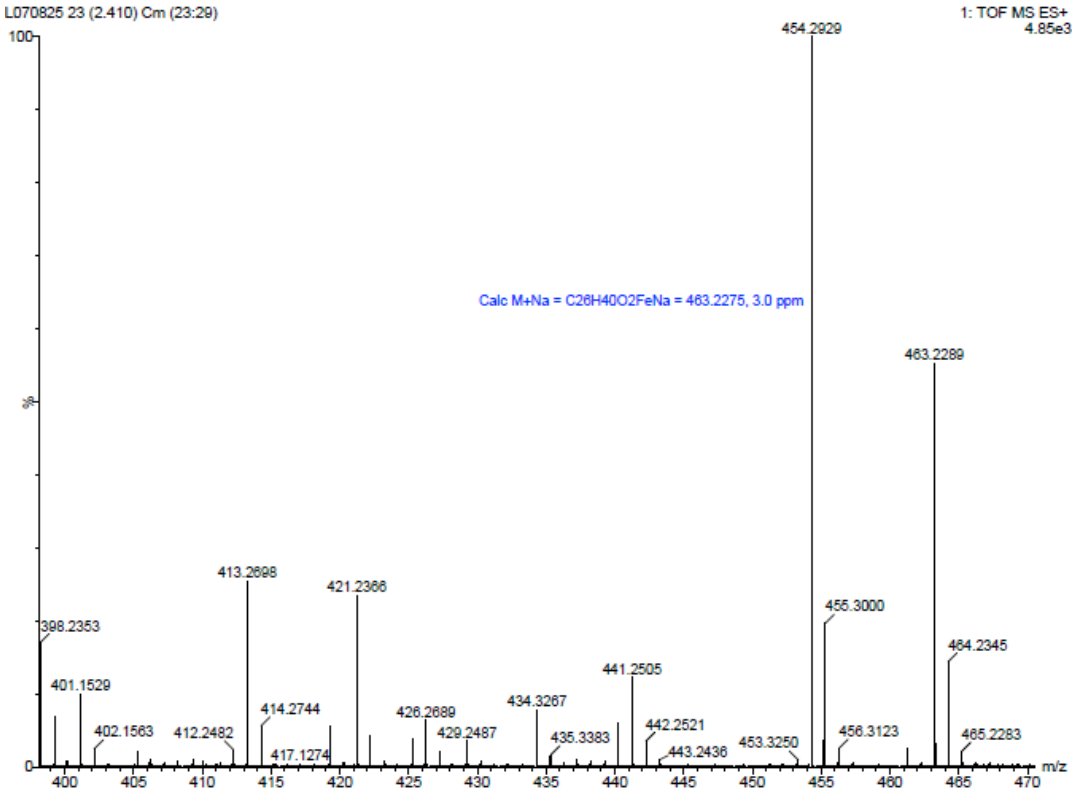

Figure A.50 Mass Spectrum of 16-Hydroxy-1-Oxohexadecylferrocene